

**DEVELOPMENT OF AS-MANUFACTURED CAD MODEL
FOR THE CONCEPT OF
“PRODUCT DNA”**

by

Yongqing Li

A dissertation submitted in partial fulfillment
of the requirements for the degree of
Doctor of Philosophy
(Mechanical Engineering)
in The University of Michigan
2009

Doctoral Committee Members:

Professor Jun Ni, Chair
Professor Shixin Jack Hu
Assistant Professor Elizaveta Levina
Dean M. Robinson, GE Global Research

DEDICATION

To my wife Haoying Zhu and daughter Emma Y. Li

ACKNOWLEDGEMENTS

I would like to express my sincere gratitude to my advisor Professor Jun Ni for his guidance, advice, and support of my research. Without him, I would not even have a chance to study in the Ph.D. program and start this research topic at the University of Michigan.

I am grateful to my dissertation committee members, Professor Jack Hu, Professor Elizaveta Levina, and Doctor Dean M. Robinson for devoting their precious time to giving me advice and reviewing this report.

TABLE OF CONTENTS

DEDICATION	ii
ACKNOWLEDGEMENTS	iii
LIST OF FIGURES	vii
LIST OF TABLES	xi
LIST OF APPENDICES	xiii
ABSTRACT	xiv
CHAPTER 1 INTRODUCTION	1
1.1 Motivation	1
1.2 Literature Review	3
1.2.1 Review of Geometry Modeling	4
1.2.2 Review of Surface Texture Characterization	5
1.2.3 Review of Physical Attributes Modeling	10
1.3 Research Objective and Tasks	14
1.3.1 Framework of “Product DNA”	14
1.3.2 Research Tasks	15
1.4 Outline	16
CHAPTER 2 GEOMETRY MODELING BASED ON NON-RIGID REGISTRATION OF 2D PROFILE CURVES	18
2.1 Introduction	18
2.2 Overview of Registration	22
2.2.1 Correspondence Establishment	23
2.2.2 Affine Combined with FFD Transformation	27
2.3 Curve and Constraints Representations	27
2.3.1 B-spline Curve	28
2.3.2 Boundary Constraints	28
2.4 The Algorithm of Non-rigid Registration	30
2.4.1 Correspondence Matrix	30
2.4.2 Transformation Mechanism	36
2.4.3 Cost Functions	37
2.4.4 Algorithm	39
2.5 Examples and Discussion	41
2.5.1 Time Complexity	41
2.5.2 Case Studies	42
2.6 Conclusions and Future Work	48

CHAPTER 3 SURFACE TEXTURE MODELING AND ANALYSIS WITH B-SPLINE WAVELET	50
3.1 Introduction	50
3.2 Overview of Wavelet Transform and MRA.....	55
3.2.1 Wavelet Transform	55
3.2.2 Multi-Resolution Analysis (MRA)	57
3.3 B-spline Wavelet based MRA of Surface Texture.....	61
3.3.1 Surface Texture Representation	61
3.3.2 Surface Texture Decomposition and Reconstruction.....	63
3.3.3 B-spline Wavelet-based MRA Algorithm.....	68
3.4 Case Studies	69
3.4.1 Correlation between Multi-scale Surface Textures and Milling Parameters	69
3.4.2 Correlation between Multi-scale Surface Textures and Tool Wear Conditions	77
3.5 Conclusions	85
CHAPTER 4 HETEROGENEOUS MODELING BASED ON CROSS-SECTIONAL MASS DENSITY POINTS	87
4.1 Introduction	87
4.2 Related Work	90
4.3 Heterogeneous Object Representations.....	93
4.3.1 Mass Density Point	93
4.3.2 Mass Density Surface.....	93
4.3.3 Mass Density Solid	94
4.4 Proposed Approach	95
4.4.1 Intensity Images and Mass Density Points.....	95
4.4.2 Geometric Surface Reconstruction	99
4.4.3 Mass Density Surface Reconstruction	100
4.4.4 3D Heterogeneous Lofting	109
4.5 Case Studies	111
4.5.1 Case Study 1.....	111
4.5.2 Case Study 2.....	113
4.5.3 Case Study 3.....	114
4.5.4 Case Study 4.....	116
4.6 Conclusions and Future Work.....	118
CHAPTER 5 CONCLUSIONS AND FUTURE WORK.....	120
5.1 Conclusions	120
5.2 Future Work	122
5.3 Original Contributions	127

APPENDICES	129
Appendix A: Transformations in 2D space.....	129
Appendix B: B-spline wavelet filter banks	131
REFERENCES	135

LIST OF FIGURES

Figure 1.1: The schematic framework of as-manufactured CAD model based "Product DNA"	14
Figure 2.1: (a) A failed sorting example of a blade sectional points, and (b) magnified view of the lead edge area	21
Figure 2.2: (a) Correspondence search with ICP method, and (b) the binary correspondence matrix	24
Figure 2.3: The end points of a curve are stretching out by minimizing the one-way directed distance.....	30
Figure 2.4: All points have the same correspondence on the curve in constrained fitting.....	31
Figure 2.5: (a) Illustration of mutual distance between the source data and the target data, (b) weighted correspondence matrix from the target data to the source data, and (c) weighted correspondence matrix from the source data to the target data.....	33
Figure 2.6: The function of weight factor with respect to the distance $d_{j,i}$ and registration error σ	35
Figure 2.7: (a) Cross sectional points of a physical turbine blade and a template curve, (b) section curves reconstructed with non-rigid registration, and (c) lofted solid model based on the reconstructed curves	42
Figure 2.8: Three different stages of 2D non-rigid registration: (a) before registration, (b) after 5 iterations, and (c) after 20 iterations	44
Figure 2.9: (a) Initial profile curve and data points, (b) reconstructed curve with non- rigid registration, and (c) reconstructed curve with constrained fitting method [64].....	45

Figure 2.10: (a) Template profile curve and measured points, (b) reconstructed curve with non-rigid registration, (c) lofted surface model, and (d) magnified view of the leading edges of the reconstructed curves.....	46
Figure 2.11: (a) Template profile curve and data points, and (b) reconstructed curve with non-rigid registration	48
Figure 3.1: Hierarchy of multiresolution curve decomposition.....	65
Figure 3.2: Hierarchy of multiresolution surface decomposition (a) standard wavelet transform, and (b) non-standard wavelet transform.....	67
Figure 3.3: Milled slots of the two-level factorial experiment design.....	70
Figure 3.4: measurement locations of three spots.....	71
Figure 3.5: spot B of slot 1 from Wyko measurement.....	71
Figure 3.6: Surface texture decomposition with B-spline wavelet filters.....	72
Figure 3.7: Surface texture decomposition with B-spline wavelet filters.....	72
Figure 3.8: Boxplots of the relationship between the surface texture and milling parameters	75
Figure 3.9: Magnified photos of the new tool, normal tool, slightly and severely worn tool	78
Figure 3.10: Milled slots with different tools	79
Figure 3.11: Spot B of the slot with new tool.....	80
Figure 3.12: Surface texture decomposition with B-spline wavelet filters.....	80
Figure 3.13: Surface texture decomposition with B-spline wavelet filters.....	81
Figure 3.14: Boxplots of the relationship between surface texture and tool wears ..	82
Figure 4.1: Schematic cone-beam CT system.....	96
Figure 4.2: (a) Intensity image of an airfoil section, and (b) intensity histogram of the image.....	97
Figure 4.3: (a) Binary image of the airfoil section, and (b) boundary image of the airfoil section	97

Figure 4.4: (a) Mass density points of the airfoil section in UG, and (b) boundary points displayed in UG..... 98

Figure 4.5: (a) Template curve and cross-sectional density points, and (b) reconstructed boundary curves with non-rigid registration method 99

Figure 4.6: Reconstructed cross-sectional Coons surfaces based on the boundary curves 100

Figure 4.7: (a) A geometry surface and simulated mass density points, and (b) height display of the mass density points and fitted mass density surface 102

Figure 4.8: Color display of multi-resolution based mass density surfaces 105

Figure 4.9: Mass density fitting error with respect to mesh resolution 105

Figure 4.10: (a) Heterogeneous points, (b) interpolated cubic heterogeneous curve, (c) interpolated linear heterogeneous curve, and (d) height display of the material composition of the fitted curves..... 106

Figure 4.11: (a) Cross-sectional mass density points of a gauge block, (b) mass density surface with 4X4 resolution, and (c) mass density surface with 35x35 resolution..... 111

Figure 4.12: Mass density fitting error with respect to the mesh resolution for the block section 112

Figure 4.13: (a) A gauge pin geometry surface, (b) mass density points, (c) mass density surface with resolution of 7X7, and (d) mass density surface with resolution of 35X35 113

Figure 4.14: Mass density fitting error with respect to the mesh resolution for the pin section 114

Figure 4.15: (a) Cross-sectional mass density points, and (b) reconstructed cross-sectional mass density surfaces..... 114

Figure 4.16: (a) Mass density solid of the compressor blade, and (b) isoparametric surfaces evaluated from the mass density solid 115

Figure 4.17: (a) Cross-sectional geometric surfaces of an artifact blade, (b) mass density points, and (c) reconstructed mass density surfaces..... 116

Figure 4.18: (a) Mass density solid of the artifact blade, and (b) isoparametric surfaces evaluated from the mass density solid 118

Figure 5.1: Product DNA based closed-loop design, manufacturing, inspection and analysis..... 126

LIST OF TABLES

Table 2.1: Error report of 2D non-rigid registration for the turbine blade	45
Table 2.2: Error report of 2D non-rigid registration for the compressor blade	47
Table 3.1: Two-level factorial design	70
Table 3.2: R_a values of all the slot surfaces from the two-level factorial experiments	73
Table 3.3: Full regression model of surface roughness	76
Table 3.4: Full regression model of surface roughness without depth of cut	76
Table 3.5: Full regression model of surface waviness	76
Table 3.6: Full regression model of surface waviness without depth of cut	77
Table 3.7: Full regression model of surface form	77
Table 3.8: Full regression model of surface form without depth of cut	77
Table 3.9: R_a values of all slot surfaces milled by tools with different tool wears .	81
Table 3.10: Regression model of surface roughness	83
Table 3.11: CIs of roughness difference between normal tool, slight and severely worn tool	83
Table 3.12: Regression model of surface waviness	84
Table 3.13: CIs of waviness difference between normal tool, slight and severely worn tool	84
Table 3.14: Regression model of surface form	84
Table 3.15: CIs of form difference between normal tool, slight and severely worn tool	84
Table 4.1: Error report of multi-resolution based density fitting	105
Table 4.2: Error report of multi-resolution based density fitting for the block section	112

Table 4.3: Error report of multi-resolution based density fitting for the pin section
..... 114

Table 4.4: Statistics of cross-sectional mass density points of the compressor blade
..... 115

Table 4.5: Error report of mass density fitting for the compressor blade's sections 116

Table 4.6: Statistics of the cross-sectional mass density points of the artifact blade
..... 117

Table 4.7: Error report of mass density fitting for the artifact blade's sections 118

LIST OF APPENDICES

Appendix A: Transformations in 2D space.....	129
Appendix B: B-spline wavelet filter banks.....	131

ABSTRACT

Today, manufacturing quality control is characterized by a plethora of data, continuously collected across the manufacturing processes and throughout a product's life cycle. The level of details with which products can be measured today allows for extraction of both dimensional and non-dimensional quality characteristics uniquely describing a product's fit and functionality. Traditionally, most of the quality inspection systems can only handle the dimensional information and few system addresses the issue of product performance both during assembly and in the field of use. Besides geometric dimensions, the product performance is also determined by other non-dimensional characteristics. For example, the sealing performance between mating surfaces is greatly influenced by surface texture; and the density distribution of a blade plays an important role on its aerodynamic performance. Hence, in order to seamlessly integrate all the dimensional and non-dimensional information for better quality inspection, process diagnosis and performance analysis, I propose a representation for the concept of "Product DNA"[1].

I have developed a representation of "Product DNA", called as-manufactured CAD model, to encode high-definition features including geometry dimensions, surface texture, and physical attributes such as mass density of the product. By decoding the high-definition features, the information of manufacturing processes and functional

performance can be examined and correlated. Under the framework of as-manufactured CAD model based “Product DNA” concept, this research mainly focuses on the coding process of geometry dimensions, surface texture and physical attributes (mass density).

For the dimensional geometry genome, a non-rigid registration approach is proposed to encode the geometry information into the as-manufactured CAD model based on inspection points. In this approach, a weighted mutual distance method is utilized to establish the correspondence and then the template object is iteratively transformed and morphed to best fit the measured points with affine and free-form deformation (FFD) transformation while maintaining geometry constraints. For the surface texture genome, a B-spline wavelet-based multi-resolution analysis (MRA) approach has been proposed for surface texture characterization. Compared to traditional surface texture analysis methods, the B-spline wavelet-based MRA method allows finer frequency regimes decomposition and thus achieves more precise diagnosis of process faults. For the physical attribute genome, a systematic approach to reconstruct a heterogeneous model based on mass density points is proposed. The decoupled B-spline based representations to model geometry and mass density allows more modeling flexibility and save huge storage space. Moreover, constraints and multi-resolution based mass density fitting algorithm guarantees to achieve reasonable mass density range and satisfied accuracy.

CHAPTER 1

INTRODUCTION

1.1 Motivation

Today's manufactured part is associated with an abundance of data continuously collected across the manufacturing processes and throughout the product life cycle. This sheer volume of data becomes overwhelming. How to efficiently extract useful information from the sheer volume of data is a challenging problem in quality inspection, process diagnosis and performance analysis. Traditionally, most of the quality evaluation systems can only handle the dimensional information. However, the process and performance are also highly related to other non-dimensional characteristics. For example, the surface texture on a work piece is actually a fingerprint of the manufacturing process; the physical attribute of residual stress is a dominant factor to fatigue life; and the density distribution of casting blade plays an important role in determining its natural frequency.

Similar to biological DNA that contains complete information for the development and functioning of a living organism, a product also possesses unique characteristics which reflect design intent, encode manufacturing information and perform particular functionalities. These unique characteristics can be viewed as "Product DNA" of the part. Modern measurement technology allows full measurement of a manufactured product in different level of details. For example, the geometric shape can

be digitized by CMM (coordinate measure machine) or laser scanner; the surface texture can be measured by laser holographic interferometers [2][1], and the internal structure can be measured by ICT (Industrial Computer Tomography). All these different types of data can be integrated together and uniquely represented by a "Product DNA", inspired from the human genomes in which a DNA molecule uniquely describes the traits of a living organism. Therefore, "Product DNA" contains a unique and complete description of a product including geometry dimensions, surface textures and physical attributes.

From the perspective of dimensional and surface quality characteristics, Zhang [1] proposed a research framework of "Product DNA" in powertrain manufacturing. By using the dimensional genome in the "Product DNA", a procedure to deal with the diagnosability problem with the "Stream of Variation" model has been designed. This procedure is used to investigate root causes of process faults by examining information contained in a large set of fault parameters with a smaller array of variables named "station-level errors". In addition, a method to characterize the product surface patterns with histogram estimators has been developed for the use of surface classification. Furthermore, a set of dimension reduction methods are introduced in case the dimensionality problem is encountered in surface classification.

Like DNA which can be decoded and used for health diagnosis and disease treatment, "Product DNA" potentially has a wide range of engineering applications. First, "Product DNA" can be used for quality inspection by comparing the decoded genome with that of nominal design. By constantly monitoring the "Product DNA" during the product life cycle, people can determine when the part has significant quality change and needs to be repaired or replaced. Second, correlating the genomes of "Product DNA" to

manufacturing parameters and conditions enables us to better understand manufacturing and diagnose process faults. Third, "Product DNA" is of great importance for design optimization. The physical attributes can be modified to achieve desired functional performance based on relationships between the physical attributes and functional performance. Last but not least, "Product DNA" can serve as a linkage to better understand the relationships between manufacturing process and physical performance.

Under the general framework of the concept "Product DNA", this research aims to develop a specific representation for "Product DNA", called as-manufactured CAD model, to implicitly represent a physical product. Like DNA which is an encoding and decoding mechanism that contains code, or language, in representing the organism, the as-manufactured CAD model encodes high-definition features including geometry topology, surface texture, and physical attributes such as mass density of the product. By decoding the high-definition features, the information of a manufacturing process and the functional performance of the part can be examined and correlated.

1.2 Literature Review

To ensure successful development of an as-manufactured CAD model to support the concept of "Product DNA", comprehensive and state-of-the-art literatures have been reviewed from the perspectives of geometry modeling, surface texture characterization and physical attributes modeling, respectively.

1.2.1 Review of Geometry Modeling

One straightforward way to encode geometry dimensions into "Product DNA" is to reconstruct a CAD model (as-manufactured model) based on the measured data points of a manufactured part. Geometry modeling is an old topic and CAD (computer aided design) is the most popular modeling technology which has been developed since 1960's. Almost every product in today's market is designed through CAD technology. In 1990, Farin [3] reviewed the most recent advances of curves and surfaces theory in CAGD (computer aided geometry design). Later on, Piegl and Tiller [4] discussed the NURBS theory from the application perspective. CAD is playing a crucial role in modern product conceptual forward design. On the other hand, reconstructing a 3D CAD model based on the measured points of an existing manufactured part becomes a very common problem in the fields of part inspection and GD&T (geometry dimensioning and tolerancing). This recent technology is called reverse engineering. Unlike the forward modeling which transforms a concept to a model, the goal of reverse engineering is to create a model to best represent the geometry shape of a manufactured part. Varady et al. [5] gave a very complete overview in terms of the four major steps of reverse engineering in which the segmentation and surface fitting is the most challenging task if no nominal model existed for the manufactured part. In the case when a design specification is available, the designer's intent could be converted into geometry or engineering constraints incorporated in the as-manufactured model. Werghi et al. [6] proposed a framework for 3D object reconstruction by incorporating geometry constraints between analytical surfaces. In parallel, Benko et al. [7] also addressed the constrained fitting problem in reverse engineering for 2D and 3D analytical curves and surfaces with a modified

Newton iteration method. Li et al. [8][9] extended the constrained fitting work to free-form objects and considered engineering constraints specifically for aero parts reconstruction. In the cases of the existence of a nominal CAD model, morphing and transforming the nominal model provides a more direct and convenient way to best fit the measured points while maintaining the original geometry topology and boundary continuities. This process is also called non-rigid registration between CAD model and point set. Different from the rigid registration which only deals with translation and rotation on the object, non-rigid registration deform the object with higher DOFs (degrees of freedom). There were many research efforts of rigid registration [10][11] conducted in the fields of object recognition and geometry inspection. On the other hand, non-rigid registration between images is recently becoming a rapidly evolving discipline in biomedical area [12] for the purpose of deformation tracking of intra-subjects, variability comparison of inter-subjects, clinical diagnosis and anatomy planning. However, to my best knowledge, the topic of non-rigid registration between CAD model and discrete point sets is rarely addressed because of complex topological relationships and geometry constraints imposed between individual geometry elements. This topic will be discussed in details in Chapter 2.

1.2.2 Review of Surface Texture Characterization

If the geometry is considered as the macro-dimensional measure of "Product DNA", the surface texture can be viewed as the micro measure of "Product DNA". While the accuracy of dimensional geometry is critical for parts tolerancing and assembly, the surface tomography greatly affects the mechanical and physical properties of contact

surfaces such as wear, friction, lubrication, sealing, bearing ratio, contact deformation, contact stress, thermal and electrical conductivity.

Although engineering surfaces of different materials manufactured by different processes normally have different tomography, the surface pattern and texture can be basically characterized by some standard terms such as lay, form, waviness and roughness [13]. Lay is the term designating the directions of predominant surface pattern mainly observed in machining surfaces. Form, waviness and roughness are utilized to describe the surface tomography in different perspective scales. Roughness refers to the finely spaced surface irregularities with short wavelengths or in other words high frequency. For the machining process, surface roughness is influenced by feed rate, cutting speed, depth of cut, as well as tooling conditions and higher frequency vibrations of the system. Waviness, on the other hand, is the surface variations with medium wavelength spacing. It may be the result of tool geometry errors, tool vibrations or the deflections of the workpiece during the manufacturing [14]. Form, referred as long wavelength, is the macroscopic geometry shape containing significant features such as radius, chamfer and curved profile.

In order to measure the details of the surface texture, a variety of high resolution instruments have been developed during the last several decades. According to different measurement principles, these devices can be roughly divided into 2 types: contact and non-contact [15]. The stylus based profilometer is the most commonly used contact instrument which can trace the surface profile by detecting and recording the vertical motions of the stylus. The resolution of this type of profilometer is determined by the tip size of the stylus that can be ranging from 0.1 μm to 1 mm. Since the stylus profilometer

is the oldest surface measurement device, a number of standards have been defined based on this type of instrument for characterizing the surface texture. However, the outputs of a profilometer are mostly two dimensional and provide no 3D information of the surface characteristics. On the other hand, the relative contacting movement between stylus and surface limits the measurement speed. In respond to these limitations, the optical methods offer an alternative faster way to measure the 3D surface texture in a comparable resolution. A recent development of confocal laser scanning microscope (CLSM) enables to gain appropriate surface information and sufficient boundary definition of wear particles in micro scale [16]. Other commercialized optical interferometry systems include Shapix produced by Coherix [1], μ Cam-3D by Novacam [17], Wyko of Veeco [18], etc. The resolution of an optical system is naturally constrained by the light wavelength. Recent advances of unconventional measurement techniques, for example the scanning electron microscope (SEM), the transmission electron microscope (TEM), the scanning tunneling microscope (STM) and the atomic force microscope (AFM), have greatly improved the scanning resolution. However, these advanced measurement techniques can only measure a very small area at one time. It costs huge time to stitch the small patches together for large surface measurement. More detailed overview of surface texture measurement methods can be found in [15][19].

After the surface tomography data is acquired, the surface characterization is then becoming important in many disciplines and industrial applications. Many research efforts have been made to develop and define 2D parameters to characterize the surface profile since the stylus profilometer was invented by 1930s [19]. For instance, the parameters introduced by Whitehouse [20] are one of the most famous parameter set. In

addition, parameters defined by different standardization organizations [13] are also commonly utilized to characterize the surface roughness. The 2D parameters most often used for inspection and tolerancing include average roughness R_a , root-mean-squares (RMS) deviation R_q , maximum valley depth R_v , maximum peak height R_p , peak to valley height R_t , ten-point height R_z and bearing ratio t_p [21]. Although the 2D parameter set is still widely in use in many applications, it is sometimes inadequate or has difficulties to characterize a surface in three dimensions. With the emergence of commercial 3D measurement system, there is an increasing need to develop a set of effective 3D parameters to characterize the 3D tomography of a surface. Dong et al. [23]-[26] carefully extended the 2D parameters and elegantly developed a set of 3D parameters to characterize the surface irregularities in the aspects of amplitude, spacing, hybrid properties between amplitude and spacing, and physical functionalities. This is the so-called Birmingham 14.

Instead of characterizing a surface with statistical methods, it is also meaningful to view the surface irregularities as a spatial signal and analyze it in the frequency domain. It has been widely accepted that an engineering surface is composed of a range of spatial frequencies and each of them results from different aspects of the manufacturing processes and performs some specific functions of the surface. Form, waviness and roughness are just roughly separated wavelength regimes. To better understand the surface characteristics in more detailed level, fine wavelength regimes separation is required. Since today's measurement systems have considerably higher resolutions, modern digital filtering techniques [27][28] make it possible to separate the surface signal into fine frequency bandwidths. Raja et al. [29] gave a very comprehensive review of

recent advances in the separation of surface texture. One common disadvantage of most current filter banks is the lumping that of a wide bandwidth into a single entry such as form, waviness and roughness. This lumping limits its applications in close monitoring of manufacturing process, tighter control of surface quality and precise prediction of part performance. For this reason, the recent development of wavelets theory and multi-resolution analysis provides a powerful tool to decompose a surface into multi-scale representations.

Wavelet is a finite energy function with compact support in both space and frequency domain and whose integral is zero [30]. Unlike Fourier analysis with basis functions of sine or cosine which have infinite space domain thus only have frequency resolution but no space resolution, the local support property of wavelet function enables wavelet transform to achieve desired resolutions in both space and frequency domains. By scaling and shifting the original waveform function (mother wavelet), the wavelet analysis provides a flexible space-frequency window where large scale wavelets are used for low frequency analysis and small scale wavelets are used for high frequency. This multi-scales wavelet transform is also called multi-resolution analysis. The wavelet transform includes many different wavelet basis functions and each of them has a different property and application. Fu et al. [31] compared 4 types of commonly used wavelets (Haar, Daubechies, Coiflets and Biorthogonal) and concluded that Bior6.8 and Coif4 are good choices for surface analysis in terms of the frequency transmission characteristics.

Due to the superior performance and capabilities compared to other filter banks, wavelets transform has been applied to 3D surface texture characterization by many

scholars [32]-[36]. However, most of the surface tomography studies based on the digitized data only focus on analyzing the discrete points for some specific application purposes while neglecting the physical surface is a continuous surface. In order to develop the as-manufactured CAD model for the concept of "Product DNA", a continuous and multi-resolution based representation will be of great significance for surface texture modeling and characterization. Because of the high order continuity and local support property, the piecewise-polynomial B-splines are naturally utilized for multi-level representation of continuous curve or surface. Chui et al. [37] developed a large family of spline wavelets. Finkelstein [38] adopted the endpoint-interpolating B-spline wavelet transform for multi-resolution analysis of B-spline curve. B-spline basis functions are widely used in the computer graphics, however, there is little research carried out on how to apply the B-spline wavelet transform to represent and analyze the surface texture in multi-resolution, and correlate different levels of continuous surface texture to the manufacturing process. Chapter 3 will address this topic in more details [100].

1.2.3 Review of Physical Attributes Modeling

Most current manufacturing quality control practice focuses on the conformance of dimensional fit of manufactured products. Few has focused on the issue of product performance both during assembly and in the field of use. Physical attribute is another important component of "Product DNA", which is critical to the functional performance of a product. For example, the residual stress of manufactured part has significant impact on its fatigue life [39]. In the aerospace industry, the density distribution of the blades produced by casting, forging and laser consolidation plays an important role to the

aerodynamic properties such as natural frequency. However, the density distribution of manufactured parts always deviates from the nominal design. In order to analyze and predict the engineering performance of the manufactured part, there is a need to build an as-manufactured CAD model that incorporates physical attributes into traditional geometry CAD model for engineering analysis.

Heterogeneous object modeling is a popular method to integrate the physical attributes into the traditional CAD model. Comprehensive research and studies [40] have been conducted for heterogeneous object modeling in a forward design way. According to the representations of the heterogeneous object, there are two basic approaches for heterogeneous modeling: discrete method and continuous method.

The discrete modeling approach represents heterogeneous object with extensive sub-divided volumes. Voxel-based model is a typical discrete model to represent the volumetric data measured by MRI and CAT scanning devices [41]-[43]. Like a pixel denotes a picture element in 2D space, a voxel represents a volume element in 3D space associated with specified physical attributes (e.g., mass density). The voxel-based model is powerful to model complex object because of its discrete representation. It is also very convenient for volumetric rendering and 3D visualization. However, because voxel-based model is an approximated description of the object, the accuracy is heavily dependent on the size of elements, i.e., the resolution of the voxels. Huge storage space is needed for a highly accurate voxel-based model. In addition, the step-wise geometry exterior and discontinuous physical attributes might bring errors for engineering analysis.

Another popular discrete representation is mesh-based model, which employs a collection of polyhedrons to represent the object [44]. Each polyhedron is defined by a set of nodes containing spatial coordinates and physical attributes. A polyhedron is also termed as an element, so the mesh-based model is also called finite element (FE) model. Mesh-based model can be directly used for engineering analysis. Like voxel-based model, it can also model very complex object. However, since it is a discrete representation, it also costs huge memory to store a highly accurate model. In addition, the mesh-based model is actually a dummy model. The editing or manipulation on the model is very cumbersome because the operation involves movement for each node.

Different from discrete modeling, continuous modeling employs an exact and rigorous representation to model the object. Therefore, it is more elegant and accurate. Comprehensive studies have been conducted in this category. Kumar et al. [45] proposed an approach of r_m -set to represent heterogeneous objects by integrating the material composition along with the geometry in the solid model. Based on this representation, a series of heterogeneous modeling operations (e.g., union, intersection, difference) were also defined analogous to the geometry operation. Biswas et al. [46] proposed an implicitly constrained material function to model the material composition based on distance fields with reference to material features. This approach guarantees smoothness and analytic properties of the model and is applicable to represent material features of arbitrary dimension, shape and topology. Explicit analytical functions are adopted by Zhu [47] to represent material distribution of the heterogeneous object. This representation is intuitive and easy to use. However, the explicit material function is highly tight to the coordinate system, which makes it only suitable to model simple forms of heterogeneous

objects. Siu and Tan [48] proposed a grading source-based scheme for heterogeneous object modeling. In this scheme, the object acts as a container whose material composition is evaluated based on distances from the source features. Later on, Kou and Tan [49] introduced a hierarchical representation to model heterogeneous object in which the geometry is represented by B-rep and the material distribution is modeled and evaluated through a heterogeneous feature tree. A heterogeneous object is considered as a multidimensional point set with multiple attributes in [50]. For this hypervolume model, the function representation (F-Rep) is used as the basic model for the point set geometry, and the attributes are modeled independently with real-valued scalar functions. Spline-based representations are employed to model the heterogeneous object by several researchers [51]-[56]. For example, for a B-spline volume represented heterogeneous object, the physical attributes are encoded into the control points by extending the dimensions from three dimensions to higher-order dimensions. Many of the spline-based heterogeneous modeling methods couple the geometry and attribute together to share the same knot vector, degree and control points. This unified representation usually limits the flexibility of the physical attributes design. Martin and Cohen [57] presented a method to model volumetric data with decoupled trivariate NURBS representation in which the geometry and attributes could have different knot vector, order and number of control points except sharing the same parametric domain. This decoupled representation means the geometry and physical attributes can be modeled with different resolutions and thus increases design flexibility.

Although there are many methods proposed for heterogeneous object modeling, most of the studies are performed in a forward design way that converts design intent into

a product model. Different from the traditional heterogeneous object modeling in a forward design approach, this dissertation will address the problem of reconstructing a heterogeneous object based on cross-sectional mass density points measured from a manufactured part. Chapter 4 will discuss this topic in more details.

1.3 Research Objective and Tasks

1.3.1 Framework of "Product DNA"

In this proposed research, the concept of "Product DNA" will be further expanded

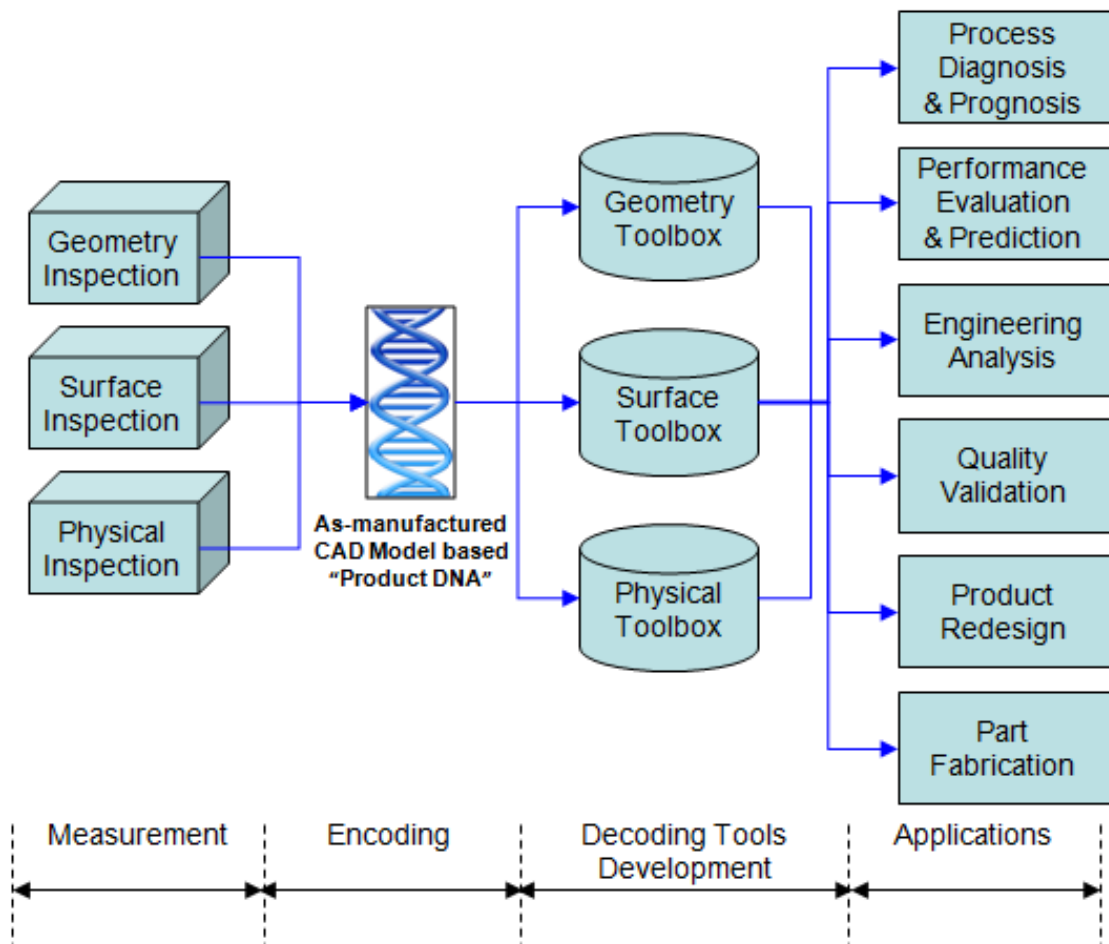


Figure 1.1: The schematic framework of as-manufactured CAD model based "Product DNA"

in a systematic way to account for all characteristics. Figure 1.1 shows the generic framework for the concept of "Product DNA". Under this framework, we develop an as-manufactured CAD model to uniquely represent the "Product DNA" of a manufactured part based on measurement data. The model encodes all the part characteristics, including geometric dimensions, surface textures and physical attributes (density, residual stress, etc.). This process is called DNA encoding. Following that, a variety of toolboxes will be developed to decode the information of "Product DNA" for purposes of different applications such as process diagnosis and prognosis, functional performance prediction, engineering analysis, quality inspection and validation, product redesign and fabrication. The proposed framework of "Product DNA" will be demonstrated from the perspectives of geometry dimension, surface texture and physical attributes, respectively. The objective of the proposed concept of "Product DNA" is to help better understand the relationships between manufacturing process, part quality and physical performance and thus to reduce life-cycle cost of the product development.

1.3.2 Research Tasks

In Zhang's [1] Ph.D. dissertation, three topics are addressed independently under the framework of "Product DNA" in powerchain manufacturing: (1) measurement scheme improvement of dimensional quality characteristics; (2) robust engineering modeling for process fault diagnosis; and (3) surface classification. In order to develop the as-manufactured CAD model for the concept of "Product DNA", this proposed research will focus on the coding process under the framework of "Product DNA" with real case studies in the aerospace and automobile industry. Specifically, the tasks of

product information coding are carried out in three different aspects: (1) dimensional geometry; (2) surface texture; and (3) physical attribute (mass density).

(1) For the dimensional geometry coding, a fast and automated geometry modeling tool with non-rigid registration method is developed. In the case of given nominal geometry model, the as-manufactured model can be reconstructed quickly by morphing the nominal model to best fit the measured data points from actual parts while incorporating geometric constraints.

(2) For the surface texture coding, a B-spline wavelet based representation is proposed for multi-resolution analysis. The surface texture details are encoded in the multi-level B-spline surfaces using B-spline wavelets functions. By decoding the wavelets in different scales, the surface characteristics can be analyzed and correlated to manufacturing process

(3) For the physical attribute coding, a systematic approach is proposed for heterogeneous modeling based on cross-sectional mass density points. Mass density distribution has significant impact on the product performance. A decoupled B-spline representation is proposed to model the geometry and mass density independently with different resolutions.

1.4 Outline

This dissertation presents the as-manufactured CAD model for the concept of "Product DNA" and its development and implementation.

Chapter 1 of the dissertation provides a brief description of this doctoral research and literature review of related research work.

Chapter 2 describes a novel algorithm for fast and accurate geometry modeling based on the technology of non-rigid registration between nominal CAD model and inspection points. Some real examples have demonstrated its superiority compared to the state-of-the-art algorithms and tools.

A multi-resolution based B-spline surface is proposed for surface texture modeling and analysis in Chapter 3. The idea of multi-resolution engineering surface analysis is introduced. Cases studies of end-milling surfaces have demonstrated the success and effectiveness of the proposed method.

By taking mass density as an example of physical attribute, Chapter 4 presents a method to incorporate mass density information into traditional geometry CAD model based on cross-sectional mass density points. Decoupled representation is adopted to model geometry and mass density independently. Moreover, a constraint based multi-resolution method is proposed for mass density fitting in order to achieve reasonable mass density range and satisfied accuracy.

Chapter 5 concludes this research and describes the future work and original contributions.

CHAPTER 2

GEOMETRY MODELING BASED ON NON-RIGID REGISTRATION OF 2D PROFILE CURVES

2.1 Introduction

One straightforward way to encode the geometry dimensions into the "Product DNA" is to reconstruct a CAD model (as-manufactured model) based on the measured points of a manufactured part. Reverse engineering provides an effective solution to build such a CAD model based on the measurement data. When the nominal CAD models and original drawings are not available, it is often necessary to reconstruct a CAD model (also called as-manufactured model) based on the measured points for downstream applications such as engineering analysis, part re-design and fabrication. Another important application of the as-manufactured model is for quality validation when the nominal CAD is available. Influenced by various manufacturing factors, the manufactured part usually differs from the designed nominal model to some extent. The difference of some key parameters between the as-manufactured model and the nominal model can quantitatively evaluate the manufacturing quality.

As stated in the review of reverse engineering [5], surface fitting is a crucial step to transform the measured points into a geometry CAD model. There are many algorithms proposed for single surface fitting in the research field. Pratt [58] proposed a general

framework to fit an algebraic curve or surface of a given shape to a two or three-dimensional point set with a direct least-squares fitting method. Based on the consideration of convenience and efficiency, the algebraic distance is minimized, subject to some quadratic normalization constraints imposed on the variables of the implicit expression of algebraic curve or surface. Pottmann et al. [59] applied methods of line geometry to the set of surface normals in combination with techniques of numerical approximation to fit a rotational surface or helical surface to a given 3D scattered points. Marshall et al. [60] presented methods for least-squares fitting of analytical surfaces (sphere, cylinder, cone and tori) for the purpose of data segmentation. In their fitting algorithm, a faithful distance function is used to approximate the true geometric distance, which achieves robustness in the presence of geometric degeneracy. In the NURBS book [4], there are detailed illustrations of how to interpolate or fit a B-spline surface to a grid of regular points. For irregularly distributed points, Ma and Kruth [61] presented a parameterization method by iteratively projecting the scattered points to a base surface until reaching a final fitted B-spline surface. In order to achieve high fitting accuracy, Weiss et al. [62] analyzed the free quantities of least-squares fitting such as the number of knots, the weights of smoothing function and the best parameterization of data points and thus provided practical solutions to compute good initial parameterizations and simultaneously maintain tight fitting tolerances and smoothness.

In practice, a nominally designed CAD model is usually bounded by a number of surfaces neighboring one another. Moreover, various geometric constraints are imposed on some individual surfaces or between different surfaces to satisfy particular requirements of engineering rules [8]. In order to capture such design intents during the

reverse engineering, the geometric constraints must be incorporated into the multiple surfaces fitting process. Werghi et al. [6] proposed a general incremental framework of model reconstruction in which the geometric constraints can be integrated into the fitting process, leading to an optimal tradeoff between the shape fitting error and the constraint tolerance. In the numerical algorithm, the constrained fitting problem was converted into a sequential of unconstrained optimization problem with penalized constraints terms, which was solved by standard Levenberg–Marquardt method. Benko et al. [63] described a detailed procedure for 3D object reconstruction based on the segmented point cloud. Starting from simple surface fitting and 2D constrained profile based translational and rotational surface fitting, a B-rep model is eventually reconstructed with post blend creation and further beautification. Later on, the same team [7] summarized the constrained fitting work by considering multiple curves (lines and circular arcs) in 2D and quadratic surfaces (planes, spheres, cylinders, cones and torus) in 3D with commonly encountered geometric constraints. Different from Werghi’s method, the Lagrangian-multiplier method was utilized to solve the problem of conflict constraints by converting inconsistent constraints into independent constraints. Recently, Li et al. [9] and Ke et al. [64] extended 2D constrained fitting by including B-spline curves into the 2D profile, which has demonstrated great industrial success in complex surface reconstruction such as lofting surface, extruding surface and revolving surface.

There are three basic assumptions in the 2D constrained fitting [64]: sorted profile data points, segmented sub-point sets and initial fitted curve of each sub-point set. However, in practice the sorting and segmentation often turn out to be very challenging when the data points are noisy or non-uniformly distributed. A failed sorting of data points

will result in wrong parameterization of the points during the curve reconstruction. Figure 2.1 shows a failed sorting example with closest point method due to some missing points on the leading edge (the arrow is the sorting direction). Even for the high quality data points, it is also difficult to judge which curve segment the points around the connecting areas belong to. In addition, if a series of 2D profile curves, for example, the cross sections of a lofting or sweeping surface, need to be reconstructed, the work of sorting, segmentation and initial curves fitting for each section will be very labor intensive. Moreover, the compatibility conditions that all cross-sectional B-spline curves must share the same knot vector and number of control vertices are hard to maintain. All these disadvantages of the current constrained fitting method have limited its use to noisy data

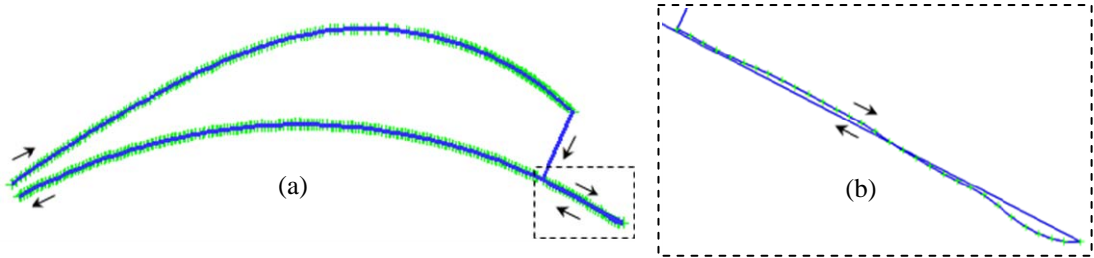


Figure 2.1: (a) A failed sorting example of a blade sectional points, and (b) magnified view of the lead edge area

points and fast reverse modeling.

In this research, we propose a new method, called constraints based non-rigid registration, for 2D profile curves based geometry modeling. We assume there exists a template profile curve, which can always be obtained by slicing the nominal CAD model or created by sketching. The objective is to recover the shape of the manufactured part based on the template nominal curve and measured points. Unlike the constrained fitting that only minimizes the one-way distance from the data points to initial fitted curves; we

consider a weighted mutual (two-way) distances between the template profile curve and the data points as the objective function. With affine combined with FFD (free-form deformation) transformation, the template curve can iteratively move closer to the target data points by minimizing the weighted mutual distances while satisfying specified geometry constraints. Compared with the constrained fitting, non-rigid registration is a fully automated process with more robustness. The advantages are six-folds: (1) no necessity for data points sorting; (2) no need for segmentation of data points; (3) no need of parameterization for data points belonging to B-spline curves; (4) immunity to noisy data points; (5) the template curve can be used for a series of cross-sectional points with similar topology, thus it is not necessary to fit the initial curves for each section; and (6) the compatibility conditions [65] between different sections are automatically satisfied. Curve compatibility is an important condition to obtain a smooth lofted surface.

The rest of this chapter is organized as follows: the next section gives an overview on the state-of-the-art registration methods. The representations of curve objects and constraints are presented in Section 2.3. Following that, the algorithm of the proposed method is illustrated in details in Section 2.4. In Section 2.5, we present some simulated and real examples and demonstrate the effectiveness and superiority of the proposed method. Finally, Section 2.6 draws the conclusion and future work.

2.2 Overview of Registration

Registration is a coordinate transformation process through which the source data is aligned to the target data so that similar features are brought into correspondence. Mathematically, the objective of registration is to find the transformation matrix by

minimizing the generalized distance, also known as dissimilarity, from the source data to the target data. Normally, the dissimilarity can be measured by computing the Euclidean distance between the corresponding feature pairs (also called correspondence) on the source and target data, respectively. Therefore, the establishment of correspondence and selection of transformation are the two essential tasks of registration. The cost function of registration can be stated as follows.

$$\text{Minimize: } \sum_{i,j} \omega_{i,j} \left(\text{dist} \left(f_i(\mathbf{X}_i), \mathbf{Y}_j \right) \right)^2 \quad (2.1)$$

Where \mathbf{X}_i and \mathbf{Y}_j are the corresponding feature pairs on the source and target data, respectively; f_i is the transformation function applied on the source data \mathbf{X}_i ; $\text{dist} \left(f(\mathbf{X}), \mathbf{Y}_j \right)$ is defined as the directed Euclidian distance from the transformed source data \mathbf{X}_i to the target data \mathbf{Y}_j ; $\omega_{i,j}$ is a weight factor of the directed distance from \mathbf{X}_i to \mathbf{Y}_j . The magnitude of $\omega_{i,j}$ indicates how much contribution of the corresponding directed distance to the cost function. Section 2.2.1 reviews some typical methods of how to determine the weight factor.

2.2.1 Correspondence Establishment

One of the most popular correspondence establishment methods is the closest distance method. A classic paradigm of this method is Iterative Closest Point (ICP) algorithm [10], which takes the nearest neighbor on the target data for a given point on source data as its correspondence. The correspondence is then updated by conducting iterative transformations. The correspondence established by this method can be viewed as

a binary matrix between the source and target data. For example, two point sets $\mathbf{X} = \{\mathbf{X}_i, i=1\dots m\}$ and $\mathbf{Y} = \{\mathbf{Y}_j, j=1\dots n\}$ as shown in Figure 2.2(a), if a source point \mathbf{X}_i corresponds a target point \mathbf{Y}_j , then $\omega_{i,j} = 1$; otherwise, $\omega_{i,j} = 0$. Therefore, the cost function of ICP method can be written as:

$$E(f) = \sum_{i,j} \omega_{i,j} \|f(\mathbf{X}_i) - \mathbf{Y}_j\|^2 \quad (2.2)$$

where f is the rigid transformation and $\|\bullet\|$ is the Euclidean norm.

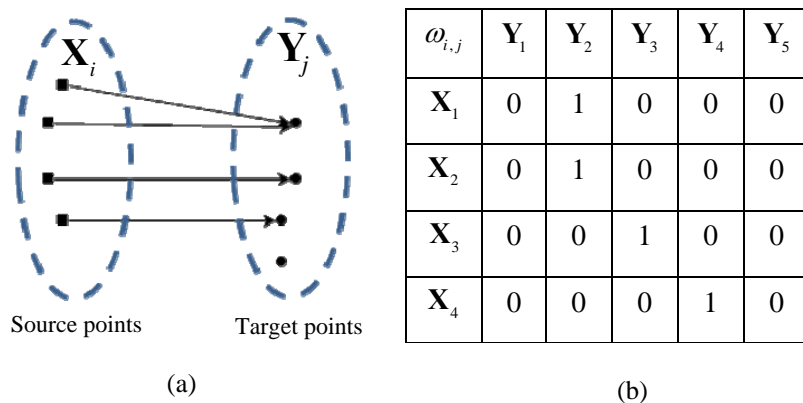


Figure 2.2: (a) Correspondence search with ICP method, and (b) the binary correspondence matrix

One limitation of ICP method is that the corresponding point pairs are very sensitive to data noise and relative positions between source and target points. It is observed in Figure 2.2 that some source points might have the same correspondence but some target points might not have correspondence.

The constrained fitting [64] can also be viewed as a registration process where initial constructed curves (source data) \mathbf{C}_i are iteratively transformed to best fit the measured

points (target data) \mathbf{Y} by minimizing the directed distance from the target points to the curves, i.e.,

$$E(f_i) = \sum_{j,i} \omega_{j,i} \left(\text{dist}(\mathbf{Y}_j, f_i(\mathbf{C}_i)) \right)^2 \quad (2.3)$$

The weight factor $\omega_{j,i}$ depends on segmentation of the target points \mathbf{Y} . If \mathbf{Y}_j belongs to \mathbf{C}_i , then $\omega_{j,i} = 1$; otherwise $\omega_{j,i} = 0$. f_i can be viewed as the transformation function represented with respect to the parameters of curve \mathbf{C}_i , and thus the curve is transformed by changing the curve parameters. $\text{dist}(\mathbf{Y}_j, f_i(\mathbf{C}_i))$ is computed as the minimum distance from point \mathbf{Y}_j to its corresponding curve \mathbf{C}_i . If we denote the closest point of \mathbf{Y}_j on curve \mathbf{C}_i as \mathbf{X}_j , then the cost function can be rewritten as:

$$E(f_i) = \sum_{j,i} \omega_{j,i} \left\| \mathbf{Y}_j - f_i(\mathbf{X}_j) \right\|^2 \quad (2.4)$$

It is recognized that equation (2.4) has the same form as equation (2.2) except that different transformation functions are applied on different types of curves. Therefore, constrained fitting also establishes a one-way binary correspondence matrix such that for each data point \mathbf{Y}_j , the nearest point \mathbf{X}_j on curve \mathbf{C}_i is considered as the correspondence.

Instead of assigning the same weight (it is 1) to the distance of each pair of correspondence, Weiss et al. [62] set different weights to express the relative “importance” of the data points to a fitted B-spline surface according to reliability criteria. Normally, the smaller the distance, the larger the weight. The correspondence matrix is

thus a relaxation of the binary matrix where the entry value $\omega_{i,j}$ can range from 0 to 1. The relaxation of the correspondence matrix allows partial matching between the source data and target data.

Chui [66] also adopted the relaxed correspondence matrix (called softassign) for point matching between two discrete point sets. The weight for the distance of each pair of corresponding points is computed as a function with respect to the distance and the annealing temperature, whose initial value is set to the largest square distance of all point pairs. As the iteration proceeds, the relaxed correspondence matrix is updated and towards to a binary matrix when the source point set is getting closer to the target point set.

Besides considering the coordinates information of the points, there are also methods that consider other geometric properties of the points for registration. Jonson and Hebert [67] presented a representation for mesh surface rigid registration by matching oriented points that is based on indexing of spin-images. Bae and Lichti [68] proposed a method based on geometric primitives and neighborhood search for partially overlapped point clouds. In this method, the change of geometric curvature and approximated normal vector of the surface formed by a point and its neighborhood are used to determine correspondence of point clouds. Because the problem considered in this research is non-rigid registration, the normal and curvature might be far different between the source data and target data. Moreover, even for rigid registration, if the discrete points are very noisy, the computed normal and curvature are not stable and cannot be used for registration. Therefore, only the coordinates of the points are used for correspondence establishment of non-rigid registration in this research.

2.2.2 Affine Combined with FFD Transformation

Affine transformation is a linear operation, which is suitable for global registration when the source data is far from the target data. Traditionally, FFD has important application in forward design. Kagan et al [69] proposed two new methods to create sculptured surfaces and volumetric solids by mechanically deforming the B-spline elements with adaptive refinement. In order to overcome the restriction of FFD on the model with holes or gaps, a discontinuous FFD (DFFD) [70] approach was proposed to incorporate iso-parameteric discontinuities into the deformation. This approach also demonstrated great application in computer-aided surgical simulation [71]. Because FFD is a non-linear operation based on B-spline basis functions with local supportive properties, it works well for local deformation when the source data is very close to the target data. The aim of combining affine and FFD transformation is to make the non-rigid registration behavior with affine transformation dominated at the beginning and then FFD more dominated as the source object is getting closer to the target object.

With the notations of 2D transformation reviewed in Appendix A, the affine combined with FFD transformation of a point \mathbf{P}_k embedded in a lattice can be expressed as:

$$f(\mathbf{P}_k) = \sum_{i',j'=0}^{M,N} B_{i',j'}(u_k, v_k) f(\mathbf{V}_{i',j'}) = \sum_{i',j'=0}^{M,N} B_{i',j'}(u_k, v_k) (\mathbf{T}\mathbf{V}_{i',j'} + \boldsymbol{\delta}_{i',j'}) = \mathbf{T}\mathbf{P}_k + \mathbf{B}_{\mathbf{P}_k}^T \boldsymbol{\delta} \quad (2.5)$$

2.3 Curve and Constraints Representations

In this research, the 2D profile only composed of multiple B-spline curves is considered because the line and circular curves can be converted into B-spline curves.

2.3.1 B-spline Curve

A B-spline curve of order r (degree + 1) can be defined as [5]:

$$\mathbf{C}(t) = \sum_{k=0}^L N_{k,r}(t) \mathbf{P}_k \triangleq \mathbf{N}^T \mathbf{P} \quad (2.6)$$

where $\mathbf{P} = [\mathbf{P}_0 \ \cdots \ \mathbf{P}_L]^T$ are the control vertices; $\mathbf{N} = [N_{0,r}(t) \ \cdots \ N_{L,r}(t)]^T$ and $N_{k,r}(t)$ is the r^{th} order B-spline basis functions with the knot vectors $\mathbf{t} = [t_0 \ \cdots \ t_r \ \cdots \ t_L \ \cdots \ t_{L+r}]$.

Substituting equation (A.5) to equation (2.6), the B-spline curve can be represented with respect to the control points of the designed lattice as:

$$\mathbf{C}(t) = \mathbf{N}^T \mathbf{B}_p \mathbf{V} \quad (2.7)$$

where $\mathbf{B}_p = [\mathbf{B}_{p_0}^T \ \cdots \ \mathbf{B}_{p_L}^T]^T$.

2.3.2 Boundary Constraints

In most applications, the positional (G^0) and tangent (G^1) continuities are the prevalent constraints enforced on the endpoints of neighboring B-spline curves. The first order derivatives on both endpoints for a B-spline curve expressed by equation (2.6) can be computed as:

$$\mathbf{C}'(0) = \frac{r-1}{t_r} (\mathbf{P}_1 - \mathbf{P}_0) \quad (2.8)$$

$$\mathbf{C}'(1) = \frac{r-1}{1-t_L} (\mathbf{P}_L - \mathbf{P}_{L-1}) \quad (2.9)$$

There are four cases of connection between two B-spline curves: start point to start point, start point to end point, end point to start point and end point to end point. Without

loss of generality, we only consider the case of start point to start point. Suppose $\{\mathbf{P}_k, k = 0 \dots L\}$ and $\{\mathbf{Q}_j, j = 0 \dots J\}$ are the control vertices of two B-spline curves $\mathbf{C}_p(t)$ and $\mathbf{C}_q(t)$, respectively, then the positional continuity means that they must have the same start point after transformation, i.e.,

$$f(\mathbf{P}_0) - f(\mathbf{Q}_0) = \mathbf{0} \quad (2.10)$$

The G^1 continuity requires that the first order derivatives $\mathbf{C}'_p(0)$ and $\mathbf{C}'_q(0)$ are collinear after transformation. Mathematically, the G^1 constraint can be formed as follows with the derivative equation (2.8).

$$[f(\mathbf{P}_1) - f(\mathbf{P}_0)] - \eta[f(\mathbf{Q}_1) - f(\mathbf{Q}_0)] = \mathbf{0} \quad (2.11)$$

where η is a constant which can be evaluated as the ratio of the length of vector $\mathbf{C}'_p(0)$ over that of vector $\mathbf{C}'_q(0)$ from the template curve.

Suppose f is the affine combined with FFD transformation, the continuity conditions can be simplified as follows by plugging equation (2.5) to equations (2.10) and (2.11), respectively.

$$\mathbf{T}(\mathbf{P}_0 - \mathbf{Q}_0) + (\mathbf{B}_{\mathbf{P}_0}^T - \mathbf{B}_{\mathbf{Q}_0}^T)\delta = \mathbf{0} \quad (2.12)$$

$$\mathbf{T}[(\mathbf{P}_1 - \mathbf{P}_0) - \eta(\mathbf{Q}_1 - \mathbf{Q}_0)] + [(\mathbf{B}_{\mathbf{P}_1}^T - \mathbf{B}_{\mathbf{P}_0}^T) - \eta(\mathbf{B}_{\mathbf{Q}_1}^T - \mathbf{B}_{\mathbf{Q}_0}^T)]\delta = \mathbf{0} \quad (2.13)$$

2.4 The Algorithm of Non-rigid Registration

The proposed non-rigid registration algorithm works in three basic stages: (a) the template curve is firstly sampled into a discrete point set according to particular approximation tolerance; (b) a mutual distance based weighting method is proposed to establish the correspondence between the sampled points and target cross-sectional points; and (c) the affine combined with FFD transformation is adopted to register the template curve to the cross-sectional points by minimizing the mutual distances between the sampled points and cross-sectional points. The transformation iteratively proceeds with updated correspondence matrix until the maximum iteration times are reached or registration accuracy is satisfied.

2.4.1 Correspondence Matrix

As discussed in Section 2.2, only the one-way directed distance from the target points to the curves are considered in constrained fitting [64]. It works well for initial

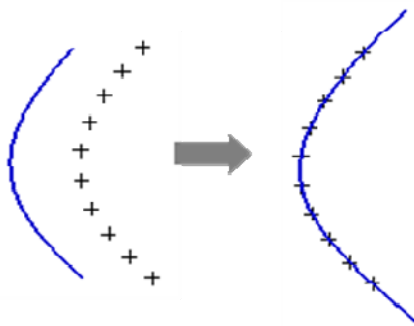


Figure 2.3: The end points of a curve are stretching out by minimizing the one-way directed distance

constructed curves very close to the data points; but when the initial curves are far from the data points, as shown in Figure 2.3, the constrained fitting method might result in

undesired curves whose endpoints are stretching out, even though the distance from the data points to the fitted curves is minimized. Hence, the directed distance from the curves $\mathbf{C}(t) = \{C_k(t)\}$ to the points $\mathbf{Y} = \{Y_j\}$ should also be incorporated in the cost function, i.e.,

$$E(f) = \left(\text{dist}(\mathbf{Y}, f(\mathbf{C}(t))) \right)^2 + \left(\text{dist}(f(\mathbf{C}(t)), \mathbf{Y}) \right)^2 \quad (2.14)$$

In constrained fitting [64], the directed distance $\text{dist}(\mathbf{Y}_j, f(\mathbf{C}(t)))$ is defined as the distance from point \mathbf{Y}_j to its correspondence (closest point) \mathbf{X}_j on curves $\mathbf{C}(t)$ as shown in equation (2.3), which works well if the initial curves are very close to the data points. However, this definition is not always reasonable when the relative position between the curves and data points is poor. Consider a simple example of a single B-spline curve reconstruction as shown in Figure 2.4, all the data points have the same correspondence (closest point) on the initial B-spline curve according to the directed distance defined in constrained fitting [64]. This simple binary correspondence matrix will lead to minimize

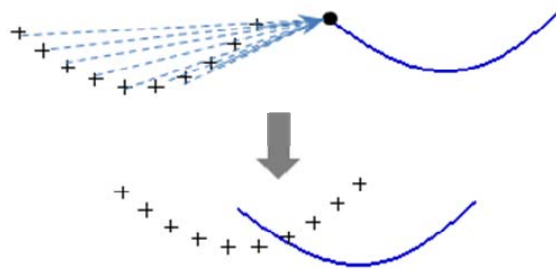


Figure 2.4: All points have the same correspondence on the curve in constrained fitting the sum of squared distance from each data point to the same point on the curve, which is obviously unreasonable for curves fitting.

In order to overcome the drawback of the directed distance definition in constrained fitting, we sample the curves $\mathbf{C}(t)$ into a discrete point set $\mathbf{X} = \{\mathbf{X}_i, i = 1 \dots m\}$ according to a particular approximation tolerance. The directed distance $dist(\mathbf{Y}, f(\mathbf{C}(t)))$ from the target point set $\mathbf{Y} = \{\mathbf{Y}_j, j = 1 \dots n\}$ to the curves $\mathbf{C}(t)$ is then defined approximately as the directed distance from the target point set \mathbf{Y} to the sampled point set \mathbf{X} , i.e., $dist(\mathbf{Y}, f(\mathbf{X}))$.

Let us define:

$$\begin{aligned}
\left(dist(\mathbf{Y}, f(\mathbf{C}(t)))\right)^2 &\triangleq \left(dist(\mathbf{Y}, f(\mathbf{X}))\right)^2 \\
&\triangleq \sum_{j=1}^n \left(dist(\mathbf{Y}_j, f(\mathbf{X}))\right)^2 \\
&\triangleq \sum_{j=1}^n \sum_{i=1}^m \omega_{j,i} \|\mathbf{Y}_j - f(\mathbf{X}_i)\|^2
\end{aligned} \tag{2.15}$$

Where $\left(dist(\mathbf{Y}, f(\mathbf{X}))\right)^2$ is defined as the sum of squared distance from each target point \mathbf{Y}_j to the sampled point set \mathbf{X} , denoted as $\left(dist(\mathbf{Y}_j, f(\mathbf{X}))\right)^2$, which is further defined as the sum of weighted square distance from the target point \mathbf{Y}_j to each sampled point \mathbf{X}_i . $\omega_{j,i}$ is the weight factor satisfying $0 \leq \omega_{j,i} \leq 1$ and $\sum_{i=1}^m \omega_{j,i} = 1$.

Similarly, the squared distance $\left(dist(f(\mathbf{C}(t)), \mathbf{Y})\right)^2$ from the curves $\mathbf{C}(t)$ to the target points \mathbf{Y} is defined as follows:

$$\begin{aligned}
(\text{dist}(f(\mathbf{C}(t)), \mathbf{Y}))^2 &\triangleq (\text{dist}(f(\mathbf{X}), \mathbf{Y}))^2 \\
&\triangleq \sum_{i=1}^m (\text{dist}(f(\mathbf{X}_i), \mathbf{Y}))^2 \\
&\triangleq \sum_{i=1}^m \sum_{j=1}^n \varpi_{i,j} \|f(\mathbf{X}_i) - \mathbf{Y}_j\|^2
\end{aligned} \tag{2.16}$$

where $\varpi_{i,j}$ is the weight factor satisfying $0 \leq \varpi_{i,j} \leq 1$ and $\sum_{j=1}^n \varpi_{i,j} = 1$.

It is noticed that the definitions of directed distance in equations (2.15) and (2.16) have the same forms except different notations of the weight factor. $\omega_{j,i} (i=1\dots m)$ measures the possibility of the source points $\{\mathbf{X}_i\}$ to be the correspondence for each target point \mathbf{Y}_j . In contrast, $\varpi_{i,j} (j=1\dots n)$ measures the possibility of the target points $\{\mathbf{Y}_j\}$ to be the correspondence for each source point \mathbf{X}_i . Different from the constrained fitting where only a one-way binary correspondence matrix is used to minimize the directed distance from the target points to the curves, there are two weighted

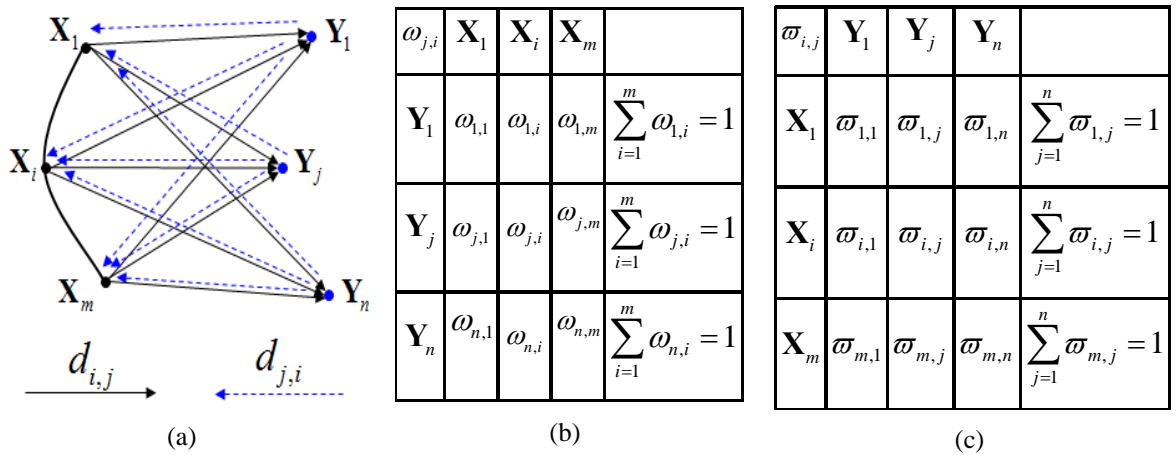


Figure 2.5: (a) Illustration of mutual distance between the source data and the target data, (b) weighted correspondence matrix from the target data to the source data, and (c) weighted correspondence matrix from the source data to the target data

correspondence matrices (See Figure 2.5) utilized to minimize the mutual distances between the curves and target points.

Since the weight factors indicate the relative “importance” of the distance between each corresponding point pairs in the cost function, the following properties should be taken into account when evaluating the weight factors:

(1) The smaller the distance, the larger the weight factor. In other words, there is a higher possibility to be correspondence for two closer points than for two points far from each other.

(2) As the curves are transformed to the data points, the correspondence matrix is converging to a binary matrix, which means that each point will finally have only one correspondence with weight 1. This property guarantees that non-rigid registration is equivalent to constrained fitting when the curves are getting very closer to the target points.

In order to satisfy the above properties, a Gaussian function with respect to the distance is adopted to compute the weight factor. Mathematically,

$$\omega_{j,i} = \frac{1}{\sigma\sqrt{2\pi}} \exp\left(-\frac{d_{j,i}^2}{2\sigma^2}\right) \quad (2.17)$$

where $d_{j,i} = \|\mathbf{Y}_j - \mathbf{X}_i\|$ and σ is registration error which is defined as the averaged sum of squared distance between the source points and target points, i.e.,

$$\sigma = \frac{1}{mn} \sum_j^n \sum_i^m \|Y_j - X_i\|^2 \quad (2.18)$$

It is obvious that $\omega_{j,i}$ is a strictly decreasing function with respect to the distance $d_{j,i}$. Moreover, the Gaussian bell shape is getting sharper with decreasing registration error σ when the curves are moving closer to the target points (See Figure 2.6). Ideally, when the registration error is decreasing toward to zero, all the weight factors with non-zero distance $d_{j,i}$ are converging to zero except the weight factor with zero distance. Hence, the weighted correspondence matrix is approximately reduced to a binary matrix if the curves are very close to the data points, which is one of the assumptions in constrained fitting.

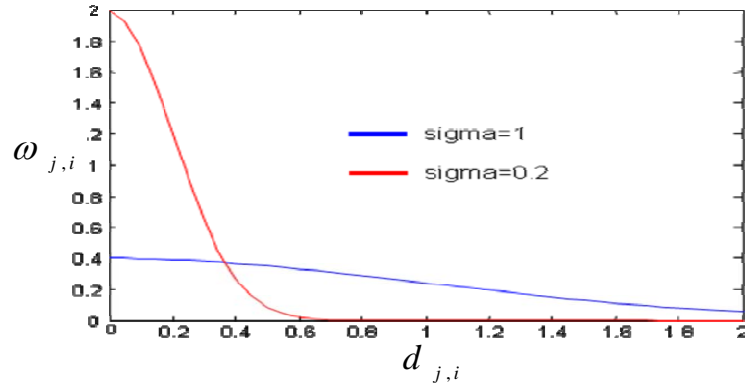


Figure 2.6: The function of weight factor with respect to the distance $d_{j,i}$ and registration error σ

It should be pointed out that the weight factors computed with equation (2.17) will be conducted a row normalization as follows to satisfy the conditions of

$$0 \leq \omega_{j,i} \leq 1 \text{ and } \sum_{i=1}^m \omega_{j,i} = 1.$$

$$\omega_{j,i} \leftarrow \frac{\omega_{j,i}}{\sum_{i=1}^m \omega_{j,i}} \quad (2.19)$$

Similarly, the weight factors $\varpi_{i,j}$ are computed as

$$\varpi_{i,j} = \frac{1}{\sigma\sqrt{2\pi}} \exp\left(-\frac{d_{i,j}^2}{2\sigma^2}\right) \quad (2.20)$$

where $d_{i,j} = \|\mathbf{X}_i - \mathbf{Y}_j\|$.

It is noticed that the initially computed $\varpi_{i,j}$ with equation (2.20) is the same as the initially computed $\omega_{j,i}$ with equation (2.17), but they are normally different after row normalization. $\varpi_{i,j}$ can be normalized as follows:

$$\varpi_{i,j} \leftarrow \frac{\varpi_{i,j}}{\sum_{j=1}^n \varpi_{i,j}} \quad (2.21)$$

2.4.2 Transformation Mechanism

In order to gradually transform and deform the template curve to best fit the target points, the affine combined with FFD transformation is applied to the sampled points of the template curve.

The transformation of a sampled point \mathbf{X}_i on a template curve with parameter t_i can be represented with respect to the curve control vertices as:

$$f(\mathbf{X}_i) = \sum_{k=0}^L N_{k,r}(t_i) f(\mathbf{P}_k) \quad (2.22)$$

which ends up with the following equation by substituting equation (2.5).

$$f(\mathbf{X}_i) = \sum_{k=0}^L N_{k,r}(t_i) (\mathbf{T}\mathbf{P}_k + \mathbf{B}_{\mathbf{P}_k}^T \boldsymbol{\delta}) = \mathbf{T}\mathbf{X}_i + \mathbf{N}_i^T \mathbf{B}_{\mathbf{P}} \boldsymbol{\delta} \quad (2.23)$$

where $\mathbf{B}_{\mathbf{P}} = [\mathbf{B}_{\mathbf{P}_0}^T \quad \mathbf{B}_{\mathbf{P}_1}^T \quad \cdots \quad \mathbf{B}_{\mathbf{P}_L}^T]^T$.

2.4.3 Cost Functions

The cost function of equation (2.14) with mutual directed distances can be written as follows by substituting equation (2.23) into equations (2.15) and (2.16).

$$\begin{aligned} E_1(\mathbf{T}, \boldsymbol{\delta}) &= \sum_{i=1}^m \sum_{j=1}^n \varpi_{i,j} \|f(\mathbf{X}_i) - \mathbf{Y}_j\|^2 + \sum_{j=1}^n \sum_{i=1}^m \omega_{j,i} \|\mathbf{Y}_j - f(\mathbf{X}_i)\|^2 \\ &= \sum_{i=1}^m \sum_{j=1}^n (\varpi_{i,j} + \omega_{j,i}) \|\mathbf{T}\mathbf{X}_i + \mathbf{N}_i^T \mathbf{B}_{\mathbf{P}} \boldsymbol{\delta} - \mathbf{Y}_j\|^2 \end{aligned} \quad (2.24)$$

Since the affine transformation and free-form deformation (FFD) are conducted simultaneously, there is a balancing problem in non-rigid registration. In order to control the transformation step size during non-rigid registration, two penalized terms are imposed on the affine and FFD transformation where the first term is a penalty coefficient α multiplied by trace of the difference between the transformation matrix \mathbf{T} and the identity matrix \mathbf{I} and the second term is a penalty coefficient β multiplied by the displacement $\boldsymbol{\delta}$ of the lattice control points. Mathematically, these two penalized terms can be formulated as:

$$E_2(\mathbf{T}, \boldsymbol{\delta}) = \alpha \cdot \text{trace}(\mathbf{T} - \mathbf{I})^T (\mathbf{T} - \mathbf{I}) + \beta \boldsymbol{\delta}^T \boldsymbol{\delta} \quad (2.25)$$

Smoothness is another important issue for free-form object deformation. Just like real objects, deformation energy is stored in the lattice during non-rigid registration, so minimizing the bending energy is an effective way to control the surface smoothness. The bending energy of the lattice expressed in equation (A.4) can be defined as [72]:

$$E_{lattice} = \int_0^1 \int_0^1 \left\{ \left(\frac{\partial^2 \mathbf{S}}{\partial^2 u} \right)^2 + \left(\frac{\partial^2 \mathbf{S}}{\partial^2 v} \right)^2 + 2 \left(\frac{\partial^2 \mathbf{S}}{\partial u \partial v} \right)^2 \right\} dudv \quad (2.26)$$

By substituting equation (A.5) to (2.26), a concise form of the lattice energy can be obtained:

$$E_{lattice} = \mathbf{V}^T \mathbf{D}^T \mathbf{D} \mathbf{V} \quad (2.27)$$

Where

$$\mathbf{D} = \int_0^1 \int_0^1 \left\{ \frac{\partial^2 \mathbf{B}^T}{\partial^2 u} + \frac{\partial^2 \mathbf{B}^T}{\partial^2 v} + \sqrt{2} \frac{\partial^2 \mathbf{B}^T}{\partial u \partial v} \right\} dudv \quad (2.28)$$

Because the affine transformation does not produce bending energy, a penalty factor γ is applied only to the displacement of lattice control points to control the smoothness during non-rigid registration. By replacing \mathbf{V} with $\boldsymbol{\delta}$ in equation (2.27), this penalized term can be rewritten as:

$$E_3(\mathbf{T}, \boldsymbol{\delta}) = \boldsymbol{\delta}^T \mathbf{D}^T \mathbf{D} \boldsymbol{\delta} \quad (2.29)$$

By synthesizing equations (2.24), (2.25) and (2.29) and taking into account the geometry constraints, the non-rigid registration can be stated as a constrained optimization problem:

$$\begin{aligned}
\text{Minimize: } E(\mathbf{T}, \boldsymbol{\delta}) &= \sum_{i=1}^m \sum_{j=1}^n (\varpi_{i,j} + \omega_{j,i}) \left\| \mathbf{T}\mathbf{X}_i + \mathbf{D}_i^T \mathbf{R}_A \boldsymbol{\delta} - \mathbf{Y}_j \right\|^2 \\
&\quad + \alpha \cdot \text{trace}(\mathbf{T} - \mathbf{I})^T (\mathbf{T} - \mathbf{I}) + \beta \cdot \boldsymbol{\delta}^T \boldsymbol{\delta} + \gamma \cdot \boldsymbol{\delta}^T \mathbf{D}^T \mathbf{D} \boldsymbol{\delta} \\
\text{subject to: } &\quad \mathbf{C}(\mathbf{T}, \boldsymbol{\delta}) = \mathbf{0}
\end{aligned} \tag{2.30}$$

where $\mathbf{C}(\mathbf{T}, \boldsymbol{\delta}) = [C_1(\mathbf{T}, \boldsymbol{\delta}) \ \cdots \ C_K(\mathbf{T}, \boldsymbol{\delta})]^T$ is the vector of geometric constraints.

The parameters of α , β and γ are initialized with empirical values based on the test examples. In order to make the affine transformation in the beginning of non-rigid registration, the initial value of α is normally set much smaller than that of β . Based on our test, the good initial values of the penalty coefficients are set as follows: $\alpha_0 = 0.1$; $\beta_0 = 10$; $\gamma_0 = 10$.

2.4.4 Algorithm

If some of the constraints are dependent, it is necessary to eliminate the dependent constraint equations before solving the optimization problem (2.30). Assume the constraints are independent each other, then the constrained optimization problem (2.30) can be solved with the Lagrangian multipliers method. Denote the Lagrangian multipliers as $\boldsymbol{\lambda}^T \in \mathbf{R}^K$, and then the optimal solution $(\bar{\mathbf{T}}, \bar{\boldsymbol{\delta}}, \bar{\boldsymbol{\lambda}})$ of (2.30) must satisfy the following equations:

$$\begin{cases} \nabla_{\mathbf{T}} E(\bar{\mathbf{T}}, \bar{\boldsymbol{\delta}}) - \bar{\boldsymbol{\lambda}}^T \cdot \nabla \mathbf{C}_{\mathbf{T}}(\bar{\mathbf{T}}, \bar{\boldsymbol{\delta}}) = 0 \\ \nabla_{\boldsymbol{\delta}} E(\bar{\mathbf{T}}, \bar{\boldsymbol{\delta}}) - \bar{\boldsymbol{\lambda}}^T \cdot \nabla \mathbf{C}_{\boldsymbol{\delta}}(\bar{\mathbf{T}}, \bar{\boldsymbol{\delta}}) = 0 \\ \mathbf{C}(\bar{\mathbf{T}}, \bar{\boldsymbol{\delta}}) = 0 \end{cases} \tag{2.31}$$

Since the objective function of (2.30) has a standard quadratic form, the computational efficiency of the optimization problem is mainly determined by the

complexity of the constraint function $C(\mathbf{T}, \boldsymbol{\delta})$. If the constraints are non-linear, the equations (2.31) can be solved with multidimensional Quasi-Newton [73] method. But when $C(\mathbf{T}, \boldsymbol{\delta})$ is a set of linear constraints, for example, the positional and tangent constraints between B-spline curve as shown in equations (2.12) and (2.13), then optimization problem (2.30) turns out to be a convex quadratic programming problem, which can be solved explicitly [74].

As mentioned above, α and β are two key coefficients to control the transformation behavior. Since the initial value of β is set much larger than that of α , the registration is dominated by the affine transformation at the beginning. As iterations proceed, both α and β are gradually decreasing with the rate equal to the ratio of the present registration error to the initial registration error. Finally, the iterations will stop either when the maximum iteration times are achieved or when the registration error is less than the desired registration error. The energy coefficient γ is given with an empirical value.

The steps of the non-rigid registration algorithm for 2D profile curve reconstruction are outlined with pseudo algorithm language as follows:

Set initial values γ_0, α_0 and β_0

Set the maximum iteration times K and the desired registration error ε_0 .

$k = 0$

Sample the template curve into points

Compute the initial registration error σ_0 with equation (2.18)

do

{

Compute and normalize $\omega_{j,i}^k$ and $\bar{\omega}_{i,j}^k$, with equations (2.17), (2.19), (2.20) and (2.21)

Solve equations (2.31) to obtain $\bar{\mathbf{T}}_k$ and $\bar{\delta}_k$

$k = k + 1$

Transform the free-form object and sampled points with equation (2.15) and (2.23)

Update σ_k with equation (2.18)

$$\alpha_k = \alpha_{k-1} \frac{\sigma_k}{\sigma_0}$$

$$\beta_k = \beta_k \frac{\sigma_k}{\sigma_0}$$

} while (($k < K$) & ($\sigma_k \geq \varepsilon_0$))

2.5 Examples and Discussion

The algorithm described above has been implemented in Unigraphics and tested with simulated and real examples. In this section, we will illustrate how this method works more efficiently than constrained fitting for 2D profile curves based geometry modeling. Moreover, we will show that non-rigid registration is superior to constrained fitting when handling noisy or non-uniformly distributed data points.

2.5.1 Time Complexity

The dimensions of the variables in the optimization problem (2.30) are determined by the degrees of freedom (DOFs) of 2D affine combined with FFD transformation, which is $2MN + 6$, where M, N are the number of control points of the lattice along the u, v directions and 6 is the DOFs of affine transformation (see Appendix A). Because the

sampled points of the template curve have to be parameterized with respect to the lattice, the time complexity of the algorithm with respect to the number of control points of the lattice is $O(MN)$. The degree and knot vector of the lattice are decided a priori. For all the test examples, the lattice has number of control points of 4×4 and degree of 3 along the u, v directions with uniform knot vector.

2.5.2 Case Studies

Example 1: Figure 2.7(a) shows data points of six cross sections measured from a used turbine blade with industrial computer tomography (ICT) and a template profile curve consisting of two B-spline curve with positional and tangent constraints on both leading and trailing edges. For each section, the distance between leading edge point and

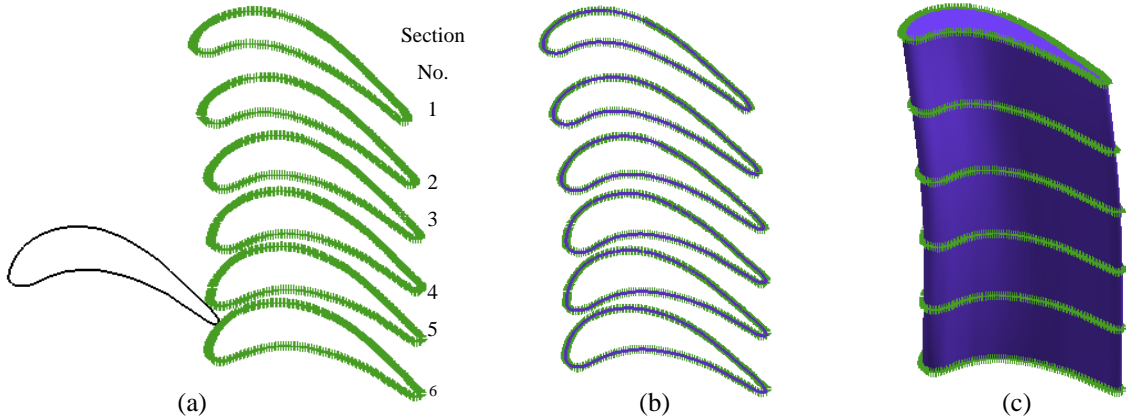


Figure 2.7: (a) Cross sectional points of a physical turbine blade and a template curve, (b) section curves reconstructed with non-rigid registration, and (c) lofted solid model based on the reconstructed curves

trailing edge point is about 20 mm and the maximum thickness is about 5 mm. The accuracy of ICT in this example is 0.1 mm. In order to analyze aerodynamics performance of the used part, it is necessary to reconstruct a CAD model, called as-manufactured model, to recover the physical shape of the blade based on the measured points. In

constrained fitting method [64], the point set of each section is required to be manually segmented in advance, and then the segmented point subsets are carefully sorted and fitted with initial B-spline curves. After that, the constrained fitting module is launched to optimize the profile curves. Finally, the as-manufactured model is reconstructed by lofting all the optimal section curves.

It is noticed that the pre-processing of data points before constrained fitting is very tedious and labor intensive, which greatly reduces the modeling efficiency. In addition, the lofting surface with high smoothness requires all the sections meet the compatibility conditions [65] that all cross-sectional B-spline curves must share the same degree and knot vector. However, each fitted cross-sectional curve based on manually segmented section points normally does not have the same knot vector. Furthermore, the leading edge points between sections are often zigzag along the radial direction (from bottom to top) of the blade, which usually results in poor smoothness of the lofting surface.

Different from the constrained fitting method which requires the initial profile curve close to the data points, non-rigid registration method enables the template profile curve to be automatically transformed and fitted to the cross-sectional points without any data pre-processing such as sorting, segmentation and parameterization. Furthermore, since the same template profile curve is used for all the cross-sectional points, the compatibility conditions are satisfied in a natural way.

Figure 2.8 shows three different stages of non-rigid registration for section No.1 where the dashed black grid is the original lattice; the black curve is the template curve which is composed of two B-spline curves with positional and tangent constraints on both leading and trailing edge; the dashed blue grid is transformed lattice and the blue curve is the transformed curve. Figure 2.8(a) is the initial state before registration where the template profile curve is obtained by slicing the nominal CAD model. After 5 iterations, the template curve is globally registered to the cross-sectional points with affine transformation dominated (See Figure 2.8 (b)). At the last stage, the template curve is best fitted to the point set with FFD dominated and large deformation on the lattice. Twenty iterations of non-rigid registration for this section model are completed successfully within 45 seconds, yielding an optimized profile curve with satisfied tangent constraints on both leading and trailing edges.

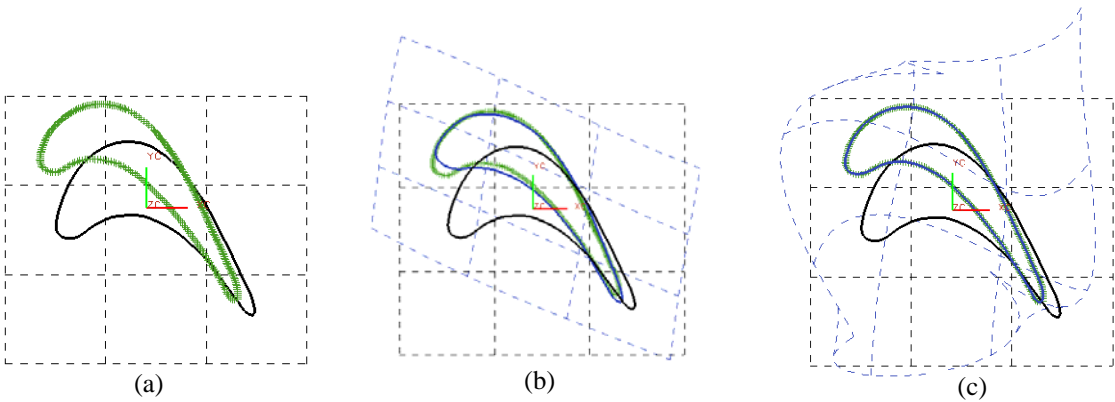


Figure 2.8: Three different stages of 2D non-rigid registration: (a) before registration, (b) after 5 iterations, and (c) after 20 iterations

Figure 2.7(b) and (c) show all the reconstructed cross sectional curves with 20 iterations and the lofted solid model, respectively. Table 2.1 lists the error between each cross-sectional curve and the corresponding point set. The average time used for each

section is about 45 seconds on a desktop with 3.4 GHz Intel Pentium and 2047 MB RAM. In this example, the engineering tolerance of reconstruction error between the curves and points must be less than one half of the measurement error. It is obvious that both of the average and root mean square error are less than 0.05 mm.

Table 2.1: Error report of 2D non-rigid registration for the turbine blade

Section No.	1	2	3	4	5	6
Avg. err. (mm)	0.0164	0.0176	0.0204	0.0227	0.0186	0.0172
RMS err. (mm)	0.0216	0.0229	0.0264	0.0306	0.0240	0.0255

Example 2: This simulated example aims to demonstrate the robustness and superiority of non-rigid registration compared to constrained fitting. As shown in Figure 2.9(a), the initial profile curve consists of one B-spline curve and three line segments with positional continuity between any two adjacent curves. In addition, tangent continuity is

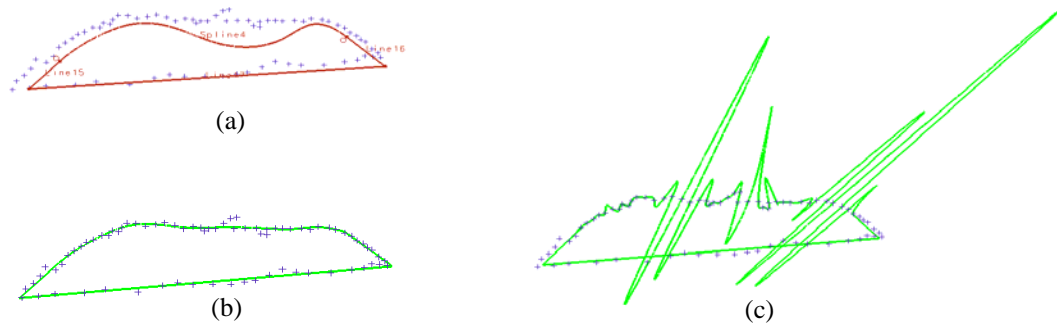


Figure 2.9: (a) Initial profile curve and data points, (b) reconstructed curve with non-rigid registration, and (c) reconstructed curve with constrained fitting method [64]

imposed between the B-spline curve and the two neighboring line segments. The number of control vertices of the B-spline curve is 52. It is noticed that some noise data are added into the cross-sectional points. The size of this profile is about 4.5x0.9 units. Figure 2.9(c) shows the result of constrained fitting method [64], which is the primary reference of this

research. Although the average fitting error is small (0.015 units), there are many wiggles on the B-spline curve, which is unacceptable for quality inspection purpose. In order to take advantage of the proposed non-rigid registration method, all the line segments are re-expressed by B-spline curves with degree of one and number of control vertices of two on both endpoints. Figure 2.9(b) shows a very smooth profile curve produced by non-rigid registration with slightly larger average fitting error (0.024 units), which is acceptable for the noisy data with standard deviation of 0.021 units to the registered curve. The reason of immunity to noise for non-rigid registration is that the movement of the profile curve is driven by the transformation of the lattice with well-controlled deformation behavior.

Example 3: This example consists of seven cross sectional points of a compressor blade measured by laser scanner as shown in Figure 2.10 (a). For each section, the distance between leading edge point and trailing edge point is about 10 units and the

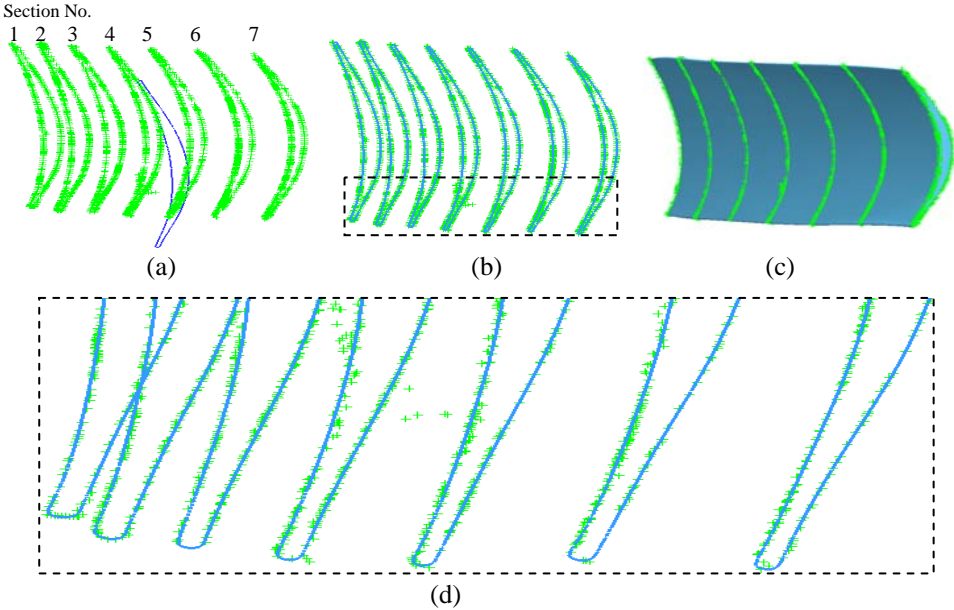


Figure 2.10: (a) Template profile curve and measured points, (b) reconstructed curve with non-rigid registration, (c) lofted surface model, and (d) magnified view of the leading edges of the reconstructed curves

maximum thickness is about 3 units. The template profile curve is composed of two B-spline curves with positional and tangent constraints on both leading and trailing edges. Inherited from the nominal CAD model, the numbers of control points on the convex and concave sides are 84 and 47, respectively. It is obvious that the sectional points in this example are visually noisy, thus it would be very cumbersome for data pre-processing such as noise cleaning, sorting, segmentation and parameterization. However, with non-rigid registration method, the user only needs to pick up the template profile curve and all the cross-sectional points, then the template curve can be automatically transformed and best fitted to the noisy points to reconstruct all the cross-sectional curves. Figure 2.10 (b) shows the reconstructed cross-sectional curves. As shown in the magnified view of the leading edges in Figure 2.10 (d), the noisy points do not have any significant influence on the quality of the reconstructed curves, which demonstrates non-rigid registration method possesses great robustness and immunity to noisy data. Figure 2.10 (c) shows the lofted solid model based on the reconstructed profile curves. Table 2.2 lists the error between each reconstructed curve and the corresponding point set. The average time spent for each section is about 90 seconds on a desktop with 3.4 GHz Intel Pentium and 2047 MB RAM.

Table 2.2: Error report of 2D non-rigid registration for the compressor blade

Section No.	1	2	3	4	5	6	7
Avg. err. ($\times 0.001$ units)	0.091	0.079	0.091	0.135	0.084	0.102	0.086
RMS err. ($\times 0.001$ units)	0.122	0.058	0.107	0.338	0.081	0.099	0.097

Example 4: This is the failed sorting example with constrained fitting as shown Figure 2.1. However, the cross-sectional curve can be successfully reconstructed with non-rigid registration method. As shown in Figure 2.11 (a), the template profile curve is

composed of two B-spline curves with positional and tangent constraints on both leading and trailing edges. The number of cross-sectional points is 410 and the numbers of control vertices on the convex and concave sides are 51 and 17, respectively. The size of the section is about 5x1 units. Figure 2.11 (b) shows the reconstructed curve with average error of 0.014 units after 20 iterations. This example demonstrated the robustness of non-rigid registration when handling non-uniformly distributed point set with gaps or missing points in the profile.

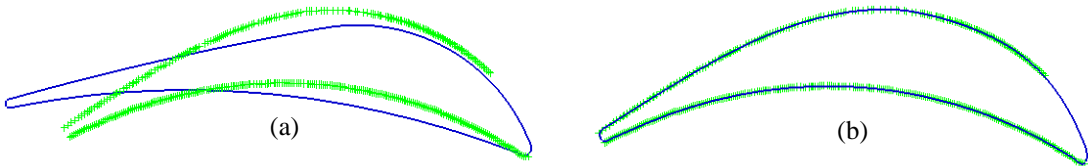


Figure 2.11: (a) Template profile curve and data points, and (b) reconstructed curve with non-rigid registration

2.6 Conclusions and Future Work

We have proposed a non-rigid registration method to reconstruct an as-manufactured geometry CAD model for the development of "Product DNA". With two weighted correspondence matrices based on mutual distances, this method iteratively registers a template curve to measured points by using affine combined with FFD transformation while simultaneously maintaining geometry constraints. Superior to constrained fitting, non-rigid registration does not require initial curves close to data points. In addition, there is no necessity of data preprocessing such as sorting, segmentation and parameterization. Furthermore, non-rigid registration shows stronger robustness to noisy data than

constrained fitting. The simulated and real examples have demonstrated the effectiveness and superiority of the method.

With the proposed method, more geometry constraints into non-rigid registration for more types of part family. Besides positional and tangent constraints, a complex profile curve might have miscellaneous geometry constraints such as parallelism and perpendicularity. Since the geometry is a macro-dimensional measure genome of "Product DNA", the as-manufactured CAD models can be classified into different categories for the purposes of part searching and quality inspection.

CHAPTER 3

SURFACE TEXTURE MODELING AND ANALYSIS WITH B-SPLINE WAVELET

3.1 Introduction

If the dimensional geometry is considered as the macro-measure of the "Product DNA", the surface texture can be viewed as the micro measure of "Product DNA", which uniquely describes the surface tomography of a manufacturing part. It has been well recognized that surface texture is in effect the "fingerprint" of manufacturing process [15]. In order to better understand the relationship between surface texture and manufacturing process, it is a crucial problem of how to characterize and analyze the surface texture with appropriate methods.

Although engineering surfaces of different materials manufactured by different processes normally have different tomography, the surface texture can be basically characterized by some standard terms such as lay, waviness and roughness [13]. Traditionally, the surface texture has been characterized and analyzed with two-dimensional (2D) parameters since the stylus profilometer was invented in 1930s. For instance, the parameters introduced by Whitehouse [20] are one of the most famous parameter set. In addition, parameters defined by different standardization organizations [13][21] are also commonly utilized for surface texture characterization. The 2D

parameters often used for inspection and tolerancing include average roughness R_a , root-mean-squares (RMS) deviation R_q , maximum valley depth R_v , maximum peak height R_p , peak to valley height R_t , ten-point height R_z and bearing ratio t_p [22].

The 2D parameter set is still widely in use in many applications, but it is sometimes inadequate or has difficulties to characterize the surface texture in three-dimension (3D). With the rapid development of 3D measurement technology, there is an increasing need to develop a set of effective 3D parameters for 3D surface texture characterization. Birmingham 14 is one of the most popular and widely accepted parameter set developed under such situations. Taking into account the lessons of parameter rash and parameter redundancy [20], Dong et al. [23]-[26] carefully extended the 2D parameters and elegantly developed a set of 3D parameters to characterize the surface irregularities in the aspects of amplitude, spacing, hybrid properties between amplitude and spacing, and physical functionalities.

Instead of characterizing the surface texture with statistical methods, it is also meaningful to view the surface irregularities as a spatial signal and analyze it in the frequency domain. It has been widely accepted that an engineering surface encodes a range of spatial frequencies. To better understand the surface characteristics in more detailed levels, finer frequency regimes separation is required. Since today's measurement systems already have considerably higher resolutions, modern digital filtering techniques [27][28] make it possible to separate the surface signal into fine frequency bandwidths [75][76]. Raja [29] gave a very comprehensive review of recent advances in separation of surface texture. One common disadvantage of most current

filter banks is the lumping a wide bandwidth into a single entry such as form, waviness and roughness, which limits its applications in close monitoring of manufacturing process and tighter control of surface quality. For this reason, the recent development of wavelets theory and multi-resolution analysis provides a powerful tool to separate the surface texture into finer frequency regimes. There have many research efforts made to apply wavelet transform into engineering surface analysis [16][32]-[35]. Since the wavelet transform has many diverse wavelet basis functions, each of them has different properties and applications. Fu et al. [31] compared 4 types of commonly used wavelets (Haar, Daubechies, Coiflets and Biorthogonal) and concluded that Bior6.8 and Coif4 are good choices for surface analysis in terms of the frequency transmission characteristics.

Milling is one of the most widely used material removal processes in industry. The milled surface quality is very important in many applications such as mating surfaces and assembly surfaces between the parts. Therefore, in order to set optimal milling parameters and thus achieve desired surface quality, it is a critical problem to find the relationship between surface texture and milling process. Montgomery and Altintas [77] derived the theoretical surface roughness of end-milling by considering factors such as cutting tool geometry, feed per revolution and number of teeth on the cutter. Nevertheless, the surface roughness is normally higher than the theoretical value because there often exists vibrations, deflection of workpiece and tool, chipping and some other random factors in actual milling process. Experiments based statistical models provide an alternative way to examine the relationship between surface roughness and manufacturing conditions [78]-[82]. Alauddin [78] created a surface roughness model to determine the optimum cutting conditions by taking into account three major controllable

cutting parameters of cutting speed, feed and axial depth of cut. Besides the three major cutting parameters, Fuh and Wu [79] simultaneously introduced tool nose radius and flank as controllable factors to build a statistical model for surface roughness prediction in end-milling of aluminum. Most recently, Zhang [82] applied Taguchi design method to optimize the cutting parameters to achieve desirable surface roughness. In this experiment design, the tool wear and temperature were considered as noisy factors. Note that all the above reviewed studies only utilized a single frequency parameter, roughness, to characterize spatial distributed surface texture and to map diverse manufacturing factors. However, different manufacturing factors might have different impact on different frequency regimes of the surface texture. Although many types of wavelets are utilized for surface texture separation and analysis, to the best of the authors' knowledge, there is little research conducted to explore how the milling factors affect different frequency regimes of the surface texture.

Motivated by multi-resolution curves presented for curves editing and smoothing [38] in computer graphics, in this research, a multi-level B-spline surfaces based representation is presented to describe the surface texture and then the B-spline wavelet based multi-resolution analysis (MRA) is applied for surface texture decomposition. Based on the measured high-resolution data points of the workpiece, an initial B-spline surface with desired continuity and accuracy is fitted. With B-spline wavelet transform, this surface is decomposed into lower-resolution approximations and higher-frequency details. The initial fitted surface with full description of the surface texture can also be perfectly reconstructed based on the lower-resolution approximations and higher-frequency details by taking inverse B-spline wavelet transform. The advantages of B-

spline wavelet-based MRA for surface texture are five-fold. First, B-spline surface is an industry standard and can express any continuous surfaces; second, the basis function of B-spline surface are piece-wise continuous and have local support property, so it is computational efficient; third, the B-spline wavelet has good amplitude transmission and linear phase property and thus there is no distortion in the filtered surface texture [83]; fourth, it can deal with measured surface with scattered points or partially missing data. Finally, all the standard parameters [25][26] can be computed more easily and accurately based on the multi-level B-spline surfaces representation.

In order to correlate the multi-scaled surface textures to the manufacturing factors, two experiments are conducted for the end-milling process of aluminum. The first experiment aims to explore the impact significance of the milling parameters on different frequency regimes of the milled surface. The purpose of the second experiment is to examine how the tool wear affects different frequency regimes of the surface texture.

The rest of this chapter is organized as follows: the next section gives an overview of wavelet transform and MRA. Section 3.3 illustrates how the multi-level B-spline surfaces are utilized to represent surface texture and how the B-spline wavelet based MRA method is applied for surface texture analysis. In Section 3.4, we present two case studies of end-milling to show how cutting parameters and tool wear affect the different frequency regimes of the surface texture decomposed with the proposed MRA method. Finally, Section 3.5 draws the conclusion.

3.2 Overview of Wavelet Transform and MRA

A wavelet is a finite energy function ψ defined on $\mathbf{L}^2(R)$ space with compact support in both space and frequency domain and whose integral is zero [29].

$$\int_{-\infty}^{+\infty} \psi(x) dx = 0 \quad \text{while} \quad \int_{-\infty}^{+\infty} |\psi(x)|^2 dx < +\infty \quad (3.1)$$

This function is sometimes called mother wavelet. A family of wavelets is obtained by scaling $\psi(x)$ with s and translating it with t :

$$\psi_{s,t}(x) = \frac{1}{\sqrt{s}} \psi\left(\frac{x-t}{s}\right) \quad (3.2)$$

where the factor $s^{-1/2}$ is for the energy normalization, i.e., $\|\psi_{s,t}(x)\| = 1$.

Unlike Fourier analysis with basis functions sine or cosine which have infinite space domain thus only have frequency resolution but no space resolution, the local support property of wavelet function enables wavelet transform to achieve desired resolutions in both space and frequency domains. By scaling and shifting the original waveform function (mother wavelet), wavelet analysis provides a flexible space-frequency window where large scale wavelets are used for lower frequency analysis and small scale wavelets are used for higher frequency analysis. This multi-scaled wavelet transform is also called multiresolution analysis (MRA).

3.2.1 Wavelet Transform

The wavelet transform of a function $f(x) \in \mathbf{L}^2(R)$ at position t and scale s is

$$Wf(t, s) = \langle f(x), \psi_{t,s}(x) \rangle = \int_{-\infty}^{+\infty} f(x) \frac{1}{\sqrt{s}} \psi^* \left(\frac{x-t}{s} \right) dx = f * \bar{\psi}_s(t) \quad (3.3)$$

with $\bar{\psi}_s(x) = \frac{1}{\sqrt{s}} \psi^* \left(\frac{-x}{s} \right)$ and $\psi^*(\bullet)$ is the conjugate complex function of $\psi(\bullet)$.

Since $\hat{\psi}(0) = \int_{-\infty}^{+\infty} \psi(x) dx = 0$, the transfer function $\hat{\psi}$ is a band pass filter [30].

By applying inverse wavelet transform, the original signal can also be reconstructed as [30]:

$$f(x) = \frac{1}{C_\psi} \int_0^{+\infty} \int_{-\infty}^{+\infty} \frac{1}{s^2} Wf(t, s) \psi_{t,s}(x) dt ds \quad (3.4)$$

$$\text{where } C_\psi = \int_0^{+\infty} \frac{|\hat{\psi}(\omega)|^2}{\omega} d\omega < +\infty. \quad (3.5)$$

Note that the scaling parameter s and translating parameter t make the wavelet transform as a flexible windowed transform on the signal. By increasing s , the space spread of the Heisenberg's box [30] increases while the frequency spread decrease. Therefore, the high frequency component of a signal can be examined by decreasing the scaling parameters. When $Wf(t, s)$ is known for the high frequency component with $s < s_0$, the reconstruction of f requires a complement of information corresponding $Wf(t, s)$ with $s > s_0$. This is obtained by a so-called scaling function ϕ with the modulus of its Fourier transform defined by

$$|\hat{\phi}(\omega)|^2 = \int_{s_0}^{+\infty} |\hat{\psi}(s\omega)|^2 \frac{ds}{s}. \quad (3.6)$$

It can be verified that $\|\phi\| = 1$ and $\lim_{\omega \rightarrow 0} |\phi(\omega)|^2 = C_\psi$, so the scaling function can be interpreted as the impulse response of a low-pass filter [30].

Hence, the low frequency approximation of f at scale s is

$$Lf(t, s) = \langle f(x), \phi_{s,t}(x) \rangle = f * \bar{\phi}_s(t) \quad (3.7)$$

where $\phi_{s,t}(x) = \frac{1}{\sqrt{s}} \phi\left(\frac{x-t}{s}\right)$, $\phi_s(x) = \frac{1}{\sqrt{s}} \phi\left(\frac{x}{s}\right)$ and $\bar{\phi}_s(x) = \phi_s^*(-x)$.

By combining equations (3.4) and (3.7), the signal can thus be reconstructed with the low frequency component for $s > s_0$ plus the high frequency details $s < s_0$ [30],

$$f(x) = \frac{1}{C_\psi} \int_0^{s_0} Wf(t, s) * \psi_s(x) \frac{ds}{s^2} + \frac{1}{C_\psi s_0} Lf(t, s_0) * \phi_{s_0}(x) \quad (3.8)$$

3.2.2 Multi-Resolution Analysis (MRA)

A comprehensive review of MRA in computer graphics can be found in Stollnitz's book [84]. The MRA is defined based on a nested linear function spaces $V^0 \subset V^1 \subset \dots \subset V^j \subset \dots \subset V^\infty = L^2(R)$. These subspaces are called scaling spaces with the resolution of the functions in V^j increasing with j . The basis functions of the scaling spaces are called scaling functions as mentioned in the previous section. The wavelet spaces, W^j , are defined as the complement of V^j in V^{j+1} , so we have the following relationships [84]:

$$V^{j+1} = V^j + W^j; \quad V^j \cap W^j = \Phi; \quad (3.9)$$

$$V^{j+1} = V^j + W^j = V^0 + W^0 + W^1 + \dots + W^j = \sum_{i=-\infty}^j W^i \quad (3.10)$$

The basis functions in W^j are called wavelets.

The basis of the scaling space V^j and wavelet space W^j can be represented by row function vectors $\boldsymbol{\varphi}^j(x) = [\varphi_0^j(x) \ \dots \ \varphi_{v(j)-1}^j(x)]$ and $\boldsymbol{\psi}^j(x) = [\psi_0^j(x) \ \dots \ \psi_{w(j)-1}^j(x)]$, where $v(j)$ and $w(j)$ are the dimensions of V^j and W^j , respectively.

The nested subspace V^j is in fact equivalent to the refinement of the scaling functions $\boldsymbol{\varphi}^j(x)$. In other words, there must exist a constant matrix \mathbf{P}^j with dimensions $v(j) \times v(j-1)$ satisfying

$$\boldsymbol{\varphi}^{j-1}(x) = \boldsymbol{\varphi}^j(x)\mathbf{P}^j. \quad (3.11)$$

Since W^{j-1} is another complement subspace in V^j , there exists a $v(j) \times w(j-1)$ matrix \mathbf{Q}^j such that

$$\boldsymbol{\psi}^{j-1}(x) = \boldsymbol{\varphi}^j(x)\mathbf{Q}^j. \quad (3.12)$$

The matrix \mathbf{P}^j and \mathbf{Q}^j are also called scaling and wavelet filters, respectively.

For any function f^{j+1} in V^{j+1} , it can thus be written as the sum of a unique function in the scaling space V^j and the wavelet space W^j . Therefore, the goal of MRA is to decompose a function or a signal into the scaling and wavelet subspaces for relevant details analysis at different level j .

Assume $\mathbf{c}^j = [c_0^j \ \dots \ c_{v(j)-1}^j]^T$ is the coefficient vector associated with an approximation version f^j of function f where $f^j = \boldsymbol{\phi}^j \mathbf{c}^j$, the low resolution approximation \mathbf{c}^{j-1} can be achieved by some form of linear filtering and down-sampling on the entries of \mathbf{c}^j [84]. The process can be expressed as a matrix equation

$$\mathbf{c}^{j-1} = \mathbf{A}^j \mathbf{c}^j \quad (3.13)$$

Apparently, some details are lost during the low resolution approximation of \mathbf{c}^j . In order to capture the lost information, the details \mathbf{d}^{j-1} can be computed by an appropriate matrix \mathbf{B}^j as

$$\mathbf{d}^{j-1} = \mathbf{B}^j \mathbf{c}^j \quad (3.14)$$

Since equations (3.13) and (3.14) decompose a signal into a low-resolution approximation and corresponding details, this process is also called analysis and the matrix pairs \mathbf{A}^j and \mathbf{B}^j are called analysis filters. On the contrary, the high-resolution signal can be reconstructed from the low-resolution approximation and the corresponding details as follows:

$$\mathbf{c}^j = \mathbf{P}^j \mathbf{c}^{j-1} + \mathbf{Q}^j \mathbf{d}^{j-1} \quad (3.15)$$

The reconstruction process is also called synthesis and thus \mathbf{P}^j and \mathbf{Q}^j are called synthesis filters.

Note that equations (3.11) and (3.12) can be combined together with a block matrix notation:

$$[\boldsymbol{\varphi}^{j-1} | \boldsymbol{\psi}^{j-1}] = \boldsymbol{\varphi}^j [\mathbf{P}^{j-1} | \mathbf{Q}^{j-1}] \quad (3.16)$$

According to the definition of MRA, a function approximation f^j at resolution j can be decomposed into a lower resolution approximation f^{j-1} plus the details g^{j-1} , i.e.,

$$f^j = f^{j-1} + g^{j-1} \quad (3.17)$$

where $f^j = \boldsymbol{\varphi}^j \mathbf{c}^j$; $f^{j-1} = \boldsymbol{\varphi}^{j-1} \mathbf{c}^{j-1}$ and $g^{j-1} = \boldsymbol{\psi}^{j-1} \mathbf{d}^{j-1}$.

Substituting equations (3.13) and (3.14) into the above equations, then (3.17) can be reduced into

$$\boldsymbol{\varphi}^j \mathbf{c}^j = \boldsymbol{\varphi}^{j-1} \mathbf{A}^j \mathbf{c}^j + \boldsymbol{\psi}^{j-1} \mathbf{B}^j \mathbf{c}^j \quad (3.18)$$

Write equation (3.18) into block matrix form as

$$[\boldsymbol{\varphi}^{j-1} | \boldsymbol{\psi}^{j-1}] \begin{bmatrix} \mathbf{A}^j \\ \mathbf{B}^j \end{bmatrix} = \boldsymbol{\varphi}^j \quad (3.19)$$

Thus, the combining of equations (3.16) and (3.19) gives us

$$\begin{bmatrix} \mathbf{A}^j \\ \mathbf{B}^j \end{bmatrix} = [\mathbf{P}^{j-1} | \mathbf{Q}^{j-1}]^{-1} \quad (3.20)$$

The equation (3.20) shows that the reconstruction filters can be easily computed by inverting the block matrix of the scaling and wavelet filters.

3.3 B-spline Wavelet based MRA of Surface Texture

It is desirable to construct the wavelets with all the good properties such as orthogonality, compact support and smoothness. However, the orthogonality always comes at the expense of wide support and low smoothness. In order to get an accurate and high resolution approximation of the surface texture, the endpoint- interpolating B-spline wavelets, in which the basis functions are compactly supported but not orthogonal one another, are presented and applied for the surface texture representation and analysis.

3.3.1 Surface Texture Representation

A general non-uniform B-spline basis function with degree p over a non-decreasing knot vector $\mathbf{u} = [u_0, \dots, u_p, u_{p+1}, \dots, u_n, u_{n+1}, \dots, u_{n+p+1}]$ can be defined as the Cox-de Boor recursion formula [3]:

$$N_{i,0}(u) = \begin{cases} 1 & \text{if } u_i \leq u < u_{i+1} \\ 0 & \text{otherwise} \end{cases} \quad (3.21)$$

$$N_{i,p}(u) = \frac{u - u_i}{u_{i+p} - u_i} N_{i,p-1}(u) + \frac{u_{i+p+1} - u}{u_{i+p+1} - u_{i+1}} N_{i+1,p-1}(u); \quad i = 0 \dots n, p = 1, 2, \dots \quad (3.22)$$

Note that $0/0 \equiv 0$ in the above equation.

In order to ensure the B-spline curve or surface interpolate the boundaries, the knot vector is usually normalized in the interval $[0,1]$ and the first and last knots are made $p+1$ repeated times. To make uniformly spaced B-splines, n is set to $2^j + p - 1$ and the knots $u_{p+1}, \dots, u_{2^j+p-1}$ are equally spaced in the interval $[0,1]$ in which j is the level of the piecewise-polynomials formed by the scaling functions $N_{0,p}^j, \dots, N_{n,p}^j$. In other words, j is

the resolution which represents how many times the knot vector space can be subdivided. Thus, the larger the number of B-spline scaling functions, the higher resolution the vector space is.

By summarizing the end-point interpolating and uniform spacing conditions, the knot vector can be written as:

$$\mathbf{u} = [u_0, \dots, u_{2^j+2p}] = \frac{1}{2^j} \left[\underbrace{0, \dots, 0}_{p+1 \text{ times}}, 1, 2, \dots, 2^j - 2, 2^j - 1, \underbrace{2^j, \dots, 2^j}_{p+1 \text{ times}} \right] \quad (3.23)$$

Denote $V^j(p)$ the $\mathbf{L}^2(\mathbf{R})$ space spanned by the B-spline basis functions, i.e. scaling functions, $N_{0,p}^j, \dots, N_{2^j+p-1,p}^j$ with degree p over the knot vector (3.23), and then the nested spaces $V^0(p), \dots, V^j(p)$ are forming a MRA.

Based on the end-point interpolating and uniform spacing knot vector, a B-spline curve with level of m and degree of p can be represented as:

$$C^m(u) = \sum_{i=0}^{2^m+p-1} N_{i,p}^m(u) \mathbf{c}_i^m = \mathbf{N}_p^m \cdot \mathbf{c}^m \quad (3.24)$$

where $\mathbf{N}_p^m = [N_{0,p}^m \quad \dots \quad N_{2^m+p-1,p}^m]$ and $\mathbf{c}^m = [\mathbf{c}_0^m \quad \dots \quad \mathbf{c}_{2^m+p-1}^m]^T$; $N_{i,p}^m(u)$ are the B-spline basis functions; \mathbf{c}_i^m are the control points; and the knot vector is defined by equation (3.23) with the replacement of m to j .

Similarly, a uniform endpoint-interpolating B-spline surface with u level of m and v level of n can be represented by the tensor product as follows:

$$S^{m,n}(u,v) = \sum_{i=0}^{2^m+p-1} \sum_{j=0}^{2^n+q-1} N_{i,p}^m(u) N_{j,q}^n(v) \mathbf{c}_{i,j}^{m,n} \quad (3.25)$$

where p and q are the degrees along u and v directions; $\mathbf{c}_{i,j}^{m,n}$ are the control points; $N_{i,p}^m(u)$ and $N_{j,q}^n(v)$ are the u and v scaling functions defined in equations (3.21) and (3.22).

With the equations (3.24) and (3.25), the 2D surface profile and 3D surface texture can be represented with multiple levels by fitting a B-spline curve or a B-spline surface to the measured 2D or 3D data points, respectively.

3.3.2 Surface Texture Decomposition and Reconstruction

It is necessary to first introduce B-spline wavelet based MRA for 2D surface profile because the MRA of surface texture can be considered as a generalization from 2D to 3D.

In order to decompose a signal into a low-resolution approximation and high-frequency details with equations (3.13) and (3.14), the analysis filters must be computed firstly. However, because the analysis filters are normally dense matrix, it would be a better approach to use equation (3.20) to determine the analysis filters by inverting the synthesis filters, which can be computed more easily.

Because the B-spline scaling functions are known in equation (3.22), the scaling filter \mathbf{P}^j can be easily computed with equation (3.11). The columns of \mathbf{P}^j are sparse due to the local support of the B-spline basis functions.

Note that B-spline wavelets are semi-orthogonal, i.e., the wavelets are orthogonal to scaling functions at the same level, but to each other, except case of degree of 0. Mathematically,

$$\left[\langle \boldsymbol{\varphi}^j, \boldsymbol{\psi}^j \rangle \right] = \mathbf{0} \quad (3.26)$$

Substituting equation (3.12) to (3.26), we have

$$\left[\langle \boldsymbol{\varphi}^{j-1}, \boldsymbol{\varphi}^j \rangle \right] \mathbf{Q}^j = \mathbf{0} \quad (3.27)$$

Since the above homogeneous linear equation system does not have a unique solution, some additional constraints must be imposed. Finkelstein [38] derived the wavelet filter \mathbf{Q}^j (See Appendix B) with minimum number of consecutive non-zero of the columns to achieve the small compact support of the corresponding wavelets. The wavelets basis $\boldsymbol{\psi}^j$ can be constructed with equation (3.12).

Suppose the surface profile is represented by equation (3.24), the $\mathbf{L}^2(R)$ space of V^m is spanned by the scaling functions \mathbf{N}_p^m and the control points \mathbf{c}^m can be considered as coefficients of the scaling functions in general wavelet transform.

The surface profile at level $m-1$ approximation can be formulated as finding new control points \mathbf{c}^{m-1} by employing equation (3.13), i.e,

$$\mathbf{C}^{m-1}(u) = \mathbf{N}_p^{m-1} \cdot \mathbf{c}^{m-1} \quad (3.28)$$

where \mathbf{N}_p^{m-1} is new basis which spans a nested subspace V^{m-1} in V^m .

The lower-resolution approximation comes with the lost details which can be captured as:

$$D^{m-1}(u) = \Psi_p^{m-1} \cdot \mathbf{d}^{m-1} \quad (3.29)$$

where Ψ_p^{m-1} is the basis of the wavelet subspace W^{m-1} with dimension 2^{m-1} orthogonal and complement to V^{m-1} in V^m ; is the coefficients of the high-frequency details.

Combining equations (3.13), (3.14) and (3.20) into block matrix, \mathbf{c}^{m-1} and \mathbf{d}^{m-1} can be computed with the following equation:

$$\begin{bmatrix} \mathbf{c}^{m-1} \\ \mathbf{d}^{m-1} \end{bmatrix} = [\mathbf{P}^m \mid \mathbf{Q}^m]^{-1} \mathbf{c}^m \quad (3.30)$$

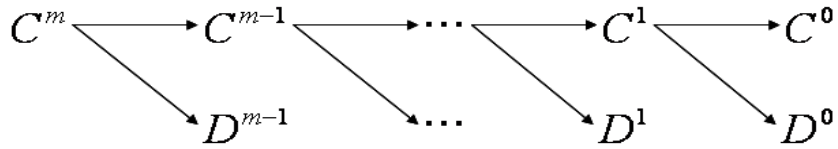


Figure 3.1: Hierarchy of multiresolution curve decomposition

This decomposition process of the surface profile can be recursively proceeded until it reaches level 0. The hierarchy of this process is shown in Figure 3.1.

On the other hand, the original surface profile can be reconstructed based on lower-resolution approximations and corresponding details:

$$\begin{aligned}
C^m(u) &= C^{m-1}(u) + D^{m-1}(u) = \mathbf{N}_p^{m-1} \cdot \mathbf{c}^{m-1} + \boldsymbol{\Psi}_p^{m-1} \cdot \mathbf{d}^{m-1} \\
&= C^0(u) + \sum_{j=0}^{m-1} D^j(u) = \mathbf{N}_p^0 \cdot \mathbf{c}^0 + \sum_{j=0}^{m-1} \boldsymbol{\Psi}_p^j \cdot \mathbf{d}^j
\end{aligned} \tag{3.31}$$

If we substitute equation (3.12) to equation (3.29), the details $D^{m-1}(u)$ turn out to be a B-spline curve with the m level scaling basis functions of \mathbf{N}_p^m and control points $\tilde{\mathbf{d}}^m$ that is obtained by multiplying \mathbf{Q}^m to \mathbf{d}^{m-1} .

$$\begin{aligned}
D^{m-1}(u) &= \boldsymbol{\Psi}_p^{m-1} \cdot \mathbf{d}^{m-1} \\
&= \mathbf{N}_p^m \cdot \mathbf{Q}^m \cdot \mathbf{d}^{m-1} \\
&= \mathbf{N}_p^m \cdot \tilde{\mathbf{d}}^{m-1}
\end{aligned} \tag{3.32}$$

In order to quickly reconstruct the original surface profile $C^m(u)$ from the lowest-resolution approximation $C^0(u)$ and all the details $D^j(u)$, we can recursively substitute equations (3.11) and (3.12) to equation (3.31) until all the scaling functions reach level m . Mathematically,

$$\begin{aligned}
C^m(u) &= \mathbf{N}_p^m \cdot \prod_{k=1}^m \mathbf{P}^k \cdot \mathbf{c}^0 + \sum_{j=0}^{m-1} \mathbf{N}_p^m \cdot \prod_{k=j+2}^m \mathbf{P}^k \cdot \mathbf{Q}^{j+1} \cdot \mathbf{d}^j \\
&= \mathbf{N}_p^m \cdot \left(\prod_{k=1}^m \mathbf{P}^k \cdot \mathbf{c}^0 + \sum_{j=0}^{m-1} \prod_{k=j+2}^m \mathbf{P}^k \cdot \mathbf{Q}^{j+1} \cdot \mathbf{d}^j \right)
\end{aligned} \tag{3.33}$$

The MRA of surface profile can be naturally extended as two dimensional (2D) wavelet transform to deal with surface texture. There are two basic types of 2D wavelet transform: standard and non-standard transform [84].

The standard wavelet transform begins with a one dimensional wavelet transform to the surface along a direction, for example u direction, until the desired low level approximation in u direction is reached. Following that, the surface is decomposed along v direction to a desired level with one dimensional wavelet transform. Different from the standard wavelet transform, the non-standard transform alternates the one dimensional wavelet transform in the u and v direction to the surface. The comparison of standard and non-standard wavelet transform to a surface is shown in Figure 3.2 (a) and (b).

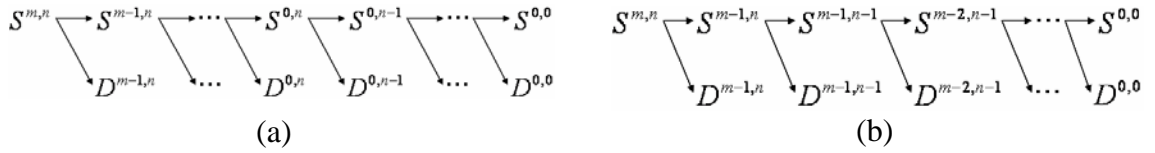


Figure 3.2: Hierarchy of multiresolution surface decomposition (a) standard wavelet transform, and (b) non-standard wavelet transform

The non-standard wavelet transform performs more efficiently than standard wavelet transform in terms of the computational time. However, it requires the same number of levels along u and v directions of the surface. Hence, it cannot be applied to general B-spline surface. In this research, a hybrid wavelet transform is used for the surface texture decomposition. The hybrid wavelet transform performs with the non-standard wavelet transform until one direction reaches the lowest-resolution approximation. If the other direction can still be decomposed, then the standard wavelet transform is performed until it reaches lowest-resolution approximation, too.

Similar to the surface profile reconstruction, the original surface texture $S^{m,n}$ can also be quickly reconstructed from the lowest-resolution approximation $S^{0,0}$ and all the

corresponding details by recursively using equations (3.11) and (3.12) until all the scaling functions reach level m and n in the u and v directions, respectively.

3.3.3 B-spline Wavelet-based MRA Algorithm

Summarizing the previous section, a general algorithm of multi-resolution analysis for surface texture is illustrated as follows.

Input:

A sample of 3D point set $\mathbf{R}_k (k = 0 \dots K)$ measured from a surface texture of a manufactured part.

Algorithm:

Step1. By using equation (3.25), fit or interpolate an initial B-spline surface to the 3D point set with uniform and end-interpolating knot vectors. The number of levels m and n of the surface is determined by desired fitting accuracy and the u, v knot vectors are defined by equation (3.23). Denote the initial surface as $S^{m,n}$.

Step2. Form the synthesis filters \mathbf{P}^j and \mathbf{Q}^j where $j = 0 \dots \max(m, n)$.

Step3. Apply the hybrid 2D wavelet transform to the column vector with equation (3.30) until each direction reaches the lowest (zero) level. Therefore, the initial surface has been decomposed into the lowest level approximation $S^{0,0}$ and higher-frequency details $(D^{m-1,n}, D^{m-1,n-1}, D^{m-2,n-1}, D^{m-2,n-2}, \dots, D^{0,0})$.

Step4. By employing equation (3.15), the surface texture at any level i, j can be easily reconstructed and examined based on the lowest level surface $S^{0,0}$ and corresponding higher- frequency details.

3.4 Case Studies

To demonstrate the effectiveness of the proposed MRA algorithm for surface texture in real applications, end-milling surfaces under different cutting parameters and tool wear conditions are examined. Based on the decomposed lower-resolution approximations and higher-frequency details, the surface texture is separated into three major frequency regimes: surface roughness, surface waviness and surface form. Moreover, regression models are built for these frequency-banded surface responses with respect to the milling parameters and tool wear conditions.

3.4.1 Correlation between Multi-scale Surface Textures and Milling Parameters

As mentioned above, the purpose of this experiment is to apply the B-spline wavelet based MRA to milled surface texture and correlate different frequency regimes to milling parameters.

3.4.1.1 Experiment Setup

Like other studies [77]-[82], the feed rate (f), spindle speed (s), and axial depth of cut (d) are selected as the controllable variables of end-milling. As shown in Table 3.1, a two level factorial experiment was performed for each controllable variable, so there were total eight experimental runs. A Mori Seiki CNC milling center was used for the experiments. The work material selected was Aluminum 6061. The slot-milling was conducted using a two-fluted H.S.S Endmill SEL250 tool with diameter of 12.7mm under dry conditions. Figure 3.3 shows the slot-milling surfaces under different cutting parameters.

Table 3.1: Two-level factorial design

	Spindle Speed (RPM)	Depth of Cut (mm)	Feed Rate (mm/min)
slot 1	500	0.2	50
slot 2	500	0.2	150
slot 3	500	1	50
slot 4	500	1	150
slot 5	1500	0.2	50
slot 6	1500	0.2	150
slot 7	1500	1	50
slot 8	1500	1	150

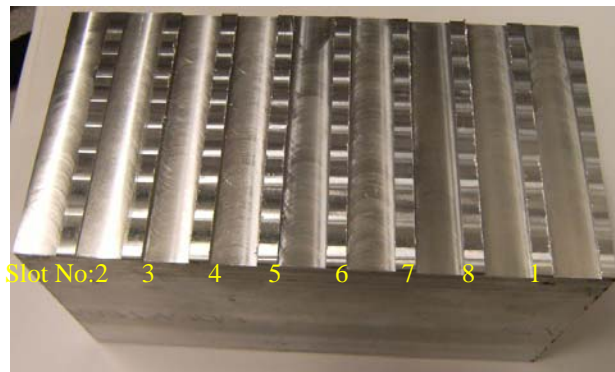


Figure 3.3: Milled slots of the two-level factorial experiment design

3.4.1.2 Results and Analysis

The 3D surface texture of the milled surfaces was measured by a WYKO optical profiler with lateral resolution of $1.65 \mu\text{m}$. Three spots on each milled surface were measured with one in the middle (B spot) and the other two near the edges (A spot and C spot) as shown in Figure 3.4. Figure 3.5 shows the measurement result of the middle spot (B spot) of slot 1. As shown in this figure, the number of measurement points is 368×240 in the x and y directions.

Because the milled surface might have sharp micro-features along the feed marks, the B-spline basis functions with degree of one ($p = 1$), which has positional continuity,

is utilized for MRA of the surface texture. Following the procedure of the MRA algorithm, an initial B-spline surface $S^{8,7}$ with number of controls points of 257X129 is

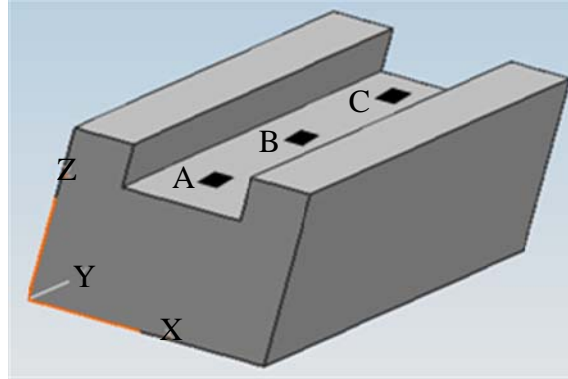


Figure 3.4: measurement locations of three spots

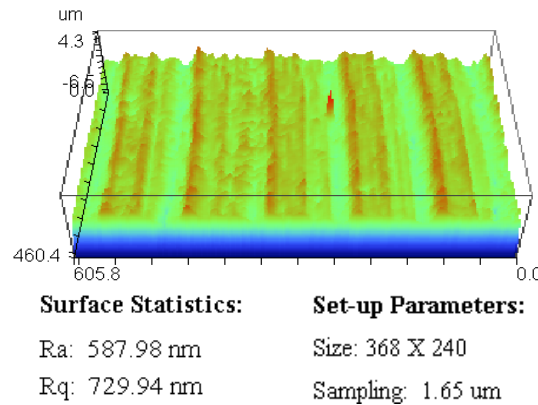
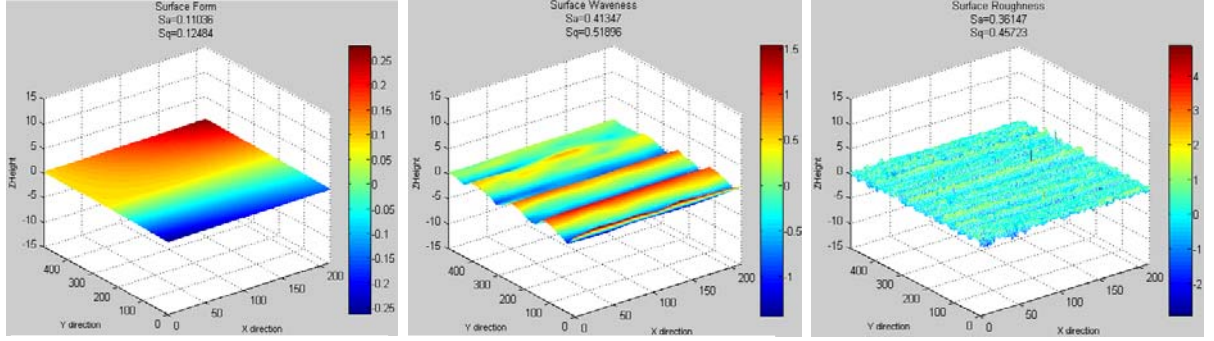


Figure 3.5: spot B of slot 1 from Wyko measurement

firstly reconstructed by interpolating part of the measured points. After fully decomposing the surface texture, we can obtain all the levels of details ($D^{7,7}, D^{7,6}, D^{6,6}, D^{6,5}, D^{5,5}, D^{5,4}, D^{4,4}, D^{4,3}, D^{3,3}, D^{3,2}, D^{2,2}, D^{2,1}, D^{1,1}, D^{1,0}, D^{0,0}$) and the lowest level of approximation ($S^{0,0}$). If the reconstruction is applied to the middle spot of slot 1 by combining the highest four levels of the details ($D^{7,7}$ to $D^{4,3}$) as roughness and the remaining levels of details ($D^{3,3}$ to $D^{0,0}$) as waviness, Figure 3.6 (b) and (c) are obtained. Since the milled surface is flat, the lowest level of approximation $S^{0,0}$ is considered as the form as shown in Figure 3.6 (a).

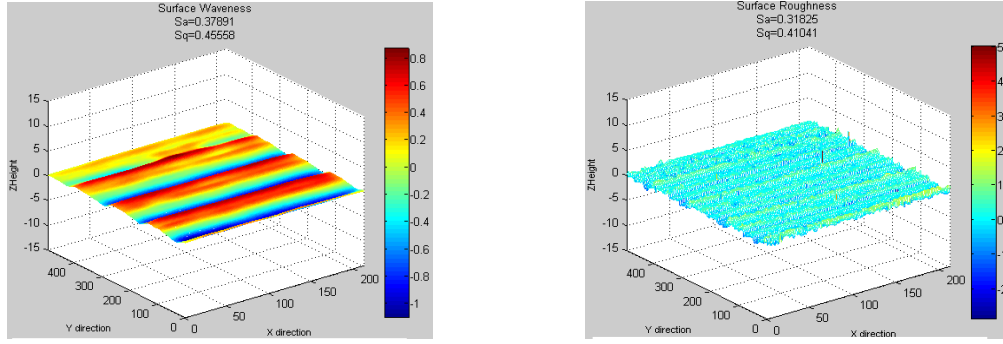


(a) Surface form

(b) Surface waviness

(c) Surface roughness

Figure 3.6: Surface texture decomposition with B-spline wavelet filters



(a) Surface waviness

(b) Surface roughness

Figure 3.7: Surface texture decomposition with B-spline wavelet filters

In order to validate the feasibility the MRA algorithm, the ISO Gaussian low pass filter [85] was implemented and the computed arithmetic average height values (R_a) of roughness and waviness were compared. The impulse response of the 2D Gaussian filter for 3D surface texture is defined as an extension of the 1D Gaussian filter [86]:

$$h(x, y) = \frac{1}{\beta \lambda_{xc} \lambda_{yc}} \cdot \exp \left\{ -\frac{\pi}{\beta} \left[\left(\frac{x}{\lambda_{xc}} \right)^2 + \left(\frac{y}{\lambda_{yc}} \right)^2 \right] \right\} \quad (3.34)$$

where $\beta = \ln 2 / \pi$ and $\lambda_{xc}, \lambda_{yc}$ are the cut-off wavelengths in the x and y directions respectively.

To be consistent with separation of the MRA algorithm, the cut-off wavelengths in x and y directions are both set to $1.65 \times 2^4 = 26.4 \mu m$. Figure 3.7 (a) and (b) shows the separated waviness and roughness of the middle spot of slot 1 with Gaussian filter. It is observed that the separated waviness and roughness between the MRA algorithm and Gaussian filter are correlated well in most locations. However, the results of MRA are normally better than that of Gaussian filter because Gaussian filter often introduces distortion around the edge areas [29].

The computed arithmetic average height value (R_a) of the form can be considered as an indicator of the local flatness of the milled surface. Table 3.2 lists all computed R_a values of all the milled surfaces. The last two columns show the difference of roughness and waviness between the B-spline wavelet based MRA algorithm and the Gaussian filter based method. The differences of R_a values are due to different transmission properties between the B-spline wavelet filter and Gaussian filter. However, all the differences of R_a values are less than or around 20%, which is very common for different filter banks [87].

Table 3.2: R_a values of all the slot surfaces from the two-level factorial experiments

unit: um	Roughness (B-spline wavlet filter)	Waviness (B-spline wavlet filter)	Form (B-spline wavelet filter)	Roughness (Gaussian Filter)	Waviness (Gaussian filter)	Roughness difference	Waviness difference
slot 1 _A	0.40441	0.47875	0.34101	0.36645	0.52946	10.359%	-9.578%
slot 1 _B	0.44484	0.34504	0.26420	0.40223	0.37538	10.593%	-8.082%
slot 1 _C	0.36147	0.41347	0.11036	0.31825	0.37891	13.581%	9.121%
slot1_avg.	0.40357	0.41242	0.23852	0.36231	0.42792	11.389%	-3.621%
slot 2 _A	0.63814	1.97960	0.29384	0.61847	1.81900	3.180%	8.829%
slot 2 _B	0.64047	2.36160	0.80942	0.64935	2.24240	-1.368%	5.316%
slot 2 _C	0.56043	2.23370	0.18983	0.53193	2.07550	5.358%	7.622%
slot 2_avg.	0.61301	2.19163	0.43103	0.59992	2.04563	2.183%	7.137%
slot 3 _A	0.59740	0.46786	0.12509	0.56232	0.42803	6.238%	9.305%

slot 3_B	0.44500	0.68371	0.17717	0.41993	0.60984	5.970%	12.113%
slot 3_C	0.46139	0.42484	0.33949	0.42281	0.47020	9.125%	-9.647%
slot 3_avg.	0.50126	0.52547	0.21392	0.46835	0.50269	7.027%	4.532%
slot 4_A	0.71630	1.46410	0.41353	0.69236	1.21620	3.458%	20.383%
slot 4_B	0.63022	1.31690	0.21321	0.57530	1.15380	9.546%	14.136%
slot 4_C	0.50261	1.63790	0.32920	0.50101	1.50190	0.319%	9.055%
slot 4_avg.	0.61638	1.47297	0.31865	0.58956	1.29063	4.549%	14.127%
slot 5_A	0.37471	0.32419	0.04618	0.35032	0.27312	6.962%	18.699%
slot 5_B	0.40938	0.31202	0.06030	0.37425	0.28353	9.387%	10.048%
slot 5_C	0.41187	0.23285	0.11194	0.36234	0.22606	13.669%	3.004%
slot 5_avg.	0.39865	0.28969	0.07281	0.36230	0.26090	10.033%	11.032%
slot 6_A	0.49972	0.62792	0.05188	0.47242	0.54913	5.779%	14.348%
slot 6_B	0.41695	0.74244	0.23158	0.38584	0.67526	8.063%	9.949%
slot 6_C	0.53688	0.55793	0.10172	0.43626	0.49447	23.064%	12.834%
slot 6_avg.	0.48452	0.64276	0.12839	0.43151	0.57295	12.285%	12.184%
slot 7_A	0.31431	0.11235	0.01493	0.28770	0.11596	9.249%	-3.113%
slot 7_B	0.30559	0.07549	0.03242	0.27283	0.09954	12.007%	-24.163%
slot 7_C	0.33414	0.11742	0.03151	0.29072	0.12469	14.935%	-5.830%
slot 7_avg.	0.31801	0.10175	0.02629	0.28375	0.11340	12.075%	-10.268%
slot 8_A	0.61557	0.46759	0.11005	0.56357	0.40870	9.227%	14.409%
slot 8_B	0.45610	0.70897	0.32054	0.41183	0.68569	10.750%	3.395%
slot 8_C	0.43304	0.78391	0.24507	0.41076	0.68601	5.424%	14.271%
slot 8_avg.	0.50157	0.65349	0.22522	0.46205	0.59347	8.552%	10.114%

3.4.1.3 Regression Models and Conclusions

The R software [36] is used to analyze the R_a values of the separated surface roughness, waviness and form with the MRA algorithm. In order to investigate the relationships between the surface textures and the milling parameters, the R_a values of different frequency regimes are first plotted with respect to the three major milling parameters as shown Figure 3.8. By observing these boxplots, it can be seen that the surface roughness, waviness and form decreases as the spindle speed increases. In contrast, the surface roughness, waviness and form increases as the feed rate increases. Moreover, it seems that the axial depth of cut does not have significant impact on the surface roughness, waviness and form.

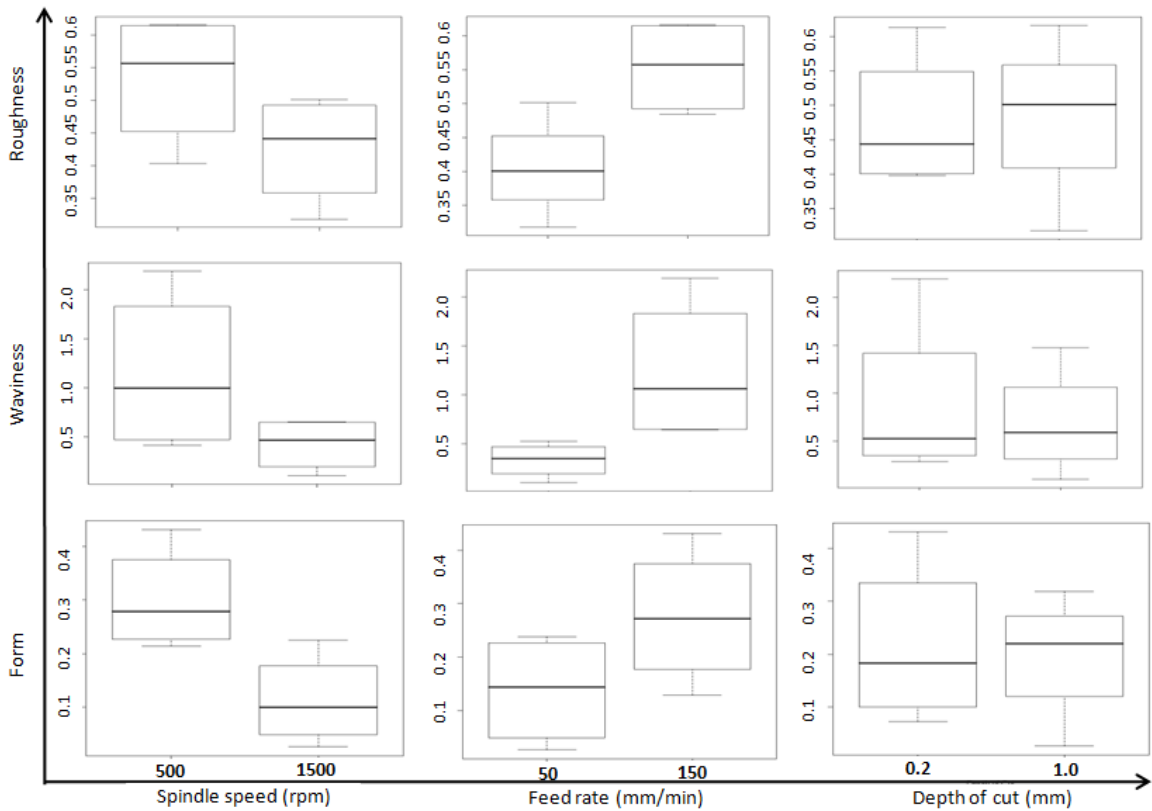


Figure 3.8: Boxplots of the relationship between the surface texture and milling

In order to validate the above observations, the first-order regression models were developed for surface roughness, waviness and form with respect to the three milling variables. Table 3.3 shows the summary of the surface roughness regression model. It can be seen that the axial depth of cut is not a significant variable to the surface roughness (p-value larger than 0.05), which is consistent with our observations. Hence, the axial depth of cut variable is dropped and the re-built regression model of the surface roughness is shown in Table 3.4. It is obvious that both the spindle speed and feed rate have significant impact on the surface roughness. However, the impact of feed rate (99% confidence level) is more significant than that of spindle speed (95% confidence level).

Table 3.3: Full regression model of surface roughness

Coefficients:	Estimate	t value	Pr(> t)
(Intercept)	0.454622	14.048	0.00014***
Spindle speed	-0.107867	-3.333	0.02902*
Depth of cut	0.009368	0.289	0.78661
Feed rate	0.148498	4.589	0.01011*

Signif. codes: 0 '***' 0.001 '**' 0.01 '*' 0.05 '.' 0.1 ' ' 1

Table 3.4: Full regression model of surface roughness without depth of cut

Coefficients:	Estimate	t value	Pr(> t)
(Intercept)	0.45931	18.134	9.37e-06 ***
Spindle speed	-0.10787	-3.688	0.01417 *
Feed rate	0.14850	5.077	0.00384 **

Signif. codes: 0 '***' 0.001 '**' 0.01 '*' 0.05 '.'

The surface waviness and surface form are handled in the same way with the surface roughness. Table 3.5 shows the full regression model of the surface waviness. Similar to the surface roughness model, the axial depth of cut is not a significant variable to the surface waviness. Table 3.6 shows the surface waviness regression model after dropping the axial depth of cut variable. By observing p-values of the variables of spindle speed and feed rate, both of them have significant impact on the surface waviness and also have the same level of confidence (95%).

Table 3.5: Full regression model of surface waviness

Coefficients:	Estimate	t value	Pr(> t)
(Intercept)	0.7945	2.853	0.0463 *
Spindle speed	-0.7287	-2.616	0.0590 .
Depth of cut	-0.1957	-0.703	0.5210
Feed rate	0.9079	3.259	0.0311 *

Signif. codes: 0 '***' 0.001 '**' 0.01 '*' 0.05 '.' 0.1 ' ' 1

Table 3.6: Full regression model of surface waviness without depth of cut

Coefficients:	Estimate	t value	Pr(> t)
(Intercept)	0.6967	3.047	0.0285 *
Spindle speed	-0.7287	-2.760	0.0399 *
Feed rate	0.9079	3.438	0.0185 *

Signif. codes: 0 '***' 0.001 '**' 0.01 '*' 0.05 '.'

Table 3.7: Full regression model of surface form

Coefficients:	Estimate	t value	Pr(> t)
(Intercept)	0.24239	6.345	0.00316**
Spindle speed	-0.18735	-4.904	0.00802**
Depth of cut	-0.02167	-0.567	0.60093
Feed rate	0.13794	3.611	0.02255 *

Signif. codes: 0 '***' 0.001 '**' 0.01 '*' 0.05 '.' 0.1 ' ' 1

Table 3.8: Full regression model of surface form without depth of cut

Coefficients:	Estimate	t value	Pr(> t)
(Intercept)	0.23156	7.528	0.000655***
Spindle speed	-0.18735	-5.275	0.003259**
Feed rate	0.13794	3.884	0.011600 *

Signif. codes: 0 '***' 0.001 '**' 0.01 '*' 0.05 '.' 0.1 ' ' 1

Table 3.7 shows the full regression model of the surface form. Similar to the surface roughness model, the axial depth of cut is not a significant variable to the surface form. Table 3.8 shows the surface form regression model after dropping the axial depth of cut variable. Although both of the spindle speed and feed rate are significant variables to the surface form, the impact of feed rate (95% confidence level) is less significant than that of spindle speed (99% confidence level).

3.4.2 Correlation between Multi-scale Surface Textures and Tool Wear Conditions

The main objective of this experiment is to examine how the tool wear severity affects different frequency regimes of the milled surface in a qualitative sense.

3.4.2.1 Experiment Setup

The same Mori Seiki CNC milling center, work material and cutting tools were used in this experiment. Different from the first experiment, four cutting tools with different severity of tool wear were used to cut the material with the same milling parameters ($f = 150$ mm/min, $s = 1000$ rpm and $d = 0.5$ mm) under dry environment. Since the degree of the tool wear is hard to quantify, the four tools are categorized as new tool, normal tool, slightly worn tool and severely worn tool.

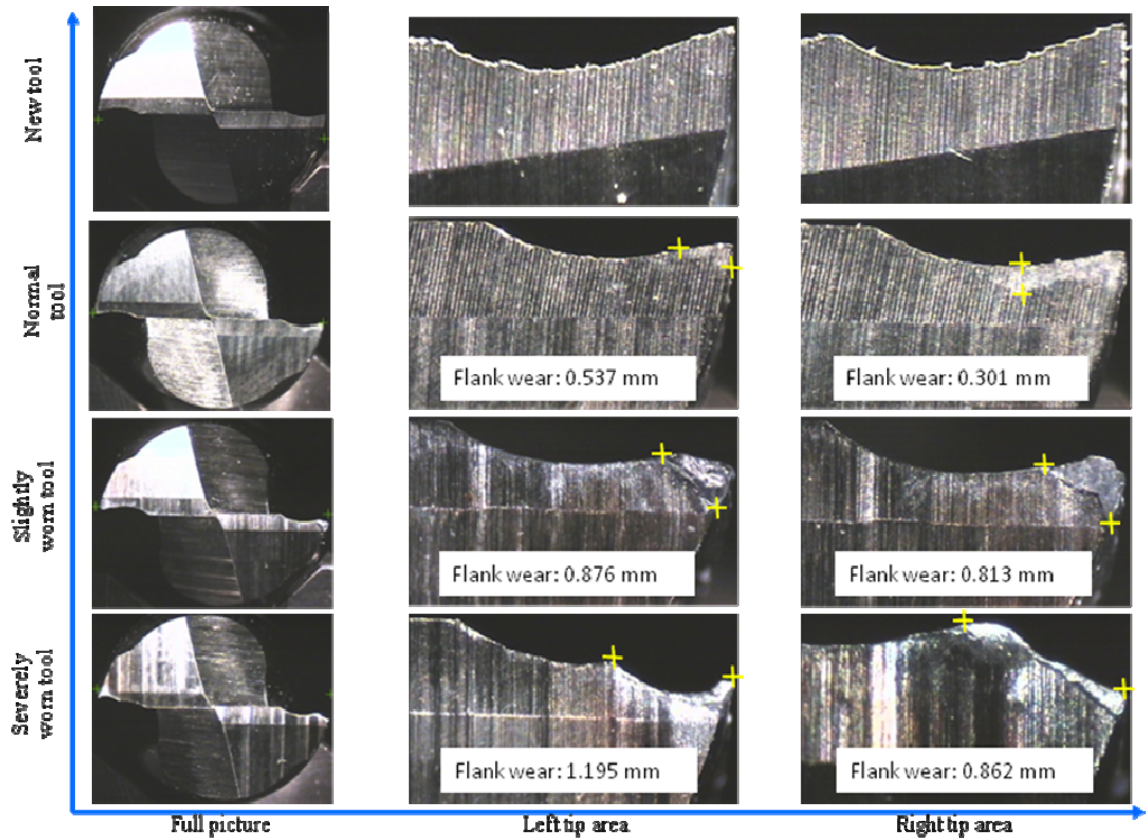


Figure 3.9: Magnified photos of the new tool, normal tool, slightly and severely worn tool

Figure 3.9 shows the magnified photos of these four tools. The number on the pictures indicates the degree of flank wear. The new tool shown in the picture has never

been used before the cutting. The normal tool has milled out aluminum volume of 76mm by 152mm by 6mm under the milling conditions of $f = 150$ mm/min, $s = 1000$ rpm and $d = 0.5$ mm. It can be observed that there are some slight differences around the cutting edge tip areas compared to the new tool. The tool wear of the slightly and severely worn



Figure 3.10: Milled slots with different tools

tool was generated by cutting high speed steel under severe milling conditions of $f = 200$ mm/min, $s = 500$ rpm and $d = 2$ mm. The slightly worn tool has removed material volume of 76mm by 152mm by 6mm. Besides the flank wear, build-up edges and crater wear also appear on the cutting tool. The severely worn tool removed twice of the material volume of the slightly worn tool. Compared to the slightly worn tool, the tool wear areas enlarge and the tool wear degree is more severe. Figure 3.10 shows the four corresponding slots milled by these tools.

3.4.2.2 Result and Analysis

The milled surfaces were measured and handled in the same way with the first experiment. Figure 3.11 shows a measurement example of the middle spot on the milled

surface with new tool. As shown in this figure, the lateral resolution is $1.65 \mu\text{m}$ and the number of measurement points is 1253×1071 in the x and y directions.

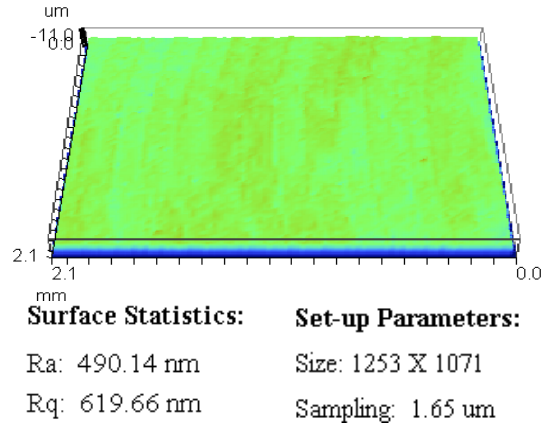
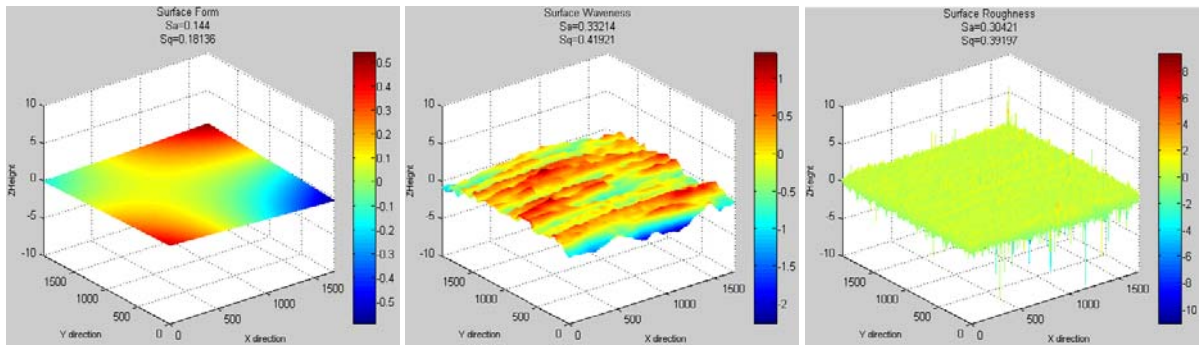


Figure 3.11: Spot B of the slot with new tool



(a) Surface form

(b) Surface waviness

(c) Surface roughness

Figure 3.12: Surface texture decomposition with B-spline wavelet filters

An initial B-spline surface $S^{10,10}$ with degree of one and number of controls points of 1025×1025 is reconstructed by interpolating part of the measured points. Since the number of control points are the same along the u and v directions, the non-standard 2D wavelet transform is applied to decompose the surface texture into high-frequency details and low-resolution approximations. If the five highest levels of the details are combined as the roughness and the five lowest levels

of the details are combined as the waviness, Figures 3.12 (b) and (c) are obtained. The reason we choose level five to separate the roughness and waviness is that the implied cut-off wavelength is $1.65 \times 2^5 = 52.8 \mu\text{m}$, which is close to the theoretical feed per teeth of $150/2/1000 = 75 \mu\text{m}$ in this experiment. Similar to the first experiment, the lowest

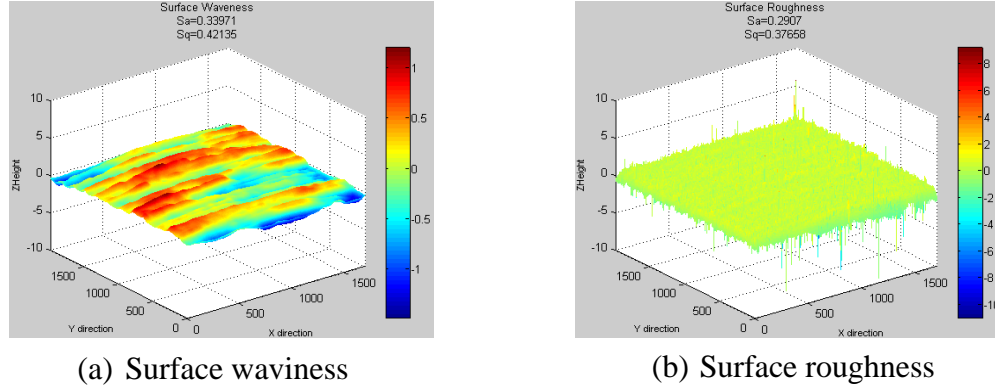


Figure 3.13: Surface texture decomposition with B-spline wavelet filters

level of approximation is considered as the surface form as shown in Figure 3.12 (a).

Figures 3.13 (a) and (b) show the separated waviness and roughness of the same spot of Figure 3.12 with Gaussian filter by setting the cut-off wavelength as $52.8 \mu\text{m}$. Similar to Table 3.2, Table 3.9 lists all the computed R_a values of the milled surfaces in this experiment.

Table 3.9: R_a values of all slot surfaces milled by tools with different tool wears

	Roughness (B-spline wavelet filter)	Waviness (B-spline wavelet filter)	Form (B-spline wavelet filter)	Roughness (Gaussian Filter)	Waviness (Gaussian filter)	Roughness difference	Waviness difference
New Tool_A	0.32717	0.41091	0.10881	0.30635	0.36989	6.80%	11.09%
New Tool_B	0.30421	0.33214	0.144	0.2907	0.33971	4.65%	-2.23%
New Tool_C	0.35044	0.68404	0.17047	0.30742	0.67046	13.99%	2.03%
avg.	0.327273	0.475697	0.141093	0.30149	0.46002	8.55%	3.41%
Normal tool_A	0.32436	0.41291	0.10785	0.30079	0.41206	7.84%	0.21%
Normal tool_B	0.33725	0.39465	0.16309	0.31765	0.4042	6.17%	-2.36%
Normal tool_C	0.34036	0.4841	0.1693	0.29915	0.49192	13.78%	-1.59%

avg.	0.33399	0.430553	0.146747	0.305863	0.43606	9.20%	-1.26%
Slightly worn_A	0.45423	0.86472	0.1549	0.38245	0.80039	18.77%	8.04%
Slightly worn_B	0.38953	0.78892	0.23469	0.3335	0.69539	16.80%	13.45%
Slightly worn_C	0.48979	0.72579	0.17974	0.42024	0.66177	16.55%	9.67%
avg.	0.444517	0.793143	0.189777	0.37873	0.719183	17.37%	10.28%
Severely worn_A	0.55232	1.4238	0.20177	0.44055	1.1938	25.37%	19.27%
Severely worn_B	0.55194	1.4503	0.14883	0.43533	1.2099	26.79%	19.87%
Severely worn_C	0.50488	1.3016	0.19095	0.40394	1.0967	24.99%	18.68%
avg.	0.53638	1.3919	0.180517	0.426607	1.1668	25.73%	19.29%

3.4.2.3 Regression Model and Conclusions

Similar to the logic of the first experiment, the relationship between different frequency regimes of the surface texture and the tool wear severity is plotted as shown in Figure 3.14. From these boxplots, it can be seen that the mean of surface roughness, waviness and form increase as the tool wear is getting worse and worse. However, it seems no big difference between the new tool and normal tool in terms of the roughness

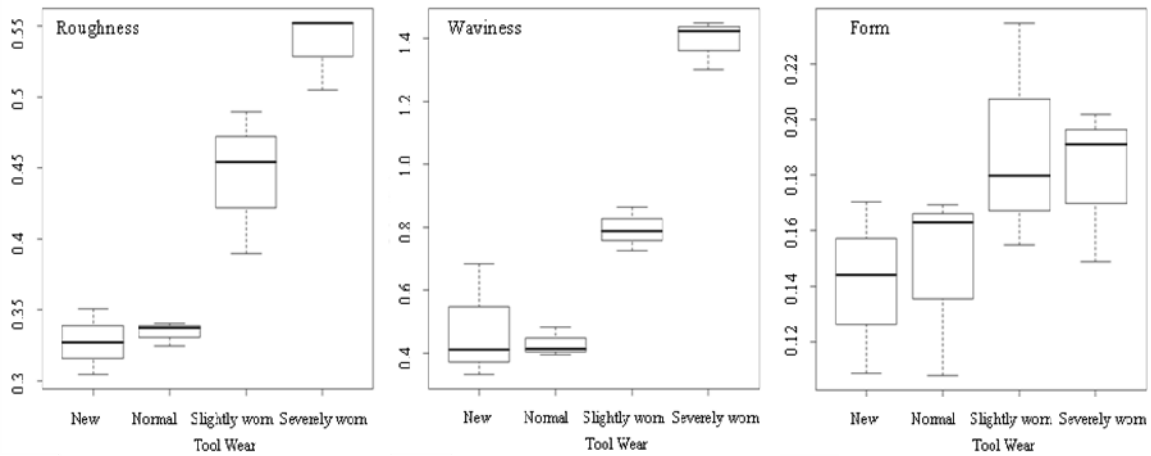


Figure 3.14: Boxplots of the relationship between surface texture and tool wears

and waviness. In fact, it is really hard to tell the form difference between different tools only according to observations on the boxplots.

In order to explore how the tool wear affects surface texture, the One-Way ANOVA method [88] is used to analyze the differences of roughness, waviness and form generated with different tool wears, respectively. Table 3.10 shows the surface roughness model by setting the new tool as the reference. By observing the p-values, it can be seen that the surface roughness of normal tool is not significantly different from that of the new tool while the surface roughness of slightly and severely worn tools are significantly different from (higher than) that of the new tool. We also compute the confidence intervals (CIs) of the difference [88] for pairwise comparisons between the normal tool, slightly and severely worn tools. Because all CIs of the difference in Table 3.11 do not contain zero, we conclude that the surface roughness of slightly worn tools is significantly different from (higher than) that of the normal tool and the surface roughness of severely worn tools is significantly different from (higher than) that of the slightly worn tool in this experiment.

Table 3.10: Regression model of surface roughness

Coefficients:	Estimate	t value	Pr(> t)
(Intercept)	0.327273	18.075	9.01e-08 ***
Normal tool	0.006717	0.262	0.79972
Slightly worn	0.117243	4.579	0.00181 **
Severely worn	0.209107	8.166	3.77e-05 ***
Residual standard error: 0.03136 on 8 degrees of freedom			
Multiple R-Squared: 0.9191,		Adjusted R-squared: 0.8887	
F-statistic: 30.28 on 3 and 8 DF,		p-value: 0.0001021	
Signif. codes: 0 '***' 0.001 '**' 0.01 '*' 0.05 '.' 0.1 ' ' 1			

Table 3.11: CIs of roughness difference between normal tool, slight and severely worn tool

Normal tool	vs.	Slightly worn tool: -0.169572 ~ -0.051480
Normal tool	vs.	Severely worn tool: -0.261436 ~ -0.143344
Slightly worn tool	vs.	Severely worn tool: -0.150910 ~ -0.032818

Table 3.12: Regression model of surface waviness

Coefficients:	Estimate	t value	Pr(> t)
(Intercept)	0.47570	7.563	6.53e-05 ***
Normal tool	-0.04514	-0.508	0.6255
Slightly worn	0.31745	3.569	0.0073 **
Severely worn	0.91620	10.300	6.80e-06 ***
Residual standard error: 0.1089 on 8 degrees of freedom			
Multiple R-Squared: 0.949,		Adjusted R-squared: 0.9299	
F-statistic: 49.64 on 3 and 8 DF,		p-value: 1.628e-05	

Signif. codes: 0 '***' 0.001 '**' 0.01 '*' 0.05 '.' 0.1

According to the One-Way ANOVA analysis results of the waviness as shown in Table 3.12 and Table 3.13, we can draw similar conclusions: The waviness of the new tool and normal tool are significantly smaller than that of slightly worn tool and severely worn tool; the waviness of slightly worn tool is significantly smaller than that of severely worn tool; there is no significant difference of the waviness between the new tool and normal tool.

Table 3.13: CIs of waviness difference between normal tool, slight and severely worn tool

Normal tool	vs.	Slightly worn tool:	-0.5676318 ~ -0.1575482
Normal tool	vs.	Severely worn tool:	-1.1663818 ~ -0.7562982
Slightly worn tool	vs.	Severely worn tool:	-0.8037918 ~ -0.3937082

Table 3.14: Regression model of surface form

Coefficients:	Estimate	t value	Pr(> t)
(Intercept)	0.141093	7.245	8.85e-05***
Normal tool	0.005653	0.205	0.842
Slightly worn	0.048683	1.768	0.115
Severely worn	0.039423	1.432	0.190
Residual standard error: 0.03373 on 8 degrees of freedom			
Multiple R-Squared: 0.3669,		Adjusted R-squared: 0.1295	
F-statistic: 1.546 on 3 and 8 DF,		p-value: 0.2763	

Signif. codes: 0 '***' 0.001 '**' 0.01 '*' 0.05 '.' 0.1 ' ' 1

Table 3.15: CIs of form difference between normal tool, slight and severely worn tool

Normal tool	vs.	Slightly worn tool:	-0.10653834 ~ 0.02047834
Normal tool	vs.	Severely worn tool:	-0.09727834 ~ 0.02973834
Slightly worn tool	vs.	Severely worn tool:	-0.05424834 ~ 0.07276834

Table 3.14 shows the One-Way ANOVA analysis results of the surface form. Please notice that all the p-values of the tools are quite large (larger than 0.1), which means that the surface forms of normal tool, slightly worn and severely worn tool are not significantly different from the new tool. The results of CIs shown in Table 3.15 further verify that the surface forms of these four tools are not significantly different one another because each of the CI contains zero. Another interesting observation on Table 3.14 is that the p-value (0.2763) of the regression is very large compared to 0.05. This means the surface forms of all these four tools are not significantly different from zero, i.e., the milled surfaces are locally flat.

3.5 Conclusions

In this study, a B-spline wavelet-based MRA algorithm has been developed to model and analyze the surface texture genome of "Product DNA". With the proposed algorithm, the surface texture can be efficiently decomposed into lower-resolution approximations and higher-frequency details. Based on the reconstructed surface roughness, waviness and form by combining different frequency regimes, the R_a parameters are computed respectively and compared to that of Gaussian filter. The comparison results have shown the effectiveness and success of the B-spline wavelet-based MRA algorithm.

In addition, two experiments were also performed to correlate different frequency regimes of the surface texture to milling variables and tool wear conditions, respectively. Based on the regression models of surface roughness, waviness and form with respect to

three major milling variables, only the feed rate and spindle speed are found to have significant effect on all the separated frequency regimes of the surface texture. Furthermore, compared to the spindle speed, the feed rate has more significant, the same significant and less significant impact on the surface roughness, waviness and form, respectively.

The One-Way ANOVA analysis of the experiment results with different tool wear degrees shows that the surface roughness and waviness generated by severely worn tool are significantly higher than that by slightly worn tool, which is also significantly higher than that by normal and new tools. Nevertheless, there are no significant differences of surface roughness and waviness between the new tool and normal tool, respectively. Moreover, the tool wear degrees have not shown significant effect on the surface form. All the milled surfaces with different tool wear severities possess local flatness.

With the B-spline wavelet based multi-resolution analysis method, future work can be conducted for faults diagnosis based on the surface texture genome variations within or between the manufacturing processes.

CHAPTER 4

HETEROGENEOUS MODELING BASED ON CROSS-SECTIONAL MASS DENSITY POINTS

4.1 Introduction

Besides dimensional geometry and surface texture, physical attribute is another important component of "Product DNA" for a manufactured part. Traditionally, most of the quality inspection systems focus on the dimensional information and few addresses the issue of product performance both during assembly and in the field of use. In addition to geometric dimensions, the product performance is also determined by other non-dimensional characteristics. For example, the physical attribute of residual stress is a dominant factor to fatigue life; and the mass density distribution of a casting blade plays an important role on its aerodynamic performance. Hence, there is a need to characterize a product based on the integration of all the dimensional and non-dimensional information into the as-manufactured CAD model based "Product DNA" for better quality inspection, process diagnosis and performance analysis.

Heterogeneous object modeling provides an effective way to physical attribute into traditional geometry CAD model, which is mainly focusing on geometry topology and dimensions [89][90]. Heterogeneous parts normally refer to objects with non-uniformly distributed material compositions or microstructures [91][92]. In parallel with

the development of layered manufacturing technology, most of the current studies [40] on heterogeneous object modeling are conducted in a way of forward design of different material compositions in a part. Similar to an r -set object in 3D Euclidean space, Kumar et al. [45][93] proposed an r_m -object to represent the material composition of the CAD model for the purposes of layered manufacturing. Qian et al. [94] adopted an approach of functionally graded material (FGM) distribution to design turbine blades in order to achieve desired performance on different areas of the part.

Besides the "heterogeneities" of compositional variation, the objects with only one material may also possess structural heterogeneity such as anisotropy, porosity and voids. Structural heterogeneity might be intentionally designed for the purpose of application. But in some situations, structural heterogeneity is an undesired property due to imperfections of manufacturing process. For example, in the aerospace industry, the porosity or voids in blades manufactured by casting, forging or laser consolidation has significant influence on part properties such as natural frequency, internal crack, fatigue life, dynamic strain and stress. In order to analyze and predict the performance of a manufactured part, a model with heterogeneous microstructures is required for engineering analysis. The ICT (industrial computer tomography) technology enables to penetrate the manufactured part and produces a stack of 3D intensity images. Because the heterogeneous microstructures have different absorption rate of X-rays, the image pixels are presented with different intensities. With the relationship equation between intensity and mass density, the 3D images can be converted into mass density points. Hence, mass density can be used as a good quantitative indicator of porosities in a manufactured part. Low mass density region has higher probability of voids and vice versa.

Different from the traditional heterogeneous object modeling in a forward design way, this research is addressing the problem of reconstructing a heterogeneous object (called as-manufactured model) based on cross-sectional mass density points measured from a manufactured part. This as-manufactured heterogeneous model has a wide range of applications. First, it can be used for quality inspection by comparing the density distribution of the manufactured part with that of nominal part design. By constantly monitoring the density variation during the product life cycle, people can determine when the part has significant quality change and needs to be repaired or replaced. Second, correlating the density distribution to manufacturing parameters and cutting conditions enables to better understand and diagnose manufacturing process. Third, the as-manufactured heterogeneous model is of great importance for design optimization. The density distribution can be modified to achieve desired functional performance based on relationships between density and functional performance. Last but not least, the as-manufactured heterogeneous model can be served as a linkage to better understand the relationships between manufacturing process and physical performance and thus to reduce the manufacturing cost while achieving desired functional performance.

The rest of this chapter is organized as follows: Section 4.2 briefly reviews related work of heterogeneous object modeling. Section 4.3 introduces representations of the heterogeneous objects. Section 4.4 describes an approach to reconstruct a heterogeneous model based on cross-sectional mass density points. Some examples are presented in section 4.5 to demonstrate the effectiveness of the proposed approach. Finally, section 4.6 draws the conclusion and future work.

4.2 Related Work

Although this research is focusing on reconstructing a structural heterogeneous model based on measured data, some closely related work of forward heterogeneous object design is reviewed here.

In general, heterogeneous object modeling involves a two-step sequential process [44][95]: geometry modeling and physical attributes modeling. Geometry modeling aims to model the shape and spatial topology of the object in 3D Euclidean space E^3 . The commonly used representations of geometry solids are CSG and B-rep [89]. On the other hand, the physical attributes include a wide range of types such as material composition, density, and residual stress, etc. By incorporating the physical attributes into the geometry model, the modeling space is expanded into $E^3 \times A^k$, where A^k is the attribute space with number of dimensions k . Most of the recent research on heterogeneous object modeling is mainly dealing with the attribute of material composition. According to different representation forms of the model, the heterogeneous modeling schemes can be classified into two categories: discrete modeling and continuous modeling.

Voxel-based [41]-[43] and mesh-based [44] model are the most popular representations of discrete modeling. Voxel-based model represents the model with voxels measured by MRI and CAT scanning devices while the mesh-based model employs a collection of polyhedrons to represent the object. Both the voxel-based and mesh-based models are powerful to model object with complex topology. Other advantages include convenience for volumetric rendering, 3D visualization and easy use for engineering analysis. However, due to the discrete representation, it costs huge

storage space if highly accurate model is desired. In addition, it is generally cumbersome to edit or manipulate the model because the operation involves changes for all the voxels or elements.

B-spline based representation is widely used for continuous heterogeneous modeling because of its convenience to edit and modify the control points. Huang et al. [53][96] utilized Bezier curve to model the material distribution of a flywheel and thus to achieve optimal design of functionally gradient materials. Kou and Tan [49] introduced a hierarchical representation to model heterogeneous object in which some primitive objects are were by heterogeneous B-spline curves. Qian et al. [54] extended the geometry B-spline volume to model material composition by adding additional dimensions to the original 3D control points. Recently, Yang et al. [56] presented an integrated design and analysis approach for heterogeneous object realization, which employs a unified design and analysis model based on B-spline representation and allows for direct interaction between the design and analysis model without laborious meshing operation. All the above B-spline based representation assumes that the geometry and physical attributes share the same set of control points, degree and knot vector. This tight coupling representation limits design flexibility when the geometry and physical attributes have different requirements on the number of control points. Martin and Cohen [57] proposed an alternative approach to represent volumetric data based on tri-variate NURBS, in which the geometry and the attributes are represented by independent tri-variate volumes except sharing the same parametric domain.

Although there are many methods proposed for heterogeneous object modeling, most of the studies are performed in a forward design way that converts design intent into

a product model. To the best knowledge of the authors, there is no prior work addressing the problem of reconstructing an as-manufactured heterogeneous model based on physical attribute data. Different from reverse engineering of geometry model, new issues might occur in reconstructing an as-manufactured heterogeneous model. For example, constraints might be needed to ensure the non-negativity of physical attributes.

In this research, a systematic approach is proposed to reconstruct a heterogeneous model based on cross sectional mass density points obtained by converting the intensity images from ICT. Because resolution requirements are different for geometry and mass density, decoupled B-spline representations are adopted to model the object. First, the geometry boundary curves are reconstructed by morphing the template curves to the cross-sectional profile points. Second, the cross-sectional geometry surfaces are reconstructed based on the boundary curves. Following that, the scattered density points of each section are parameterized and encoded into the geometry surfaces with a constraints based multi-resolution approach. Finally, all the density encoded surfaces are lofted into a 3D heterogeneous solid model. There are three important aspects in our approach: (a) decoupled B-spline representations are adopted to model the geometry and mass density; (b) multi-resolution based method is used to model density attributes; and (c) boundary constraints are considered when incorporating density information into the geometry model.

4.3 Heterogeneous Object Representations

As mentioned earlier, the heterogeneous model space is $E^3 \times A^k$, where E^3 is the 3D Euclidean space and A^k is the physical attribute space with number of dimensions k . In this research, k equals 1 because only mass density is considered. The heterogeneous objects include mass density point, mass density surface and mass density solid.

4.3.1 Mass Density Point

A mass density point \mathbf{Q} can be considered as a four dimensional point which is represented by its coordinates plus a mass density ρ , i.e., $\mathbf{Q} = [x \ y \ z \ \rho]^T$.

4.3.2 Mass Density Surface

The mass density surface is a mapping f from the parametric domain $\Omega(u, v)$ to the heterogeneous space $E^3 \times A^1$, i.e., $f: \mathbf{R}^2 \rightarrow \mathbf{R}^3 \times \mathbf{R}^1$. By decoupling the geometry and mass density information, the geometric part represented by a normal B-spline surface is defined as follows [4]:

$$\begin{aligned} \mathbf{S}(u, v) &= \sum_{i=0}^{m_g} \sum_{j=0}^{n_g} N_{i,p_g}(u) N_{j,q_g}(v) \mathbf{P}_{i,j} \\ &\triangleq \mathbf{N}_g^T \mathbf{P} \end{aligned} \quad (4.1)$$

$$\text{Where } \mathbf{P} = \left[\mathbf{P}_{0,0} \quad \cdots \quad \mathbf{P}_{m_g, n_g} \right]^T \text{ and } \mathbf{N}_g = \left[N_{0,p}(u) N_{0,q}(v) \quad \cdots \quad N_{m_g,p}(u) N_{n_g,q}(v) \right]^T.$$

$\mathbf{P}_{i,j} \in E^3$ are the geometric control points and m_g, n_g are the number of geometric control points along u, v parametric directions, respectively. $N_{i,p}(u)$ and $N_{j,q}(v)$ are the B-spline basis functions with degree of p_g and q_g in the u and v directions, respectively. The B-

spline basis functions are defined on a non-decreasing sequence of real numbers of

u_0, \dots, u_{m+p+1} :

$$N_{i,0}(u) = \begin{cases} 1 & \text{if } u_i \leq u < u_{i+1} \\ 0 & \text{otherwise} \end{cases} \quad (4.2)$$

$$N_{i,p}(u) = \frac{u - u_i}{u_{i+p} - u_i} N_{i,p-1}(u) + \frac{u_{i+p+1} - u}{u_{i+p+1} - u_{i+1}} N_{i+1,p-1}(u) \quad (4.3)$$

where $\mathbf{U} = \{u_0, \dots, u_{m+p+1}\}$ is called the knot vector.

The density part of the surface is defined independently with similar B-spline form as the geometry except different control points, degree and knot vector.

$$\begin{aligned} D(u, v) &= \sum_{i=0}^{m_d} \sum_{j=0}^{n_d} N_{i,p_d}(u) N_{j,q_d}(v) d_{i,j} \\ &\triangleq \mathbf{N}_d^T \mathbf{D} \end{aligned} \quad (4.4)$$

Where $d_{i,j} \in A^1$ are the density control points and all other notations are analogous to the geometry part.

4.3.3 Mass Density Solid

Similarly, a mass density solid can be represented by two separated tri-variate B-spline volumes. The tri-variate B-spline volume is an extension of bivariate B-spline surface with an additional parametric direction of w . The geometry part is represented as:

$$\begin{aligned} \mathbf{V}(u, v, w) &= \sum_{i=0}^{m_g} \sum_{j=0}^{n_g} \sum_{k=0}^{l_g} N_{i,p_g}(u) N_{j,q_g}(v) N_{k,r_g}(w) \mathbf{P}_{i,j,k} \\ &\triangleq \mathbf{N}_g^T \mathbf{P} \end{aligned} \quad (4.5)$$

where $\mathbf{P}_{i,j,k}$ are the geometric control points of $(m_g + 1) \times (n_g + 1) \times (l_g + 1)$ mesh. The B-spline basis functions $N_{i,p}(u)$, $N_{j,q}(v)$ and $N_{k,r}(w)$ have similar definitions with the mass density surface.

On the other hand, the mass density part is represented by an independent scalar tri-variate B-spline volume as:

$$D(u, v, w) = \sum_{i=0}^{m_d} \sum_{j=0}^{n_d} \sum_{k=0}^{l_d} N_{i,p_d}(u) N_{j,q_d}(v) N_{k,r_d}(w) d_{i,j,k} \quad (4.6)$$

$$\cong \mathbf{N}_d^T \mathbf{D}$$

where $d_{i,j,k}$ are the density control points.

The decoupled representations enable us to model geometry and mass density with different resolutions. Normally, the mass density data from ICT has much more volume than the geometry profile points measured by CMM. In this situation, huge storage space can be saved by using less number of control points to model the geometry. In addition, all the algorithms of B-spline based geometry modeling can be extended to handle the mass density modeling with slight modifications.

4.4 Proposed Approach

The proposed approach to reconstruct a mass density solid based on cross-sectional ICT images consists of four basic stages: (a) conversion and analysis of intensity images to mass density points; (b) reconstruction of cross-sectional geometric surface; (c) reconstruction of cross-sectional mass density surface; and (d) mass density solid lofting.

4.4.1 Intensity Images and Mass Density Points

Industry computer tomography (ICT) is widely used for non-destructive inspection, density measurement and defects detection [97]. A cone-beam CT system mainly consists of four basic functional units: micro-focus x-ray tube, a precise sample fixture, a flat panel digital detector and a computer system for image reconstruction. A schematic CT system is shown in Figure 4.1. When x-ray transits the rotating object, the digital detector records the attenuated intensity, which can be used to reconstruct cross-sectional grayscale images with proper algorithms. Because the intensity attenuation is related to the material's absorption rate and density, the grayscale image can be processed to obtain cross-sectional mass density points.

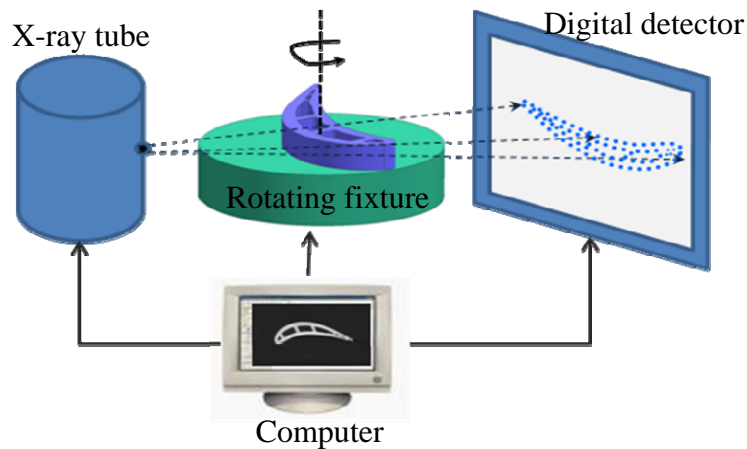


Figure 4.1: Schematic cone-beam CT system

The ICT system with high resolution has been applied to measure the samples. The system consists of a highly stable micro-focus x-ray tube with voltage of 420kv and a high resolution surface detector of 500X500 pixels. The pixel size is 0.0762 mm (0.003 inch). The output of the reconstruction is a standard DICOM format image. The system

allows scanning objects with maximum dimensions of width and height 76.2X76.2 mm (3X3 inches).

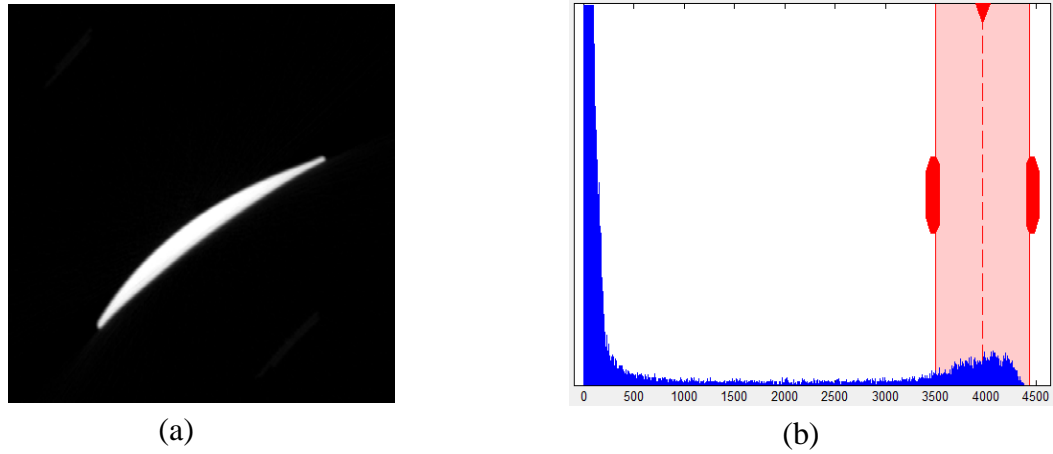


Figure 4.2: (a) Intensity image of an airfoil section, and (b) intensity histogram of the image

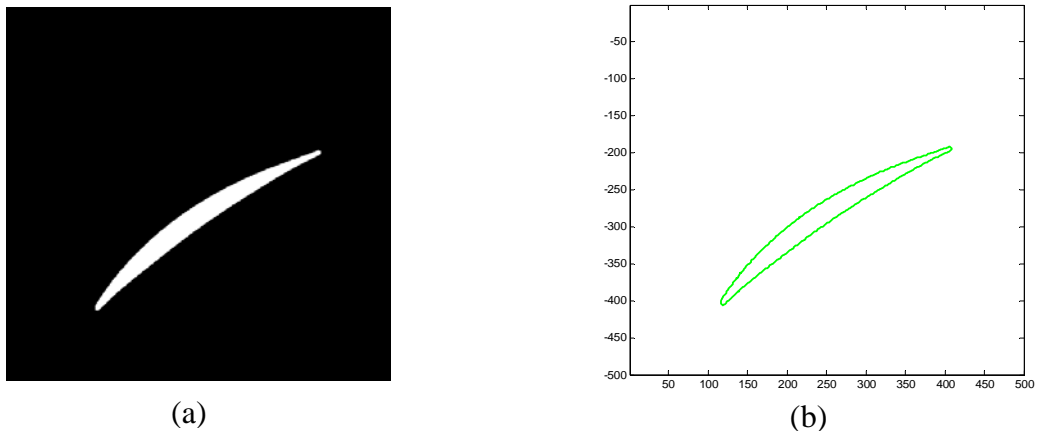


Figure 4.3: (a) Binary image of the airfoil section, and (b) boundary image of the airfoil section

Figure 4.2(a) shows a reconstructed intensity image of a compressor blade airfoil section. Figure 4.2(b) is the intensity histogram of the image. As we can see, most of the pixels are concentrated in the intensity range of 0 to 500, which corresponds to the black

area of the image. On the other hand, the pixels of the blades section are concentrated in intensity range from 3500 to 4500, which corresponds to the bright area of the image. By using the function of *im2bw* in Matlab, the original image can be converted into a binary image as shown in Figure 4.3(a). Furthermore, the boundary image (Figure 4.3(b)) is extracted based on the binary image through the function of *bwboundaries* in Matlab.

If we assume the mass density be linear with the pixel intensity and the nominal mass density of the compressor blade be 8.000 g/cm^3 with respect to the average intensity of 3600 of the white pixels in the binary image, the binary intensity image can be converted into a set of mass density points as shown in Figure 4.4(a). There are totally 7242 mass density points for this section with maximum density of 8.858 g/cm^3 , minimum density of 4.005 g/cm^3 , average density of 8.000 g/cm^3 and standard deviation

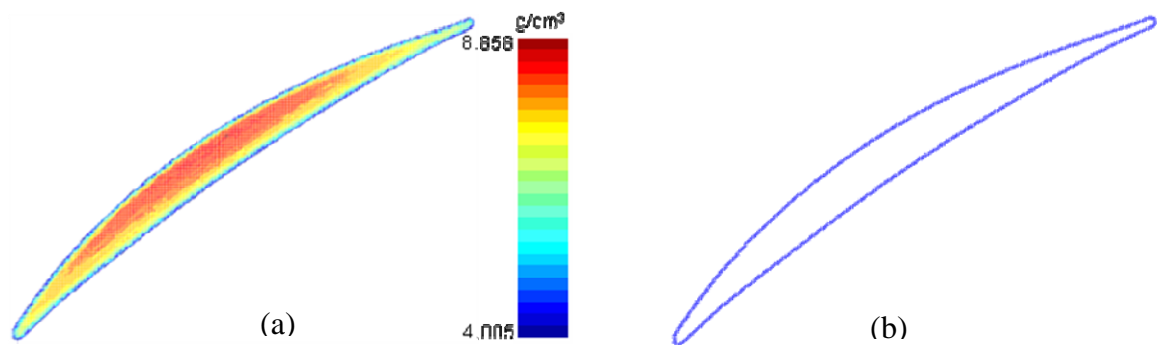


Figure 4.4: (a) Mass density points of the airfoil section in UG, and (b) boundary points displayed in UG

of 1.404 g/cm^3 . Figure 4.4(b) shows the boundary points displayed in Unigraphics (UG).

4.4.2 Geometric Surface Reconstruction

In order to obtain a final lofted heterogeneous solid, a series of cross-sectional heterogeneous surfaces are required to be firstly reconstructed based on the cross-sectional boundary points and interior mass density points. A sequential modeling process is adopted to reconstruct the heterogeneous surface: geometry surface reconstruction and mass density surface reconstruction. This sub-section focuses on reconstructing cross-sectional geometry surfaces based on boundary points.

Because the mass density points of each section are coplanar, the cross-sectional geometric surface is purely determined by the boundary points. To ensure the compatibility conditions that all cross-sectional B-spline curves share the same degree and knot vector, a template curve based non-rigid registration method [98] is employed to

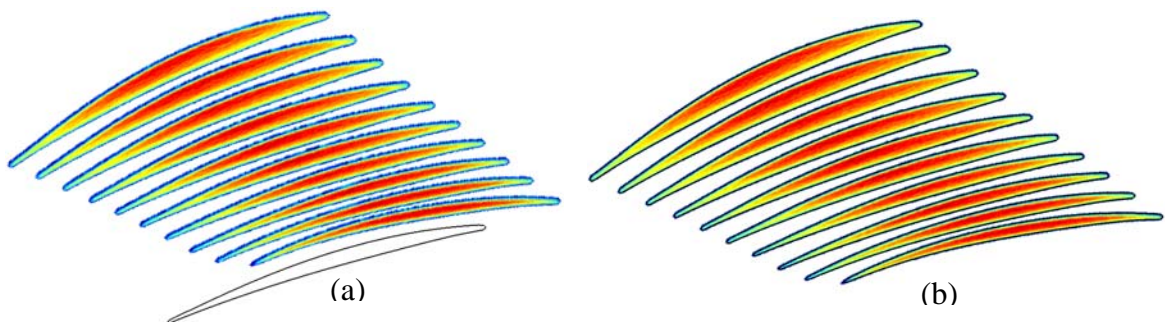


Figure 4.5: (a) Template curve and cross-sectional density points, and (b) reconstructed boundary curves with non-rigid registration method

reconstruct all the profile curves based on the boundary points. Figure 4.5(a) shows an example that consists of a template curve and 10 sections of mass density points. The template curve is composed of 4 B-spline curves with positional and tangent constraints applied between any two adjacent curves. The curves on the leading edge and trailing edge have number of control points of 7 and the curves on the convex and concave sides

have number of control points of 15, respectively. With the non-rigid registration method, the template curve is automatically transformed and morphed to best fit all the cross-sectional boundary points. Figure 4.5(b) shows all the reconstructed boundary curves associated with mass density points.

Different from homogeneous lofting which is directly performed on the boundary curves, heterogeneous lofted solid is reconstructed based on heterogeneous surfaces. Therefore, cross-sectional planar geometric surfaces are to be created. Given 4 boundary B-spline curves, a bilinearly blended Coons surface can be easily constructed [4]. Because all the boundary curves are derived from the same template curve, all the

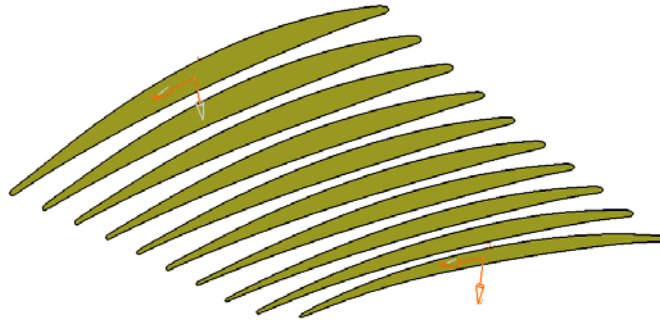


Figure 4.6: Reconstructed cross-sectional Coons surfaces based on the boundary curves reconstructed Coons surfaces have the same degree, number of control point and knot vector in both u, v parametric directions. The satisfaction of this compatibility condition is critical to obtain a final solid model with high quality. Figure 4.6 shows all the reconstructed cross-sectional Coons surfaces of the compressor blade example.

4.4.3 Mass Density Surface Reconstruction

The second step of the sequential modeling is to reconstruct a mass density surface based on the cross-sectional geometric surfaces and mass density points.

4.4.3.1 Initial Mass Density Fitting

As mentioned in section 3, the decoupled B-spline representation (equation 4.4) is used to model the scattered mass density points for each section. Given a set of scattered mass density points $\mathbf{Q} = \{\mathbf{Q}_k\}, k = 0 \dots K$, the objective of mass density fitting is to get an optimal representation of $D(u, v)$ which minimizes the fitting errors as well as keeping smooth density change. The least-square cost function can be formulated as:

$$\begin{aligned} E(p_d, q_d, \mathbf{U}, \mathbf{V}, \mathbf{D}) &= \sum_{k=0}^K \left\| \sum_{i=0}^{m_d} \sum_{j=0}^{n_d} N_{i,p_d}(u_k) N_{j,q_d}(v_k) d_{i,j} - \rho_k \right\|^2 \\ &= \sum_{k=0}^K \left\| \mathbf{N}_{d,k}^T \mathbf{D} - \rho_k \right\|^2 \end{aligned} \quad (4.7)$$

As shown in the above cost function, the optimization variables include the degrees, knot vectors and control points of the density surface. Since the cross-sectional geometric surface is already available, the degree and knot vector of the mass density surface can be initially chosen as the same as that of the geometric surface. Moreover, the parameters u_k and v_k of the mass density point \mathbf{Q}_k can be computed by locating the nearest point on the geometric surface. This way, the density control points \mathbf{D} are the only variables to be considered and the initially fitted mass density surface will share the same parametric domain and have the same degree, knot vector and number of control points with the geometric surface. The optimization is reduced as:

$$\text{Minimize : } E(\mathbf{D}) = \sum_{k=0}^K \left\| \mathbf{N}_{d,k}^T \mathbf{D} - \rho_k \right\|^2. \quad (4.8)$$

The above least-square optimization problem can be explicitly solved by setting the first derivatives to zero, i.e.

$$\sum_{k=0}^K \mathbf{N}_{d,k} \mathbf{N}_{d,k}^T \mathbf{D} - \sum_{k=0}^K \rho_k \mathbf{N}_{d,k} = 0. \quad (4.9)$$

It can be easily proved that $\sum_{k=0}^K \mathbf{N}_{d,k} \mathbf{N}_{d,k}^T$ is a positive semi-definite matrix in that

$\mathbf{x}^T \sum_{k=0}^K \mathbf{N}_{d,k} \mathbf{N}_{d,k}^T \mathbf{x} \geq 0$ for any vector \mathbf{x} . Because the number of scattered mass density

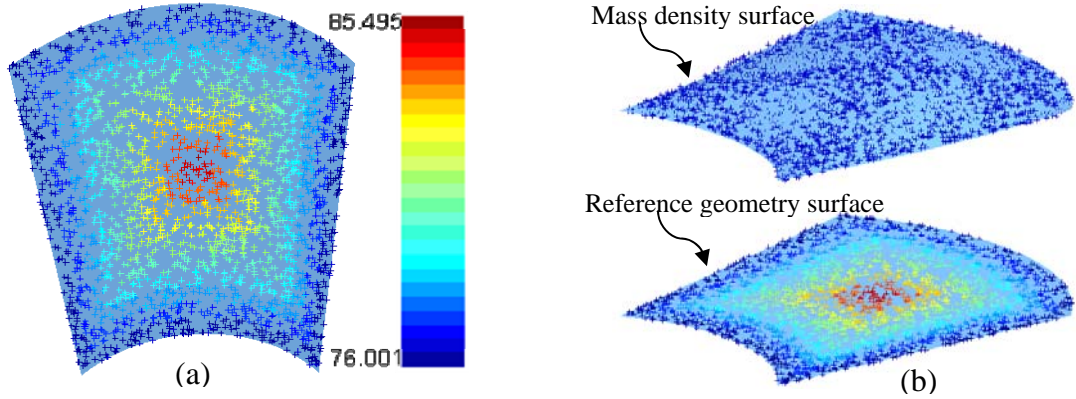


Figure 4.7: (a) A geometry surface and simulated mass density points, and (b) height display of the mass density points and fitted mass density surface

points is usually larger than that of the control points, the matrix of $\sum_{k=0}^K \mathbf{N}_{d,k} \mathbf{N}_{d,k}^T$ is normally positive definite. Therefore, the control points \mathbf{D} can be obtained by inverting the matrix. But if in some cases the matrix is not positive definite, the linear equation of (4.9) can still be solved by singular value decomposition (SVD) method [99].

Figure 4.7 (a) shows an example which consists of a geometric surface with degree of 3X3 and number of control points of 4X4 in u, v directions, respectively. In addition, 2500 randomly simulated density points are added to the geometric surface. This scattered mass density point set has the maximum density 85.495 units, minimum density of 76.001 units, average density of 79.107 units and standard deviation density of 2.365 units. As shown in the figure, the mass density points are intentionally manipulated such that density is decreasing from the central area to the lateral area. With the above illustrated method, a initial density surface can be reconstructed. Figure 4.7(b) is the height display of the mass density points and reconstructed mass density surface relatively to the geometric surface.

4.4.3.2 Multi-resolution based Mass Density Fitting

As shown in the height display of the example in Figure 4.7(b), the mass density surface does not pass through all the density points. The reason is that the number of density control points inherited from the geometric surface is not large enough to meet desired accuracy. In order to achieve higher accuracy, more control density points are needed to increase the freedom of fitting. A multi-resolution based density fitting approach is proposed to add more control points to the mass density surface. The multi-resolution based density fitting can be easily realized by refining the knot vectors of the initial fitted mass density surface.

Knot refinement means to insert multiple knots into the knot vector at once. Single knot insertion is a very important operation to B-spline surface. Given the j^{th} row density control points $d_{i,j}(i = 0..m_d)$ with degree of p_d and the knot vector

$\mathbf{U} = \{u_0, \dots, u_{m_d}\}$ and a knot $\bar{u} \in (u_k, u_{k+1})$ to be inserted, then the newly formed knot vector is $\bar{\mathbf{U}} = \{\bar{u}_0 = u_0, \dots, \bar{u}_k = u_k, \bar{u}_{k+1} = \bar{u}, \bar{u}_{k+2} = u_{k+1}, \dots, \bar{u}_{m_d+1} = u_{m_d}\}$. Denote \bar{V} and V the $L^2(\mathbb{R})$ spaces spanned by the B-spline basis functions defined by knot vector $\bar{\mathbf{U}}$ and \mathbf{U} , respectively, it is clearly that $V \subset \bar{V}$; thus the row of control density points $d_{i,j}$ have equivalent correspondences $\bar{d}_{i,j}$ ($i = 0 \dots m_d + 1$) in \bar{V} . The new row control density points $\bar{d}_{i,j}$ can be computed as [4]:

$$\bar{d}_{i,j} = \alpha_i d_{i,j} + (1 - \alpha_i) d_{i-1,j} \quad (4.10)$$

where

$$\alpha_i = \begin{cases} 1 & i \leq k - p \\ \frac{\bar{u} - u_i}{u_{i+p_d} - u_i} & k - p + 1 \leq i \leq k \\ 0 & i \geq k + 1 \end{cases} \quad (4.11)$$

In our implementation, new knots are inserted into the middle of any two adjacent and unequal knots. That is to say, a coarse knot vector space V^J is halved and subdivided into a finer space V^{J+1} . Therefore, if an initial density surface has $(m_d + p_d) \times (n_d + q_d)$ control points mesh, then the next refined control density mesh is $(2m_d + p_d) \times (2n_d + q_d)$ and the J^{th} refined control density mesh is $(2^J m_d + p_d) \times (2^J n_d + q_d)$. These nested knot vector spaces $V^0 \subset V^1 \subset \dots \subset V^J \subset \dots \subset V^\infty = L^2(\mathbb{R})$ forms a multi-resolution of the mass density surface.

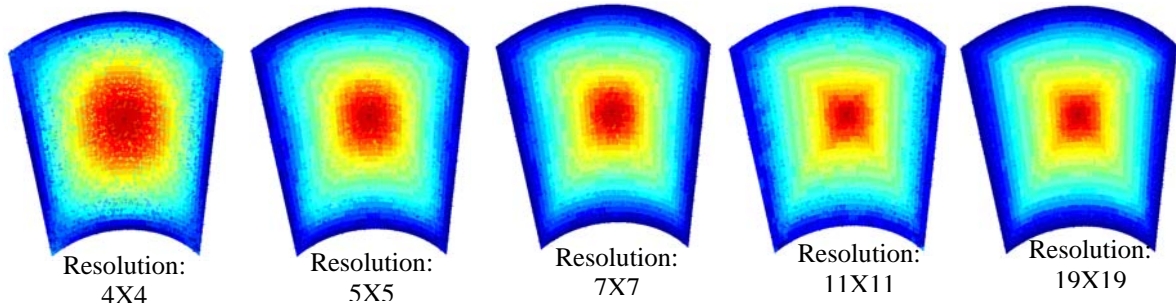


Figure 4.8: Color display of multi-resolution based mass density surfaces

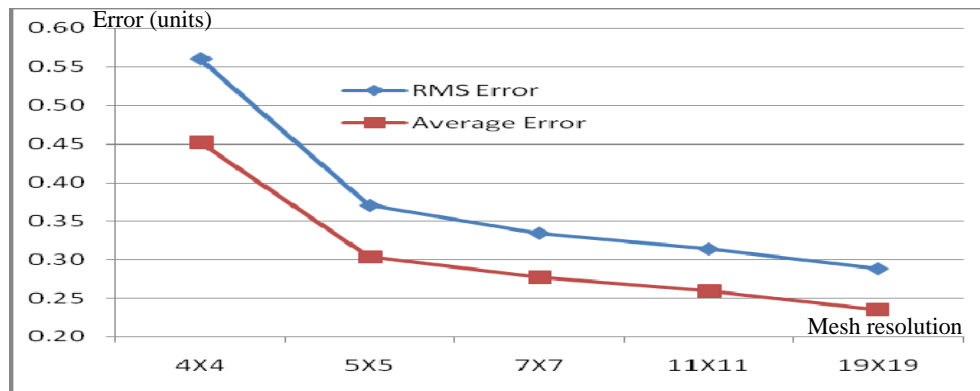


Figure 4.9: Mass density fitting error with respect to mesh resolution

Following up the example presented in Figure 4.7, the multi-resolution based density fitting approach is applied. Figure 4.8 shows the colors display of the mass density surfaces under different resolutions. As shown in the figure, the color of the mass density surface matches the color of mass density points better and better as the resolution increases. Table 4.1 lists the average and root mean square (RMS) density fitting errors for all the resolutions. Figure 4.9 shows the corresponding chart of the errors with respect to the mesh resolutions. Consistent with the color display, both of the errors are gradually decreasing with increasing resolutions.

Table 4.1: Error report of multi-resolution based density fitting

Mesh Resolution:	4X4	5X5	7X7	11X11	19X19
RMS Error (units):	0.560	0.370	0.334	0.314	0.288
Average Error (units):	0.452	0.303	0.277	0.259	0.234

4.4.3.3 Constrained Mass Density Fitting

As pointed out by Yang et al. [56], the material composition of the heterogeneous points must be positive and less than 1 in heterogeneous object design. However, in their interpolation algorithm, they did not consider the problem that even all the heterogeneous points have the material compositions positive and less than 1, the lofted curve, surface and volume might still have areas whose material compositions are negative or larger than 1 due to fitting oscillation. This is unreasonable in real practice. Figure 4.10 (a) shows a simple example with four heterogeneous points with coordinates $(0, 0, 0, 0.2)$, $(2, 0, 0, 0.5)$, $(2.7, 0, 0, 0.02)$ and $(3, 0, 0, 0.98)$ from left to right. As we can see, all the

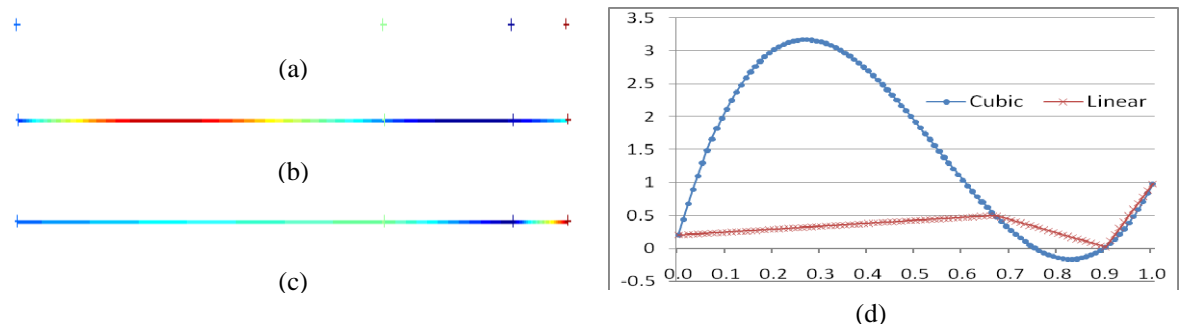


Figure 4.10: (a) Heterogeneous points, (b) interpolated cubic heterogeneous curve, (c) interpolated linear heterogeneous curve, and (d) height display of the material composition of the fitted curves

points' material compositions are within the range of 0 to 1. However, if the general heterogeneous curve lofting algorithm is applied with degree of 3, the resulted curve will have portions with material compositions larger than 1 or less than 0 as shown in Figure 4.10 (d). The color displayed heterogeneous curve in Figure 4.10(b) also shows obvious inconsistent color matching between the curve and points.

One way to solve this problem is to use B-spline curve with degree of 1 to model the material compositions because all the linearly blended curve portions between any

two adjacent points have the material composition values between that of the two points. Therefore, given the heterogeneous points have material compositions positive and less than 1, the interpolated curve will also satisfy this condition. As shown in Figure 4.10(c), the linearly interpolated heterogeneous curve has good color match with the heterogeneous points.

Linear B-spline to model heterogeneous points will limit the degree of freedom for heterogeneous object reconstruction. Moreover, for scattered heterogeneous points in 2D, the B-spline heterogeneous surface fitting (not interpolation) with degree of 1 sometimes also results in some undesired portions. An alternative way to conquer this problem is to impose boundary constraints on the reconstructed heterogeneous surface.

For a set of scattered mass density points with approximated normal distribution with mean density μ and standard deviation σ , the low and up bounds of the boundary constraints can be set as $\max(0, \mu - 3\sigma)$ and $\mu + 3\sigma$, respectively. The boundary constraints not only guarantee the reconstructed mass density surface within a reasonable density range, but also exclude some possible noisy points from the intensity images. It should be pointed out that the boundary constraints can be set to other forms depending on the distribution types of the scattered mass density points.

By incorporating the boundary constraints into equation (4.8), the mass density surface fitting then becomes a constrained optimization problem as:

$$\begin{aligned}
 \text{Minimize : } E(\mathbf{D}) &= \sum_{k=0}^K \left\| \mathbf{N}_{d,k}^T \mathbf{D} - \rho_k \right\|^2 \\
 \text{s.t. : } lb &\leq \mathbf{N}_d^T \mathbf{D} \leq ub, \quad \forall u \in [0,1] \text{ and } v \in [0,1]
 \end{aligned} \tag{4.12}$$

where lb and ub stand for the low bound and up bound, respectively. This inequality constraint requires every surface point satisfy the boundary constraints, which means there are infinite constraints because of infinite surface points. One way to simplify the boundary constraints is to use the B-spline's *strong convex hull property* which says a B-spline curve (or surface) is contained in the convex hull of its control polyline (or mesh). Therefore, the constrained optimization problem can be simplified as:

$$\begin{aligned} \text{Minimize : } E(\mathbf{D}) &= \sum_{k=0}^K \left\| \mathbf{N}_{d,k}^T \mathbf{D} - \rho_k \right\|^2 \\ \text{s.t. : } \mathbf{lb} &\leq \mathbf{D} \leq \mathbf{ub} \end{aligned} \tag{4.13}$$

where \mathbf{lb} and \mathbf{ub} denote the low bound and up bound vectors (with the same dimensions as \mathbf{D}), respectively.

As pointed out in section 4.4.3.1, the matrix $\sum_{k=0}^K \mathbf{N}_{d,k} \mathbf{N}_{d,k}^T$ is a positive semi-definite matrix, hence $E(\mathbf{D})$ is a convex function. Furthermore, because the inequality constraints are linear, the constrained optimization is a standard quadratic programming problem. In this case, the quadratic problem has a global minimum if there exists at least one vector \mathbf{D} satisfying the boundary constraints. The optimal solution $\bar{\mathbf{D}}$ must satisfy the Karush-Kuhn-Tucker (KKT) conditions and the simplex algorithm can be used to solve the linear equation system of the KKT conditions [74].

4.4.3.4 Algorithm

By comprehensively considering the issues of accuracy and constraints, the algorithm of mass density surface reconstruction based on geometric surface and scattered mass density points can be summarized as follows:

Set the desired density fitting error threshold ε_0 .

Compute the mean density μ and standard deviation σ

Parameterize the mass density points with respect to the geometric surface

Set the number of control points and knot vector of the initial density surface as the same as the geometric surface

Solve the constrained optimization problem (4.13) to obtain \mathbf{D}^0

Report the density fitting error ε

$J=0$

While($\varepsilon > \varepsilon_0$)

{

$J=J+1$

Refine the knot vectors of the previous density surface

Solve the constrained optimization problem (4.13) to obtain \mathbf{D}^J

Report the density fitting error ε

}

4.4.4 3D Heterogeneous Lofting

After a series of cross-sectional mass density surfaces have been reconstructed, the final mass density solid can be created by extending the 1D B-spline curve interpolation

algorithm [4] to 3D. Because decoupled representations are used for cross-sectional geometric and mass density surface reconstruction, the lofting of geometric solid and mass density solid are performed independently. Moreover, since all the cross-sectional geometric surfaces are derived from the same template curve, the compatibility conditions (same knot vector, same degree and same number of control points) are automatically satisfied. However, all the mass density surfaces must be refined to have the same resolutions with the highest one. In addition, the degree along the density lofting direction is chosen as 1 in cases of unreasonable regions on the density solid.

Suppose there are $l+1$ heterogeneous surfaces denoted as $(\mathbf{S}_k, \mathbf{D}_k) \in E^3 \times A^1, k = 0..l$, the decoupling representation based 3D mass density lofting algorithm can be described as follows:

Set the degree r_g and r_d in the lofting direction

Computing the knot vector \mathbf{W}_g and \mathbf{W}_d along the lofting direction based on the spacing between adjacent cross sections.

For each column (totally $(m_g + 1) \times (n_g + 1)$ columns) of the geometric control points $\mathbf{P}_{i,j}^k (k = 0..l)$, apply the B-spline curve interpolation algorithm to get control points $\mathbf{P}_{i,j,k} (i = 0..m_g, j = 0..n_g, k = 0..l)$ of the volume geometry.

For each column (totally $(m_d + 1) \times (n_d + 1)$ columns) of the density control points $d_{i,j}^k (k = 0..L)$, apply the B-spline curve interpolation algorithm to get control points $d_{i,j,k} (i = 0..m_d, j = 0..n_d, k = 0..l)$ of the volume mass density.

The volume represented by geometry control points $\mathbf{P}_{i,j,k}$ and mass density control points $d_{i,j,k}$ is the final lofted mass density solid which passes all the cross-sectional geometric and mass density surfaces.

4.5 Case Studies

The approach described in section 4.4 has been implemented in Unigraphics and tested with real examples. Because the mass density points of all examples have approximated normal distribution, the low and up bounds of the constraints for density fitting are set to $\max(0, \mu - 3\sigma)$ and $\mu + 3\sigma$, respectively. Both fitting accuracy and

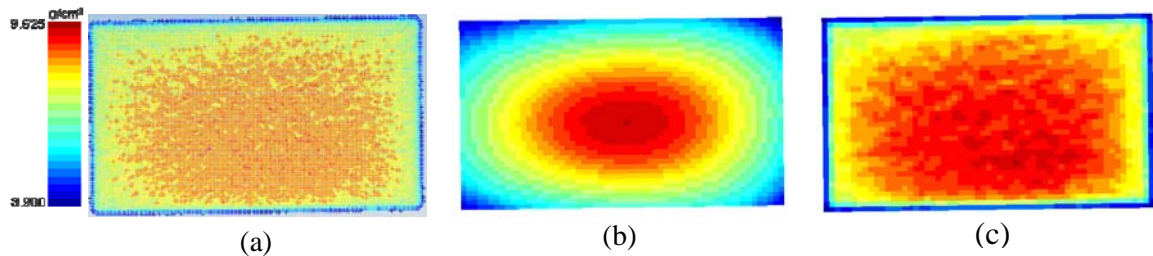


Figure 4.11: (a) Cross-sectional mass density points of a gauge block, (b) mass density surface with 4X4 resolution, and (c) mass density surface with 35x35 resolution calculation cost are given to illustrate the robustness and the applicability of the proposed approach. All the tests are performed on a DELL desktop with 3.4 GHz Intel Pentium and 2047 MB RAM.

4.5.1 Case Study 1

This example shows the constrained multi-resolution based mass density fitting for a cross-section of a gauge block. Figure 4.11 (a) shows one section of 24,796 mass density points with mean density 8.000g/cm^3 , maximum density 9.625g/cm^3 , minimum

density 3.900 g/cm^3 and standard deviation 0.811 g/cm^3 . For the constrained fitting, the low bound is set as 5.567 g/cm^3 and the up bound is set as 10.433 g/cm^3 . As the customers require the RMS error must be less than 50% of one standard deviation, the mass density fitting starts from resolution of 4X4 and ends at resolution of 35X35. As it can be seen from Table 4.2, the accuracy is satisfied from the resolution of 11X11. Figure 4.11(b) and (c) shows color display of the mass density surfaces with resolutions 4X4 and 35X35, respectively. It is obvious that Figure 4.11(c) has better color matching to the mass density points than Figure 4.11(b). Table 4.2 lists the average and RMS errors of mass density fitting under different resolutions and Figure 4.12 graphically shows the error change with respect to the resolution. As what is expected, both of the average and RMS errors are gradually decreasing as the resolution is increasing. The running time constrained density fitting for the resolution of 35x35 is about 150 seconds.

Table 4.2: Error report of multi-resolution based density fitting for the block section

Mesh Resolution:	4X4	5X5	7X7	11X11	19X19	35X35
RMS Error (g/cm^3):	0.596	0.500	0.425	0.374	0.356	0.322
Average Error (g/cm^3):	0.391	0.348	0.311	0.266	0.255	0.232

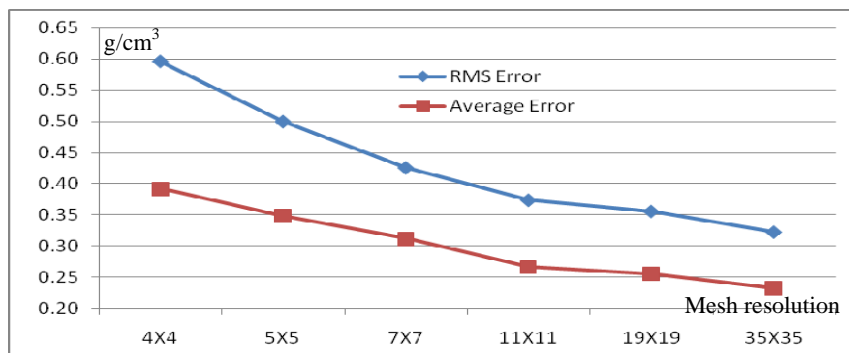


Figure 4.12: Mass density fitting error with respect to the mesh resolution for the block section

4.5.2 Case Study 2

Figure 4.13(a) shows one cross-sectional geometric surface of gauge pin which is represented by planar B-spline surface with degree of 3 and number of control points 7 in both parametric directions. In Figure 4.13(b), there are totally 21,305 mass density points with mean density 8.000g/cm^3 , maximum density 9.498g/cm^3 , minimum density 3.911g/cm^3 and standard deviation 0.814g/cm^3 . The low bound and up bound constraints are set as 5.558g/cm^3 and 10.442g/cm^3 , respectively. The multi-resolution based mass

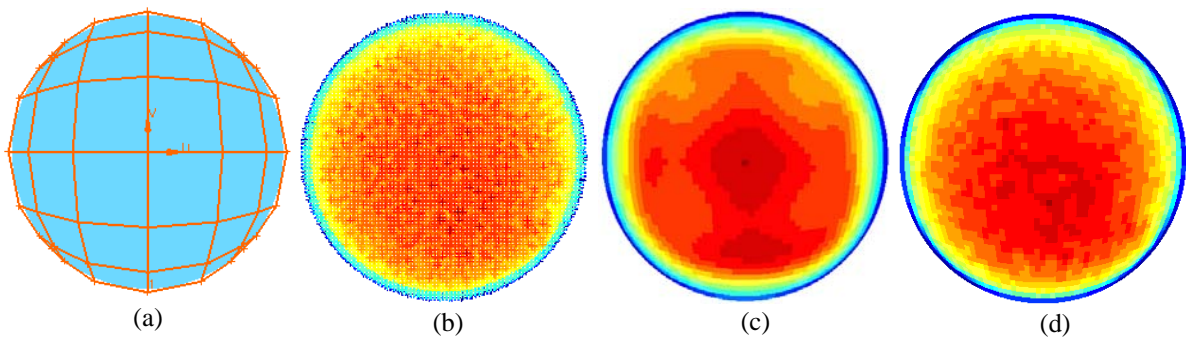


Figure 4.13: (a) A gauge pin geometry surface, (b) mass density points, (c) mass density surface with resolution of 7×7 , and (d) mass density surface with resolution of 35×35 . Density fitting algorithms is tested on this example until it reaches the resolution of 35×35 . Figures 4.13(c) and (d) are the color displays of the fitted mass density surfaces with resolution of 7×7 and 35×35 , respectively. Based on the comparison of these two figures, it is evident that Figure 4.13(d) has closer density change pattern to the mass density points. Table 4.3 lists the error report and Figure 4.14 shows the chart of the error with respect to the mesh resolution. As we can see in both of the table and chart, the average and RMS errors are gradually decreasing with increasing mesh resolution. The running time constrained density fitting for the resolution of 35×35 is about 120 seconds.

Table 4.3: Error report of multi-resolution based density fitting for the pin section

Mesh Resolution:	7X7	11X11	19X19	35X35
RMS Error (g/cm^3):	0.352542	0.328628	0.31269	0.287634
Average Error (g/cm^3):	0.253866	0.230398	0.224682	0.205086

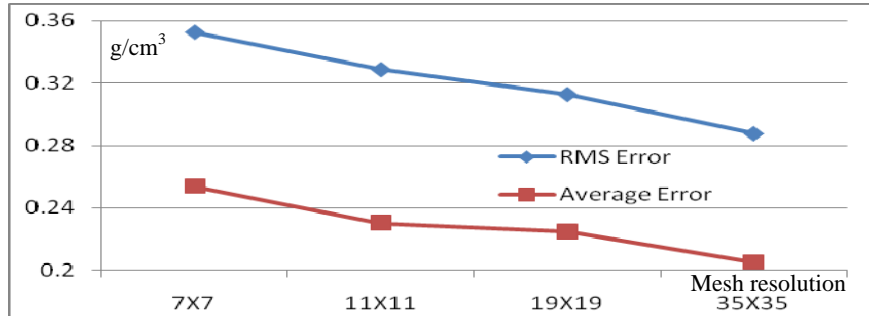


Figure 4.14: Mass density fitting error with respect to the mesh resolution for the pin section

4.5.3 Case Study 3

This example is following up the compressor blade example presented in Section 4.2. But here we focus on the mass density surfaces reconstruction based on the reconstructed geometric surfaces and mass density points. Figure 4.15(a) shows all the

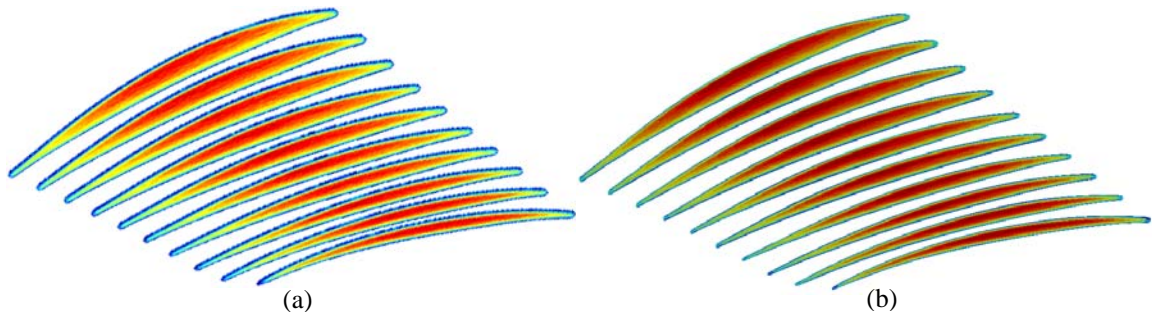


Figure 4.15: (a) Cross-sectional mass density points, and (b) reconstructed cross-sectional mass density surfaces

cross-sectional mass density points and Table 4.4 lists the statistics of the mass density points. Because the resolution (15X7) of the mass density control points inherited from

the geometric surface is larger enough to achieve desired accuracy, the constrained mass density fitting is performed only once for each section. Figure 4.15 (b) shows the reconstructed cross-sectional mass density surfaces. It can be seen that all the mass density surfaces have great color matching with the corresponding cross-sectional mass

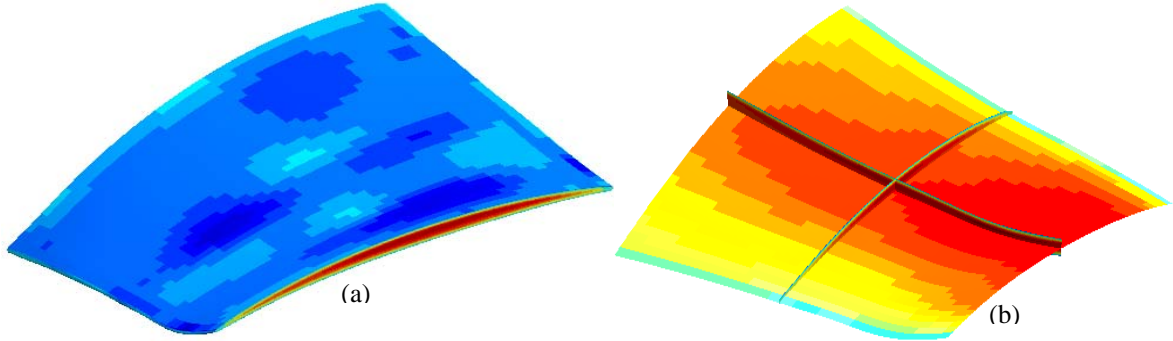


Figure 4.16: (a) Mass density solid of the compressor blade, and (b) isoparametric surfaces evaluated from the mass density solid

density points. Table 4.5 list the average and RMS errors of mass density fitting for each section. As shown in the table, the small average and RMS errors indicate good fitting to the mass density points. The running time for each section is about 60s. Based on the reconstructed mass density surfaces, the 3D heterogeneous lofting algorithm is applied and Figure 4.16(a) shows the lofted mass density solid. Figure 4.16(b) shows three isoparametric surfaces of $u = 0.5$, $v = 0.5$ and $w = 0.5$ evaluated based on the mass density solid.

Table 4.4: Statistics of cross-sectional mass density points of the compressor blade

Section number:	1	2	3	4	5	6	7	8	9	10
Point number:	3818	3971	4235	4575	4929	5356	5807	6254	6850	7242
Maximum density(g/cm ³):	10.408	10.437	10.470	10.524	10.388	10.245	10.242	10.239	10.085	9.858
Minimum density(g/cm ³):	3.950	3.933	3.911	3.839	3.781	3.723	3.674	3.616	3.552	4.005

Average density(g/cm^3):	8.000	8.000	8.000	8.000	8.000	8.000	8.000	8.000	8.000	8.000
Stadard deviation(g/cm^3):	1.857	1.841	1.852	1.815	1.792	1.758	1.746	1.694	1.652	1.404
Low bound density(g/cm^3):	2.429	2.477	2.444	2.555	2.624	2.726	2.762	2.918	3.044	3.788
Up bound density(g/cm^3):	13.571	13.523	13.556	13.445	13.376	13.274	13.238	13.082	12.956	12.212

Table 4.5: Error report of mass density fitting for the compressor blade's sections

Section number:	1	2	3	4	5	6	7	8	9	10
RMS error (g/cm^3):	0.133	0.113	0.132	0.133	0.133	0.145	0.138	0.140	0.138	0.141
Average error (g/cm^3):	0.097	0.087	0.101	0.102	0.104	0.109	0.109	0.110	0.109	0.109

4.5.4 Case Study 4

This example is a blade artifact. Figure 4.17(a) includes 8 cross-sectional geometric surface reconstructed with non-rigid registration method [98]. Each surface has the degree of 3X3 and number of control point 25X4 along the u, v parametric directions. Figure 4.17(b) shows the corresponding cross-sectional mass density points. Table 4.6

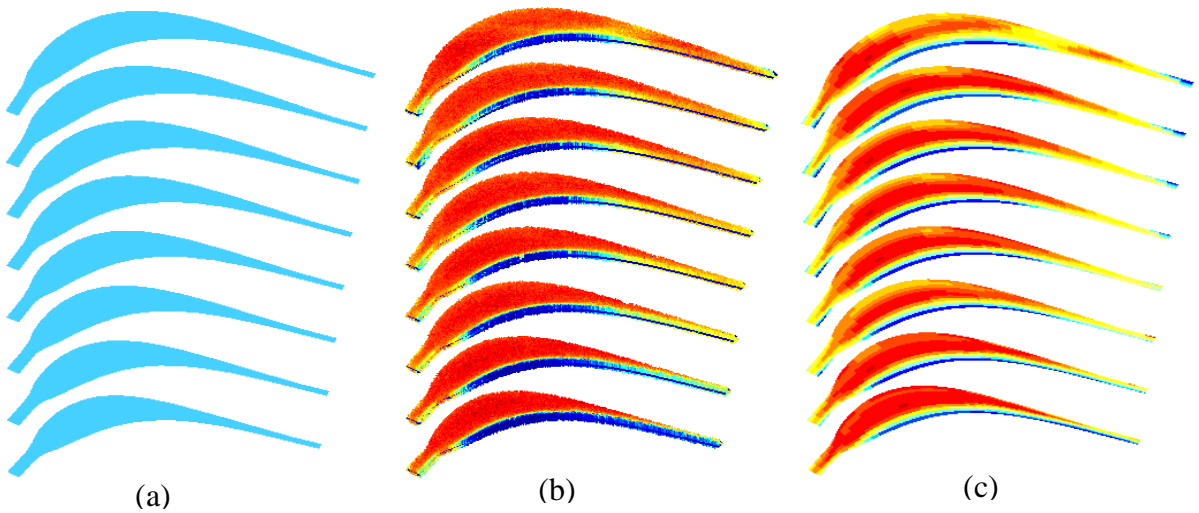


Figure 4.17: (a) Cross-sectional geometric surfaces of an artifact blade, (b) mass density points, and (c) reconstructed mass density surfaces

lists the statistics of the mass density points of each section. As shown in the table, the mass density points are quite noisy because of the high standard deviation and lower minimum densities. By applying the constrained density fitting to each section with the number of density control points the same as that of the geometric surface, a series of density surfaces are reconstructed as shown in Figure 4.17(c). It can be observed that the color display of each density surface matches its corresponding density point very well. In addition, as shown in the error report in Table 4.7, most of the RMS errors are satisfied except section 5, 6, and 7 whose RMS error are just slightly larger than one half of the standard deviation. This is normal for such noisy mass density points and the error can be further reduced by increasing the resolutions of the mass density surface. The running time for each section in this example is about 90 seconds. Figure 4.18(a) shows the mass density solid reconstructed by using the 3D heterogeneous lofting algorithm and Figure 4.18(b) shows the isoparametric surfaces of $u = 0.5$, $v = 0.5$ and $w = 0.5$ evaluated based on the mass density solid.

Table 4.6: Statistics of the cross-sectional mass density points of the artifact blade

Section number:	1	2	3	4	5	6	7	8
Point number:	11343	11860	12443	13026	13605	14264	14917	15530
Maximum density(g/cm ³):	9.879	9.583	9.512	9.332	9.294	9.182	9.326	9.493
Minimum density(g/cm ³):	0.323	0.308	0.338	0.490	0.720	0.849	0.794	0.419
Average density(g/cm ³):	8.000	8.000	8.000	8.000	8.000	8.000	8.000	8.000
Standard deviation(g/cm ³):	2.390	1.943	1.653	1.382	1.227	1.163	1.140	1.242
Low bound density(g/cm ³):	0.83	2.171	3.041	3.854	4.319	4.511	4.58	4.274
Up bound density(g/cm ³):	15.17	13.829	12.959	12.146	11.681	11.489	11.42	11.726

Table 4.7: Error report of mass density fitting for the artifact blade's sections

Section number:	1	2	3	4	5	6	7	8
RMS error (g/cm ³):	0.828	0.796	0.742	0.667	0.626	0.600	0.598	0.618
Average error (g/cm ³):	0.534	0.474	0.413	0.346	0.316	0.301	0.300	0.338

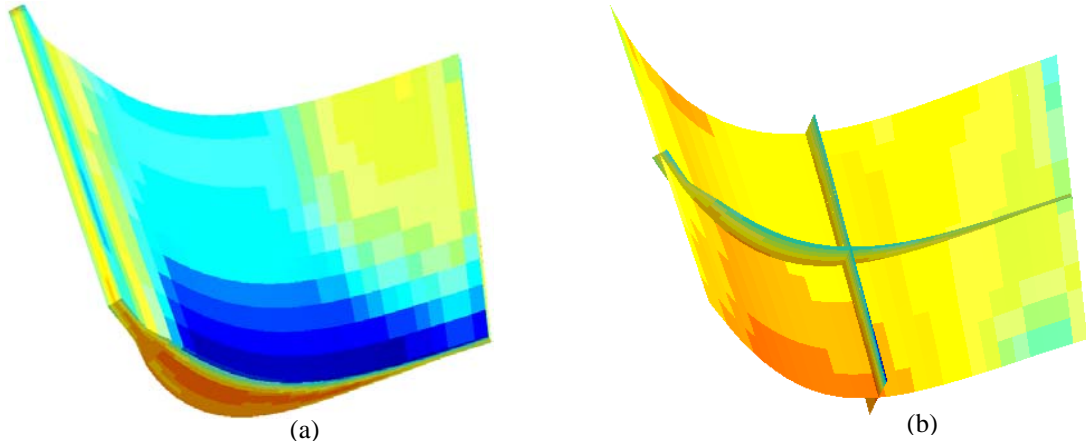


Figure 4.18: (a) Mass density solid of the artifact blade, and (b) isoparametric surfaces evaluated from the mass density solid

4.6 Conclusions and Future Work

By taking mass density as one of the physical attributes of "Product DNA", this research proposes a constraint based multi-resolution approach to reconstruct a heterogeneous model based on cross-sectional mass density points. In this approach, a series of cross-sectional geometric surfaces are firstly reconstructed by transforming and deforming a template curve to best fit the boundary points extracted from the intensity images of ICT. Based on the cross-sectional mass density points, a decoupled representation is used for mass density surface fitting in order to increase modeling flexibility. Inheriting the number of control points and knot vectors from the

reconstructed geometric surface, an initial mass density surface is reconstructed by minimizing the sum squared distances between the surface and points. In order to obtain a mass density surface within a reasonable density range, boundary constraints are added into density fitting. Further knot refinement technology can be applied on the initial mass density surface to increase fitting resolutions and thus achieve desired accuracy. Finally, a mass density solid is lofted based on the reconstructed mass density surfaces with 3D heterogeneous lofting algorithm.

There are three basic advantages of the proposed approach. First, the decoupled representations enable independent modeling flexibilities for geometry and mass density and thus save huge storage space under different resolution requirements. Second, the boundary constraints guarantees a reasonable mass density surface reconstructed based on the mass density points. Third, the multi-resolution based method provides a coarse-to-fine fitting hierarchy to achieve desired accuracy. The simulated and real examples have demonstrated the effectiveness and superiority of the proposed approach.

Future research of heterogeneous object modeling can be extended into incorporating more types of physical attributes into the as-manufactured CAD model based "Product DNA" for different applications. In addition, performance analysis and prediction can be conducted based on the reconstructed as-manufactured CAD model can also be investigated.

CHAPTER 5

CONCLUSIONS AND FUTURE WORK

5.1 Conclusions

This doctoral research is focusing on reconstructing an as-manufactured CAD model based on measurement data, which is an essential stage for the development of "Product DNA" framework. Specifically, the research work has been conducted from three different perspectives to encode the product information into the as-manufactured CAD model: dimensional geometry, surface texture and physical attribute (mass density).

First, a non-rigid registration approach has been proposed for 2D profile curves based geometry modeling for the purpose of geometry information. In this approach, a weighted mutual distance based method is proposed to establish the correspondence and then the template curve is iteratively transformed and morphed to best fit the measured points through affine combined with FFD transformation while maintaining geometry constraints. The final solid model can then be created by lofting, sweeping, translating or revolving with the morphed 2D profile curves. Compared to the traditional constrained fitting method that assumes the 2D profile points have been segmented in advance and the initial fitted curves are very close to the points, this non-rigid registration approach does not require any data preprocessing such as noise filtering, sorting, segmentation and parameterization. Moreover, the compatibility conditions between different profile curves

are automatically satisfied to ensure the final reconstructed solid with high quality. The real industry examples have demonstrated the effectiveness and significance of the approach applied in part family modeling and manufactured part validation.

Second, a B-spline wavelet-based MRA approach has been proposed for surface texture modeling, analysis and process parameters correlation in end-milling. Motivated by multi-resolution curves in computer graphics, an initial B-spline surface is first interpolated or fitted to the measured points of the surface texture. With B-spline wavelet transform, the initial surface is then decomposed into higher-frequency details and lower-frequency approximations. By taking the reconstructed surface roughness, waviness and form based on different frequency regimes as the responses, regression models are built by considering feed rate, spindle speed, axial depth of cut and tool wears as controllable variables in the end-milling process of aluminum. The real case studies and comparisons with ISO Gaussian filter have demonstrated the effectiveness of the proposed B-spline wavelet-based MRA algorithm for surface texture analysis and manufacturing process diagnostics.

Third, by taking mass density as an example of physical attribute, a systematic approach has been proposed to reconstruct a heterogeneous model based on measured cross-sectional intensity images. To increase modeling flexibility and save storage space, decoupled B-spline based representations are adopted to model geometry and mass density independently. Moreover, a constraint based multi-resolution method is proposed for mass density surface fitting in order to achieve reasonable mass density range and satisfied accuracy. Finally, a 3D heterogeneous mass solid is created by lofting all the reconstructed mass density surfaces with 3D heterogeneous lofting algorithm. The

simulated and real examples have demonstrated the effectiveness and success of the proposed approach for reconstruction of heterogeneous objects. In addition, the proposed approach can also be used for heterogeneous object modeling for other physical attributes such as porosity and material composition.

5.2 Future Work

The research work of this doctoral study is concentrated on the coding process of "Product DNA", which is the first step to develop the entire framework of the concept. In this dissertation, three different DNA genomes, i.e., geometry dimensions, surface texture and physical attributes (mass density), have been considered to reconstruct an as-manufactured CAD model based on measurement data. As indicated in Figure 1.1, the coding process of building an as-manufactured CAD model is an essential part of the entire "Product DNA" framework. In order to complete the whole "Product DNA" framework for different purposes of applications, a number of future research may be taken up following the studies in this dissertation.

1. Establishment of Product DNA library. Inspired by the idea of human gene library, a Product DNA library can be built based on the classification of manufacturing parts. The genome priority of classification is geometry, surface texture and physical attributes. By comparing geometry genomes, the products with similar geometry genomes will be grouped into a part family. For example, the blades at different stages in jet engine belong to the same part family because they share the similar geometry genome, although the dimensions, surface texture and physical attributes might be different. Surface texture pattern and physical attributes distribution can be further

divided based on the family parts into more detailed categories. In addition, the information of manufacturing process, functional performance and product life time can be attached to each Product DNA.

SQL database can be used to build the Product DNA library. New Product DNA can be easily added to the library according to classification rules. A search engine can also be developed for the Product DNA library. The search engine will enable the users to quickly find their interested products by inputting some key words such as genomes of geometry, dimensions, surface textures or physical attributes. The initial product based on the Product DNA concept could be a data management and reporting system that will be designed to analyze Product DNA to determine the capacity and predict the life expectancy for a product based on the predetermined function the product is built to perform.

2. Product DNA based quality inspection. Each product in the library has a corresponding Product DNA of the nominal design. Influenced by various manufacturing factors, the manufactured part usually differs from the nominal design to some extent. Therefore, an important application of Product DNA is to inspect the product quality by comparing the corresponding genome of the manufactured part with that of the nominal design. On the other hand, by continuously monitoring the Product DNA of manufactured parts throughout the whole life cycle, people can find the quality issue at the right time and make decisions of repairing or replacement.

3. Product DNA based process diagnosis. The Product DNA can be used to identify the causes of genomes variation and relationship to the manufacturing processes.

With knowledge of these causes and relationships, higher precision manufacturing will be possible. By examining the relationship between the genomes variation and the manufacturing process, the root causes or factors which result in the variation can be identified. The preliminary research in chapter 3 has demonstrated this idea by correlating surface texture genomes to the milling process.

In this research, a set of tools can be developed with experience-based knowledge and its unified consideration of the analytical knowledge and connections. The Stream of Variations approach can be utilized to connect dimensional and surface texture genomes of the product with fixture or tool alignment errors in the process. In addition, statistical methods can be used to describe connections of product DNA with the process-level faults and behavioral patterns of the product during its use. It is anticipated that a number of physical attribute genomes will be extracted from the product measurements for which no experience-based knowledge about connections to the process-level faults or product behavior patterns will be available.

4. Product DNA based performance analysis and prediction. The Product DNA not only uniquely defines the product's characteristics, but also defines the functional performance of the product in the field of use. In this research, the relationship between DNA genomes and physical performance can be investigated. Furthermore, DNA decoding tools can be developed for the purpose of performance analysis and prediction.

Case study can be carried out depending on different applications. For example, the geometry dimensional genome of the blades is fundamentally related to the aerodynamics performance [8]. By incorporating engineering rules into the geometry

genomes, the relationship between the performance and geometry parameters can be better understood. Surface texture genome has significant impact on the performance of functional surfaces such as mating and sealing surfaces in powertrain manufacturing. Wavelet based multi-resolution analysis (MRA) method can be used to identify the dominated frequency regimes which have the most significant influence on the performance. Physical attributes normally have more direct relationships to the physical performance. The density genomes, especially for the casting, forging and laser consolidation part, can also be studied to explore the relationships to performance such as natural frequency and dynamic strain and stress. Simulation models can be developed by decoding the physical attributes genome.

By constantly monitoring the Product DNA and analyzing the physical performance, time series model can be built to examine the evolution behaviors of the genomes and how they dynamically affect the physical performance over time. Statistical methods can be developed based on the time series model for the purpose of performance prediction.

5. Optimization of design, manufacturing and performance. The ultimate goal of Product DNA development is to provide a platform for optimal product design and manufacturing to achieve desired performance. Product DNA serves as the information hub which closes the loop of design, manufacturing, inspection and engineering analysis (See Figure 5.1).

Design optimization tools can be developed by modifying corresponding DNA genomes based on the relationships between Product DNA and physical performance. To

do this, the performance will be set as the objective function with DNA genomes as the variables while subject to some engineering constraints. Optimal Product DNA can be obtained by solving a constrained optimization problem.

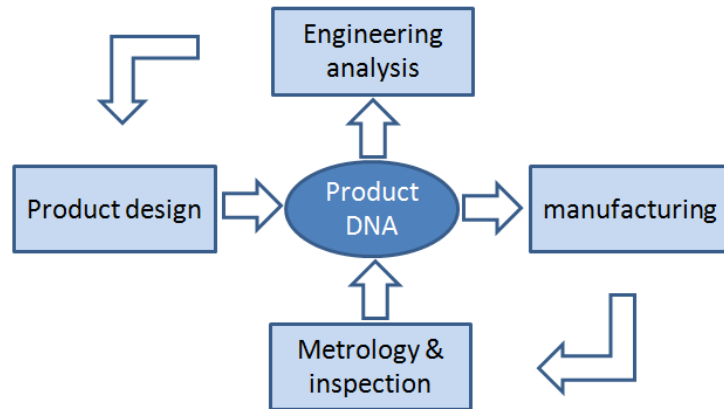


Figure 5.1: Product DNA based closed-loop design, manufacturing, inspection and analysis

There is a lack of understanding about exactly how manufacturing processes directly and indirectly affect the desired physical attributes and performance of the parts they produce. Product DNA can be considered a linkage between the process and performance because it carries genomes related both to process information and performance patterns of the product. Once we have constructed a cost model of process and an improved understanding of how manufacturing process parameters affect part characteristics, methods can be developed to choose parameter settings which allow users to both achieve desired physical performance and minimize manufacturing cost. To do this, the quality of the desired physical attribute genomes can be expressed in terms of manufacturing cost, formulated with a constrained objective function, and developed by a technique to evaluate the optimal value of the process parameters.

5.3 Original Contributions

This research tackled the coding process of reconstructing an as-manufactured CAD model under the framework of "Product DNA". The main original contributions of this dissertation are summarized as follows:

1. For the dimensional geometry genome, the non-rigid registration approach for 2D profile curves based geometry modeling is novel. Most of the state-of-the-art approaches require the 2D profile points sorted, segmented and parameterized. With the non-rigid registration approach, a template curve can be automatically transformed and morphed to best fit the 2D profile points without any data preprocessing work. Moreover, all the reconstructed 2D profile curves naturally satisfy the compatibility condition, which is essential to obtain a high quality solid model by sweeping, lofting, revolving or translating.

2. For the surface texture genome, the B-spline wavelet-based MRA algorithm for surface texture modeling and analysis is novel. Because the B-spline wavelet has linear phase transmission characteristics, the filtered surface texture does not have any distortions. Most of the current studies are still using a single frequency band to characterize the surface texture. With the B-spline wavelet-based MRA method, the surface texture can be decomposed into multiple finer frequency bands such as surface form, surface waviness and surface roughness. By correlating different frequency bands of the surface texture to manufacturing parameters and conditions, process faults and root causes can be more precisely diagnosed.

3. In addition to dimensional geometry and surface texture, physical attributes are incorporated into the "Product DNA" framework. By taking mass density as an example of physical attribute, a systematic approach to reconstruct a heterogeneous solid based on cross-sectional mass density points is new. Although there are numerous studies in the field of heterogeneous modeling, all of them are conducted in a forward design way by converting a concept into a computer model. On the contrary, the proposed approach enables to build a heterogeneous model based on the inspection data of a manufactured part. The as-manufactured mass density solid has important applications such as quality inspection and engineering analysis. In addition, the algorithm of constrained mass density surface fitting with decoupled multi-resolution representation is novel.

APPENDICES

Appendix A: Transformations in 2D space

Transformation is a function f which maps a point $\mathbf{X}_i = [x_{i1} \ x_{i2} \ 1]^T$ in the source data to the corresponding point $\mathbf{Y}_j = [y_{j1} \ y_{j2} \ 1]^T$ in the target data, i.e.,

$$f : \mathbf{X}_i \rightarrow \mathbf{Y}_j. \quad (\text{A.1})$$

Rigid Transformation

Rigid transformation in 2D allows the source data rigidly to move to the target data with 3 DOFs (degree of freedom), i.e., one rotation and two translations. The mathematical form of rigid transformation with homogeneous coordinates is:

$$f(\mathbf{X}_i) = \begin{bmatrix} \cos \theta & \sin \theta & t_1 \\ -\sin \theta & \cos \theta & t_2 \\ 0 & 0 & 1 \end{bmatrix} \begin{bmatrix} x_{i1} \\ x_{i2} \\ 1 \end{bmatrix}. \quad (\text{A.2})$$

Affine Transformation

Different from rigid transformation, affine transformation in 2D allows the source data to deform with three additional DOFs (one shear and two scales). Therefore,

$$f(\mathbf{X}_i) = \begin{bmatrix} a_1 & a_2 & a_3 \\ a_4 & a_5 & a_6 \\ 0 & 0 & 1 \end{bmatrix} \begin{bmatrix} x_{i1} \\ x_{i2} \\ 1 \end{bmatrix} \triangleq \mathbf{TX}_i. \quad (\text{A.3})$$

Free-from Deformation

The basic idea of FFD is to deform the object by manipulating the control points of a designed mesh [101]. There are many proposed methods [102] for mesh design and the simplest way is to define the mesh shape as the axis oriented bounding box of the object with a grid of control points \mathbf{V} . Because the objects considered in this paper are 2D curves, the designed mesh, sometimes called lattice, is often expressed as a tensor product B-spline surface:

$$\mathbf{S}(u, v) = \sum_{i', j'=0}^{M, N} B_{i', j'}(u, v) \mathbf{V}_{i', j'} \triangleq \mathbf{B}^T \mathbf{V} \quad (\text{A.4})$$

where $\mathbf{B} = [B_{0,0}(u, v) \ \cdots \ B_{M,N}(u, v)]^T$ and $B_{i,j}(u, v) = B_{i,p}(u)B_{j,q}(v)$; $B_{i,p}(u), B_{j,q}(v)$ are the p^{th} , q^{th} order B-spline basis functions with the knot vectors $\mathbf{u} = [u_0 \ \cdots \ u_p \ \cdots \ u_M \ \cdots \ u_{M+p}]$ and $\mathbf{v} = [v_0 \ \cdots \ v_q \ \cdots \ v_N \ \cdots \ v_{N+q}]$, respectively. $\mathbf{V} = [\mathbf{V}_{0,0} \ \cdots \ \mathbf{V}_{M,N}]^T$ are the lattice control points.

A point \mathbf{P}_k embedded in the lattice with parameters (u_k, v_k) can be computed as:

$$\mathbf{P}_k = \mathbf{S}(u_k, v_k) = \sum_{i', j'=0}^{M, N} B_{i', j'}(u_k, v_k) \mathbf{V}_{i', j'} \triangleq \mathbf{B}_{\mathbf{P}_k}^T \mathbf{V} \quad (\text{A.5})$$

Hence, if a displacement vector $\boldsymbol{\delta}$ is made on the control points of the lattice, then the transformation of the point \mathbf{P}_k can be expressed as:

$$f(\mathbf{P}_k) = \sum_{i', j'=0}^{M, N} B_{i', j'}(u_k, v_k) (\mathbf{V}_{i', j'} + \boldsymbol{\delta}_{i', j'}) = \mathbf{P}_k + \mathbf{B}_{\mathbf{P}_k}^T \boldsymbol{\delta} \quad (\text{A.6})$$

where $\boldsymbol{\delta} = [\boldsymbol{\delta}_{0,0} \ \cdots \ \boldsymbol{\delta}_{M,N}]^T$.

REFERENCES

- [1] M. Zhang, 2007, Measurement scheme and classification methods for the development of a "Product DNA" concept in manufacturing, Ph.D. thesis, University of Michigan
- [2] http://www.coherix.com/shapix_surface_detective, 2009
- [3] G. Farin, 2002, Curves and Surfaces for CAGD, 5th edition, Morgan-Kaufmann
- [4] L. Piegl and W. Tiller, 1997, The NURBS Book, 2nd edition, Springer-Verlag, New York, NY
- [5] T. Varady, R. Martin and J. Cox, 1997, Reverse engineering of geometric models, Computer-Aided Design, 29(4), pp. 253-254
- [6] N. Werghi, R. Fisher, C. Robertson and A. Ashbrook, Object reconstruction by incorporating geometric constraints in reverse engineering, Computer-Aided Design, 1999, 31(6), pp. 363-399
- [7] Pál Benko, Géza Kós, Tamás Várady, László Andor, Ralph Martin. 2002, Constrained fitting in reverse engineering, Computer-Aided Geometric Design, 19(3), pp. 173-205
- [8] Y. Li, X. Huang, C. Gong, K. Wang, 2004, An engineering rules based parameterization approach for turbine blade reverse engineering, Proceedings of the Geometric Modeling and Processing, pp. 311-318.
- [9] Y. Li, X. Huang, C. Gong, J. Zheng, 2005, Sketch template based parametric modeling in reverse engineering, Computer-Aided Design & Applications, 2(1-4), pp. 19-28.
- [10] P. J. Besl, N. D. McKay, 1992, A method for registration of 3-D shapes, IEEE Transactions on Pattern Analysis and Machine Intelligence, 14(2), pp. 239-256
- [11] Y. Chen, G. Medioni, 1991, Object modeling by registration of multiple range images, Image and Vision Computing, 10, pp. 145-155
- [12] D. Rueckert, L.I. Sonoda, C. Hayes, D. L. G. Hill, M.O. Leach, D. J. Hawkes, 1999 Non-rigid registration using free-form deformations: application to breast MR images, IEEE Transactions on Medical Imaging, 18(8), pp. 712-721
- [13] ASME B46.1., 1995, Surface texture (Surface Roughness, Waviness, and Lay).
- [14] G.T. Smith, 1989, Advanced machining, Springer-Verlag, New York, NY. pp. 198-223
- [15] D J Whitehouse, 1997, Surface metrology, Measurement Science and Technology, 8, pp. 955-977
- [16] C. Yuan, Z. Peng, X. Yan, 2005, Surface characterization using wavelet theory and confocal laser scanning microscopy, Journal of Tribology, 127, pp. 394-404
- [17] http://www.novacam.com/nc_profilometer.php

- [18] <http://www.veeco.com/promo/nt9000/>
- [19] J. M. Bennett, 1992, Recent developments in surface roughness characterization, *Measurement Science and Technology*, 3, pp. 1119-1127
- [20] D.J. Whitehouse, 1982, The parameter rash – is there a cure? *Wear*, 83, pp. 75-78.
- [21] ISO 4287:1997, Geometrical product specifications(GPS) - Surface texture: Profile method- Terms, definitions and surface texture parameters
- [22] T. R. Thomas, 1992, *Rough surface*, 2nd edition, London : Imperial College Press.
- [23] W.P. Dong, P.J. Sullivan, K.J. Stout, 1992, Comprehensive study of parameters for characterising three-dimensional surface topography I: Some inherent properties of parameter variation, *Wear*, 159, pp. 161-171.
- [24] W.P. Dong, P.J. Sullivan, K.J. Stout, 1993, Comprehensive study of parameters for characterising three-dimensional surface topography II: Statistical properties of parameter variation, *Wear*, 178, pp. 29-43.
- [25] W.P. Dong, P.J. Sullivan, K.J. Stout, 1994, Comprehensive study of parameters for characterising three-dimensional surface topography III: Parameters for characterising amplitude and some functional properties, *Wear*, 178, pp. 29-43.
- [26] W.P. Dong, P.J. Sullivan, K.J. Stout, 1994, Comprehensive study of parameters for characterising three-dimensional surface topography IV: Parameters for characterising spatial and hybrid properties, *Wear*, 178, pp. 45-60.
- [27] M. Vetterli, 1992, Wavelets and filter banks: theory and design, *IEEE Transactions on Signal Processing*, 40(9), pp. 2207-2232.
- [28] G. Strang, T. Q. Nguyen, 1996, *Wavelets and filter banks*, Wellesley Cambridge Press, Wellesley.
- [29] J. Raja, B. Muralikrishnan, S. Fu, 2002, Recent advances in separation of roughness, waviness and form, *Journal of the International Societies for Precision Engineering and Nanotechnology*, 26, pp. 222-235.
- [30] M. Stephane, 1999, *A wavelet tour of signal processing*, Second edition, Academic Press
- [31] S. Fu, B. Muralikrishnan, J. Raja, 2003, Engineering surface analysis with different wavelet bases, *Journal of Manufacturing Science and Engineering*, 125, pp. 844-852.
- [32] V. Niola, G. Nasti, G. Quaremba, 2005, A problem of emphasizing features of a surface roughness by means the discrete wavelet transform, *Journal of Material Processing Technology*, 164-165, pp. 1410-1415.
- [33] X. Chen, J. Raja, S. Simanapalli, 1995, Multi-scale analysis of engineering surfaces, *International Journal of Machine Tools and Manufacture*, 35, pp. 231-238.
- [34] X.Q. Jiang, L. Blunt, K.J. Stout, 2000, Development of a lifting wavelet representation for surface characterization, *Proc. R. Soc. Lond. A*, 456, pp. 2283-2313.

- [35] B. Josso, D. R. Burton, M. J. Lalor, 2002, Frequency normalised wavelet transform for surface roughness analysis and characterisation, *Wear*, 252, pp. 491-500.
- [36] C. Yuan, Z. Peng, X. Yan, 2005, Surface characterization using wavelet theory and confocal laser scanning microscopy, *Journal of Tribology*, 127, pp. 394-404.
- [37] C. K. Chui, 1992, *An introduction to wavelets*, Elsevier.
- [38] A. Finkelstein, D. H. Salesin, 1994, Multiresolution curves, *Computer Graphics (proceedings of SIGGRAPH'94)*, 28, pp. 261-268.
- [39] N.T. Ninh and M.A. Wahab, 1995, The effect of residual stress and weld geometry on the improvement of fatigue life, *Journal of materials processing technology*, 48(1-4), pp.581-588
- [40] X.Y. Kou, and S.T. Tan, 2007, Heterogeneous object modeling: A review. *Computer-Aided Design*, 39(4), pp.284-301
- [41] E. Lorensen, E. Cline, 1987, *Marching cubes: A high resolution 3D surface construction algorithm*. ACM Press
- [42] V. Chandru, S. Manohar, C.E. Prakash, 1995, Voxel-based modeling for layered manufacturing. *Computer Graphics and Applications*, 15(6), pp. 15-42.
- [43] M. Chen, J.V. Tucker, 2000, Constructive volume geometry, *Computer Graphics Forum*, 19, pp. 281-93.
- [44] T.R. Jackson, 2000, *Analysis of functionally graded material object representation methods*. Ph.D. thesis. Massachusetts Institute of Technology
- [45] V. Kumar, D. Dutta, 1998, *Approach to modeling & representation of heterogeneous objects*. *Journal of Mechanical Design, Transactions of the ASME*, 120, pp. 659–67
- [46] A. Biswas, V. Shapiro, I. Tsukanov, 2004, Heterogeneous material modeling with distance fields, *Computer Aided Geometric Design*, 21, pp. 215–42.
- [47] F. Zhu, 2004, *Visualized CAD modeling and layered manufacturing modeling for components made of a multiphase perfect material*. M.Phil. thesis. The University of Hong Kong
- [48] Y.K. Siu, S.T. Tan, 2002, Source-based heterogeneous solid modeling. *Computer-Aided Design*, 34(1), pp. 34-41.
- [49] X.Y. Kou, and S.T. Tan, 2005, A hierarchical representation for heterogeneous object modeling, *Computer-Aided Design*, 37(3), pp. 307-319.
- [50] A. Pasko, V. Adzhiev, B. Schmitt, and C. Schlick, 2001, Constructive hypervolume modeling, *Graph Models*, 63, pp.413–42.
- [51] J.R. Cho, S.W. Shin, 2004, Material composition optimization for heat-resisting FGMs by artificial neural network. *Composites Part A: Applied Science and Manufacturing*, 35, pp. 585–94.

- [52] J. Hua, Y. He, H. Qin, 2004, Multiresolution heterogeneous solid modeling and visualization using trivariate simplex splines. In: Proceedings of the ninth ACM symposium on solid modeling and applications, pp. 47-58
- [53] J. Huang, G.M. Fadel, V.Y. Blouin and M. Grujicic, 2002, Bi-objective optimization design of functionally gradient materials. *Materials & Design*, 23, pp. 657–66.
- [54] X. Qian and D. Dutta, 2003, Physics-based modeling for heterogeneous objects. *ASME Transactions: Journal of Mechanical Design*, 125, pp. 416–27
- [55] Z. Wu, H.S. Seah and F. Lin, 1999, NURBS-based volume modeling, *International Workshop on Volume Graphics*, pp. 321–30
- [56] P. Yang and X. Qian, 2007, A B-spline-based approach to heterogeneous objects design and analysis, *Computer-Aided Design*, 39, pp. 95-111
- [57] W. Martin and E. Cohen, 2001, Representation and extraction of volumetric attributes using trivariate splines: A mathematical framework, *Proceedings of the Sixth ACM Symposium on Solid Modeling and Applications*, pp. 234–40
- [58] V. Pratt, 1987, Direct least-squares fitting of algebraic surfaces, *Computer Graphics*, 21(4), pp.145–152
- [59] H. Pottmann and T. Randrup, 1998, Rotational and helical surface approximation for reverse engineering, *Computing*, 60(4), pp. 307–322
- [60] D. Marshall, G. Lukacs and R. R. Martin, 2001, Robust Segmentation of primitives from range data in the presence of geometric degeneracy, *IEEE PAMI*, 23(5), pp.304–314
- [61] W. Ma, and J. Kruth, 1995, Parameterization of randomly measured points for least squares fitting of B-spline curves and surfaces, *Computer-Aided Design*, 27(9), pp. 663–75
- [62] V. Weiss, and L. Andor, G. Renner, and T. Varady, 2002, Advanced surface fitting techniques, *Computer-Aided Design*, 19(1), pp.19–42
- [63] P. Benko, R.R. Martin, and T. Varady, 2001, Algorithms for reverse engineering boundary representation models, *Computer-Aided Design*, 33(11), pp.839–851
- [64] Y. Ke, W. Zhu, F. Liu and X. Shi, 2006, Constrained fitting for 2D profile-based reverse modeling, *Computer-Aided Design*, 38(2), pp.101-114
- [65] L. Piegl, and W. Tiller, 1996, Algorithm for approximate NURBS skinning, *Computer-Aided Design*, 28(9), pp. 699-706
- [66] H. Chui, and A. Rangarajan, 2003, A new point matching algorithm for non-rigid registration, *Computer Vision and Image Understanding*, 89(2-3), pp.114-141
- [67] K. H. Bae and D. D. Lichti, 2004, Automated registration of unorganised point clouds from terrestrial laser scanners, *IAPRS*, Vol. XXXV, part B5, pp.222-227
- [68] A.E. Johnson and M. Hebert, 1997, Surface registration by matching oriented points, *Proceedings of the International Conference on Recent Advances in 3-D Digital Imaging and Modeling*, pp.121-128

- [69] P. Kagan, A. Fischer and P. Z. Bar-Yoseph, 2003, Mechanically based models: adaptive refinement for B-spline finite element, *Int. J. Numer. Meth. Eng*, 57(68), pp.1145-1175
- [70] S. Schein and G. Elber, 2004, Discontinuous Free Form Deformations, *Proceedings of the Computer Graphics and Applications, 12th Pacific Conference*, pp.227-236
- [71] G. Sela, J. Subag, A. Lindblad, D. Albocher, S. Schein and G. Elber, 2007, Real-time haptic incision simulation using FEM-based discontinuous free-form deformation, *Computer-Aided Design*, 39(8), pp.685–693
- [72] G. Celnikera and D. Gossardb, 1991, Deformable curve and surface finite-elements for free-form shape design, *Computer Graphics*, 25(4), pp.257-266
- [73] J. E. Dennis and R. B. Schnabel, 1996, Numerical methods for unconstrained optimization and nonlinear equations, *Classics in Applied Mathematics 16*, Soc for Industrial & Applied Math
- [74] R. Fletcher, 1987, *Practical methods of optimization*, J. Wiley and Sons, Chicester and New York, second edition
- [75] J. Raja, and V. Radhakrishnan, 1979, Digital filtering of surface profiles, *Wear*, 57, 147-155
- [76] D.M. Tsai and S.K. Wu, 2000, Automated surface inspection using Gabor filters, *International Journal of Advanced Manufacturing Technology*, 16, 474-482
- [77] D. Montgomery and Y. Altinatas, 1991, Mechanism of cutting forces and surface generation in dynamic milling, *ASME Journal of Engineering for Industry*, 113, 160-168
- [78] M. Alauddin, M. Baradie, and M.S.J. Hashmi, 1995, Computer-aided analysis of a surface-roughness model for end milling, *Journal of Materials Processing Technology*, 55, 123-127
- [79] K.H. Fuh, and C.F. Wu, 1995, A proposed statistical model for surface quality prediction in end-milling of Al alloy, *International Journal of Machine Tools and Manufacture* , 35(8), 1187–1200
- [80] Y.H. Tsai, J.C. Chen and S.J. Lou, 1999, In-process surface recognition system based on neural networks in end milling cutting operations, *International Journal of Machine Tools and Manufacture*, 39(4), 583–605
- [81] S. M. Lou, J. C. Chen and C.M. Li, 1999, Surface roughness prediction technique for CNC end-milling, *Journal of Industrial Technology*, 15(1), pp. 1-6
- [82] J. Z. Zhang, J. C. Chen and E. D. Kirby, 2007, Surface roughness optimization in an end-milling operation using the Taguchi design method, *Journal of Materials Process Technology*, 184, 233-239
- [83] C.K. Chui and J.Z. Wang, 1991, A cardinal spline approach to wavelets, *Proc. Amer. Math. Soc.*, 113, 785-793
- [84] E. J. Stollnitz, T. D. DeRose and D.H. Salesin, 1996, *Wavelets for Computer Graphics: Theory and Application*, Morgan Kaufmann Publishers.

- [85] ISO 11562, 1991, Geometrical product specification (GPS) – surface texture: profile method – metrological characteristics of phase correct filters. Geneva: International Organization for Standardization
- [86] Y.B. Yuan, W.Y. Piao and J.B. Xu, 2006, A fast Gaussian filtering algorithm for three-dimensional surface roughness measurements, *Journal of Physics: Conference Series*, 48, 1401-1461
- [87] T.R. Thomas and G. Charlton, 1981, Variation of roughness parameters on some typical manufactured surfaces, *Precision Engineering*, 3(2), 91-96
- [88] M. J. Crawley, 2005, *Statistics: An Introduction using R*, John Wiley and Sons, Ltd.
- [89] C.M. Hoffmann, 1989, *Geometric & Solid Modeling*, Morgan Kaufmann Publishers
- [90] M. Mantyla, 1987, *An Introduction to Solid Modeling*, Computer Science Press, New York City, USA
- [91] V. Kumar, D. Burns, D. Dutta and C. Hoffmann, 1999, A framework for object modeling. *Computer-Aided Design*, 31(99), pp. 541-56
- [92] A.J. Markworth, K.S. Ramesh and W.P. Parks, 1995, Modelling studies applied to functionally graded materials, *Journal of Materials Science*, 30(9), pp. 2183-93
- [93] V. Kumar and D. Dutta, 1997, An approach to modeling heterogeneous objects, *Proceedings of the solid freeform fabrication symposium*, pp. 336
- [94] X. Qian and D. Dutta, 2003, Design of heterogeneous turbine blade, *Computer-Aided Design*, 35(3), pp. 319-29
- [95] K.H. Shin, 2002, Representation and process planning for layered manufacturing of heterogeneous objects. Ph.D. thesis. University of Michigan
- [96] J. Huang and G. Fadel, 2000, Heterogeneous flywheel modeling and optimization, *Materials and Design*, 21, pp. 111-125
- [97] M. Danczak, K.J. Wolter, R.R. OLTER and H. Roth, 2003, Application of computer tomography in electronic technology, 26th International Spring Seminar on Electronics Technology
- [98] Y. Li and J. Ni, 2009, Constraints based non-rigid registration for 2D blade profile reconstruction in reverse engineering, *ASME Journal of Computing and Information Science in Engineering*, to be appear.
- [99] G. H. Golub and C. Reinsch, 1970, Singular value decomposition and least squares solutions, *Numer. Math.* 14, pp. 403--420
- [100] Y. Li and J. Ni, 2009, B-spline wavelet-based multiresolution analysis (MRA) of surface texture in end-milling of aluminum, *ASME Journal of Manufacturing Science and Engineering*, accepted
- [101] T. W. Sederberg and S. R. Parry, 1986, Free-form deformation of solid geometric models, *ACM SIGGRAPH Computer Graphics*, 20(4), pp.151-160
- [102] S. Coquillart, 1990, "Extended free-form deformation: A sculpturing tool for 3D geometric modeling," *ACM SIGGRAPH Computer Graphics*, 24(4), pp.187-196

